

DISSERTATION

EXPLORING EXCITED STATES OF TRANSITION METAL PHOTOCATALYSTS WITH
TIME DEPENDENT DENSITY FUNCTIONAL THEORY

Submitted by

Collette M. Nite

Department of Chemistry

In partial fulfillment of the requirements

For the Degree of Doctor of Philosophy

Colorado State University

Fort Collins, Colorado

Spring 2018

Doctoral Committee:

Advisor: Anthony K. Rappé

Matthew Shores
Steven Strauss
James Sites

Copyright by Collette Margaret Nite 2018

All Rights Reserved

ABSTRACT

EXPLORING EXCITED STATES OF TRANSITION METAL PHOTOCATALYSTS WITH TIME DEPENDENT DENSITY FUNCTIONAL THEORY

Advances in photocatalysis have led to a rise in interests in more sustainable chemistry. It has been shown that visible light can be harnessed through a photocatalyst to promote conventionally unfavorable chemical transformations. Most of these photoreactions rely on a rare metal photocomplex such as $\text{Ru}(\text{bpy})_3^{2+}$. However, in order to scale these reactions for industrial purposes, rare metals must be replaced with more earth abundant metals. First row transition metals provide an earth abundant alternative that open up new reaction pathways. Due to the differences between first and second and third row transition metals, catalytic design requires complex knowledge of the photophysics and photochemistry of the complex that is not easily obtained with experimental methods.

Electronic structure methods can aid in catalytic design. Density functional theory (DFT) and time dependent density functional theory (TDDFT) are methods capable of calculating large molecular systems. TDDFT is a useful tool in studying excited states, providing excited state energies and intensities, probing the photochemistry of the system. However, DFT/TDDFT are by no means black box calculations, especially when calculating first row transition metal complexes with complicated spin state manifolds. Screening different metal ligand scaffolds requires a high level of benchmarking, ensuring functionals and basis sets are optimal for the given system. A

higher level of analysis is required in order to go beyond the electronic spectrum to get at the vibronic character of a system. There is also a coupling between the protonation of a complex and the electronic excited state. Understanding the protonation effects of a system is very useful for tuning a catalyst to a given reaction. In addition, specific binding effects of a solvent must be understood in order to corroborate theoretical and experimental data. All of these factors must be considered when studying the character of metals and their relation to their ligand backbone. This dissertation highlights these issues associated with using TDDFT for photocatalytic development, and derives useful conclusions furthering the development of a first row transition metal photocatalyst.

ACKNOWLEDGEMENTS

Graduate school has been an amazing, life-changing journey, one in my wildest dreams I did not know I would ever complete. I could not have completed the journey without many amazing people who have shaped me into a better scientist and person, cultivating both my craft and my character.

Above all I would like to thank my advisor, Tony Rappé for everything he has done for me. Going into graduate school I knew I wanted to work for him as I wanted to study inorganic complexes theoretically, and I am grateful that he gave me that opportunity working with me from the ground up despite my lack of knowledge of computers and theory. Throughout this graduate school process I have doubted myself in more ways than one, yet Tony, one of the most brilliant people I have ever met, always made me feel as though I was intelligent and capable. He has brought the scientist out in me that I never knew existed. Even when I failed, he helped me find the successes in the experience. He saw me through two pregnancies and made it possible to finish my degree with children. Tony has been there for both my professional and personal accomplishments and taught me that in life, it is possible to have it all without compromising as long as you work hard and are surrounded by a great team.

I would like to thank my committee, Matthew Shores, Steve Strauss, Alan Van Orden, and Jim Sites. They have opened my eyes to see other aspects of my research that I would miss without their different scientific expertise.

I would like to thank my family for all their love, support and encouragement throughout this entire process. Above all, I must thank my mother, Stacy, who has laid

down her life to be with me and my family when we needed her. She has supported me through everything, and was my first role model, showing me that as a woman you can attain many professional achievements without compromising your values and while still putting God and your family first.

I would like to thank my dad, Benny, for all the love, prayers and support. When I view myself the way I know my dad sees me, it makes me a more confident individual. He always has believed in my intelligence and has been able to calm me in the most stressful of times.

My brother, Tyler has also believed in me and given me all the love and support. Tyler and our dear friend, Reed, have helped my family immensely through moves in addition to lightening our load through laughs and good times. I am so grateful. I am especially in gratitude for Tyler and my mother taking care of my children through the most stressful time of my life when I defended my dissertation two weeks after the birth of my second child.

I am forever indebted to all the people who have prayed for us over the years, especially Drew Dutton and my Grandma Julie.

I also must thank my Grandpa Duane, who encouraged me to seek higher education and never allowed me to rest on my laurels.

I also am so grateful for my inlaws, David and Carol Nite, for all the love, prayer, and support. For always encouraging me to finish my degree even after the birth of my first child. For their example of marriage and partnership, and for raising the best partner for me in the world.

I want to thank my beautiful children, Augustine and Elisabeth, for filling my life with purpose for which I did not know I was lacking.

Most of all, I want to thank my beloved husband, Jacob, without whom I would have never obtained my greatest successes. Words cannot express how much gratitude and love I have for you. Every experience in this journey I am so grateful to have shared with you. Working both professionally and personally together has been the highlight of my life, and I am honored to continue the partnership throughout the rest of this life and the next. I could write a million pages about you and it still would not adequately describe how I feel.

DEDICATION

For Jacob Nite and Tony Rappé, who believed in me.

And our Blessed Mother who carried me through.

TABLE OF CONTENTS

ABSTRACT	ii
ACKNOWLEDGEMENTS	iv
DEDICATION	vii
LIST OF TABLES	x
LIST OF FIGURES	xi
CHAPTER 1: INTRODUCTION	1
I. INTRODUCTION	1
A. HOMOGENEOUS PHOTOCATALYSIS	4
B. OUTER SPHERE PHOTOCATALYSIS	4
C. [Ru(bpy) ₃]Cl ₂ AS A PHOTOCATALYST	5
D. OTHER 2 ND AND 3 RD ROW TRANSITION METAL PHOTOCATALYSTS	7
E. APPLICATION TO CO ₂ REDUCTION	8
F. FIRST ROW TRANSITION METAL PHOTOCATALYSTS	9
G. FIRST ROW TRANSITION METAL APPLICATION TO CO ₂ REDUCTION	10
H. COMPLICATIONS TO USING FIRST ROW TRANSITION METALS	11
I. INNER SPHERE PHOTOCATALYSIS	11
J. THEORETICAL APPLICATIONS	13
K. DFT APPROACHES FOR STUDYING PHOTOCATALYSTS	14
L. TDDFT APPROACHES FOR STUDYING PHOTOCATALYSTS	15
II. LIGAND METAL TRENDS	17
III. VIBRONIC EFFECTS	18
IV. PROTONATION STATES	18
V. VANADIUM CHEMISTRY	18
VI. COMPARISON TO EXPERIMENT	19
REFERENCES	20
CHAPTER 2: BENCHMARKING TDDFT CALCULATIONS AND ITS APPLICATION TO PERIODIC AND LIGAND TRENDS	39
I. INTRODUCTION	39
II. BENCHMARKING	44
III. METHODS	55
IV. RESULTS AND DISCUSSION	58
V. CONCLUSION	66
REFERENCES	68
CHAPTER 3: UNRAVELING THE SOURCE OF INTERSYSTEM CROSSING OF CHROMIUM BIPYRIDINE TYPE COMPLEXES	72
I. INTRODUCTION	72
II. THEORETICAL METHODOLOGY	73
III. RESULTS AND DISCUSSION	75
IV. CONCLUSIONS	84
REFERENCES	86
CHAPTER 4: IMPACT OF DEPROTONATION ON POTENTIAL PHOTOCOMPLEXES	88

I. INTRODUCTION	88
II. EXPERIMENTAL.....	91
III. RESULTS/DISCUSSION.....	91
IV. CONCLUSIONS.....	95
REFERENCES.....	98
CHAPTER 5: COMPARISON OF EXCITED STATE PROPERTIES OF CHROMIUM(III) AND VANADIUM(II) COMPLEXES: POTENTIAL AS PHOTOCATALYSTS	100
I. INTRODUCTION:.....	100
II. THEORETICAL METHODS:	102
A. STRUCTURE OPTIMIZATION AND THEORETICAL SPECTRA:	102
B. Cr / V(PDO) ₃ :	103
C. VIBRATIONAL PROJECTIONS:	104
III. RESULTS & DISCUSSION:	105
A. TDDFT:.....	105
B. SPIN DENSITY PLOTS:.....	106
C. VIBRATIONAL PROJECTION SPECTRA:	111
D. SORCI:	113
IV. CONCLUSIONS:.....	115
REFERENCES.....	117
CHAPTER 6: ELUCIDATING EXPERIMENTAL RESULTS OF MACROCYCLE PHOTOCOMPLEXES THROUGH TDDFT	118
I. INTRODUCTION	118
II. EXPERIMENTAL.....	119
III. RESULTS	120
IV. CONCLUSION	126
REFERENCES.....	130
CHAPTER 7: FUTURE DIRECTIONS	131

LIST OF TABLES

Table 2.1: The total energy of Ni(II) complex (2) as calculated with DFT	49
Table 3.1: Spin determinant components and coefficients that comprise the seventh quartet state.....	82
Table 3.2: Spin-determinant components for the eight doublet state.....	83
Table 5.1: Spin density plots of quartet and doublets states of the Cr(III)bpy ₃ and V(II)bpy ₃ photocomplexes.	108
Table 5.2: Spin density plots of quartet and doublets states of the Cr(III)pod and V(II)pod photocomplexes.	109
Table 5.3: Spin density plots of quartet and doublets states of the Cr(III)esterpod and V(II)esterpod photocomplexes.....	110
Table 6.1: NTOs of various excited states of the Cr(III)THB complex (8) with an acetonitrile molecules bound	127
Table 6.2: NTOs of selected excited states of the Cr(III)THB complex (9) with two acetonitrile molecules bound	128

LIST OF FIGURES

Figure 1.1: Oxidative photocatalytic cycle of Ru(bpy) ₃ ²⁺	6
Figure 1.2: The proposed inner sphere photocatalytic reaction for the endothermic conversion of methanol to methyl formate.....	12
Figure 2.1: Schiff-base synthesis	42
Figure 2.2: Salen-type ligand synthesis	43
Figure 2.3: Salophen ligand backbone.....	43
Figure 2.4: Cr(III) and Ni(II) THB complex structures used for benchmarking	47
Figure 2.5: Comparison of basis set effect on the theoretical TDDFT absorption spectrum of Ni(II) complex (2) using the APFD XC functional.....	48
Figure 2.6: Comparison of basis sets effect on the theoretical TDDFT absorption spectrum of Cr(II) complex (1) using the APF-D XC functional.	50
Figure 2.7: The electron density difference plots for a set of NTOs.....	51
Figure 2.8: Computational time in CPU hours versus basis sets	51
Figure 2.9: TDDFT absorption spectra of complexes (2) (left) and (3) (right)	52
Figure 2.10: Theoretical absorption spectra of Ni(II) complex (2).....	53
Figure 2.11: TDDFT absorption spectra with molar absorptivity (M ⁻¹ cm ⁻¹) vs. wavelength (nm) of Cr(III) complex (1) comparing XC correlation functionals	54
Figure 2.12: TDDFT absorption spectra of Cr(III) complex (1).....	55
Figure 2.13: TDDFT(APF-D/6-311+*) spectra of Cr(III)THB complex (1) with and without implicit DMF solvent.	56
Figure 2.14: Zn(II) Schiff base type complex (black) as compared to a Zn(II) hydrogen substituted tertiary amine type complex (orange).....	59
Figure 2.15: The TDDFT absorption spectra of a Schiff base tripodal complex	60
Figure 2.16: Salen ligand complexed to metal	61
Figure 2.17: The TDDFT (APF-D/6-311+G*) absorption spectra of the salen complex with high valent metals Ni(II), Cu(II), and Zn(II).....	61
Figure 2.18: The TDDFT (APF-D/6-311+G*) absorption spectra of the salen	62
Figure 2.19: NTOs for the Zn(II) nitrogen substituted salen complex	63
Figure 2.20: TDDFT(APF-D/6-311+G*) absorption spectra of nitrogen coordinated salen complex	63
Figure 2.21: TDDFT (APF-D/6-311+G*) absorption spectra of Zn(II) salen (green), a modified isopropanol bridging derivative (orange) and salophen (purple) complex. ..	64
Figure 2.22: Zn(II)THB complex with a nitrogen ethyl bridge enclosing the system.	65
Figure 2.23: A comparison of the TDDFT (APF-D/6-311G*) absorption spectra of Zn(II) complexes	66
Figure 3.1: TDDFT absorption spectra of Cr(III)(bpy) ₃	75
Figure 3.2: Pure electronic spectrum of Cr(III)(NH ₃) ₄ (bpy) calculated with TDDFT	77
Figure 3.3: The vibronic spectrum of the first excited state Cr(III)(NH ₃) ₄ (bpy)	77
Figure 3.4: DFT(APF-D/6-311+G*) optimized geometries and bond distances.....	78
Figure 3.5: Vibrational projection plots of the geometric transition	79
Figure 3.6: NTOs of the first excited states of bipyridine	81
Figure 3.7: The electronic configuration of one of the excited doublet states	84

Figure 4.1: Structure derivatives of Cr(III) complex.....	89
Figure 4.2: TDDFT(APF-D/6-311+G*) absorption spectra of Cr(III)(THB)	92
Figure 4.3: TDDFT(APF-D/6-311+G*) absorption spectra of Cr(II)(THB)	92
Figure 4.4: TDDFT(APF-D/6-311+G*) absorption spectra of chromium THB complex with implicit DMF solvent in various oxidation states.....	94
Figure 4.5: Experimental UV-vis spectra of Cr(III) (blue) and Cr(IV) (orange) THB.....	94
Figure 4.6: Spin density plots of Cr(II), complex (2) (left), Cr(III), complex (6) (center), and Cr(IV), complex (7) (right) THB complexes	95
Figure 4.7: The theoretical TDDFT spectrum (blue) and the experimental spectrum (black) of the Cr(III)THB complex (2)	96
Figure 4.8: The experimental crystal structure of the Cr(III) THB complex	96
Figure 5.1: TDDFT(APF-D/6-311+G*) spectra of various first row transition metal Schiff base complexes.....	105
Figure 5.2: TDDFT(APF-D/6-311+G*) spectra of various first row transition metal salen type complexes.....	106
Figure 5.3: Vibrational distortion projection plot.....	112
Figure 5.4: Plot of excited state energies of X(PDO) ₃ complexes.....	114
Figure 6.1: THB complex of first row transition metals that were calculated.....	120
Figure 6.2: TDDFT(APF-D/6-311+G*) absorption spectra of Cr(III) complex	121
Figure 6.3: Structure derivatives of Cr(III) THB complex with acetonitrile solvent.	123
Figure 6.4: TDDFT(APF-D/6-311+G*) absorption spectra of Cr(III) THB structures....	124
Figure 6.5: TDDFT(APF-D/6-311+G*) absorption spectrum of Cr(III)THB complex (8) with one acetonitrile explicitly bound	124
Figure 6.6: TDDFT(APF-D/6-311+G*) absorption spectrum of Cr(III)THB complex (9) with two acetonitrile molecules explicitly bound	125

CHAPTER 1: INTRODUCTION

I. INTRODUCTION

In recent decades, the field of photocatalysis has gained wide interest from multiple disciplines due to its potential for utilizing solar energy. Sunlight is a completely renewable, non-toxic, inexpensive form of energy that can be harvested to employ as both chemical reagent and fuel.¹ With growing concerns about global warming and our dependence on non-renewable fossil fuels, in addition to a growing push for “green” environmentally friendly chemical synthesis, harnessing energy from visible light seems intuitive. However, this endeavor is not without its challenges.

Of utmost environmental concern at the moment is our reliance on fossil fuels and our contribution to global warming. Carbon dioxide (CO₂) is an unwanted byproduct of our fossil fuel consumption. Our greenhouse gas emission is known to be driving global warming, and current levels of CO₂ in the atmosphere are currently unmatched by our planet’s natural carbon cycle. However, CO₂ has the potential to be used as an important chemical feedstock due to its non-toxicity and abundance.²

CO₂ is a non-polar, linear molecule and is the most oxidized form of carbon. The reduction of CO₂ can result in the formation of value added products such as methanol, dimethyl ether, and formic acid, all of which can be used as liquid fuels. Due to the thermodynamic stability of the carbon-oxygen double bonds, the reduction of CO₂ is an endothermic reaction that requires a substantial amount of energy input. In addition, there is a large kinetic barrier to overcome in order to reorient the linear CO₂ structure to a reduced bent structure. In order to overcome these thermodynamic and kinetic

barriers of CO₂ for the hydrogenation of CO₂ with H₂ for the production of CH₃OH, a catalyst can be used. For CO₂ hydrogenation to become a large-scale industrial process, there is need for the development of a low pressure catalytic process for CO₂ reduction.³

Another large environmental challenge is chemical waste. Synthetic reactions often require harsh chemicals and wasted stoichiometric reagents in order to promote complex organic transformations. Photocatalysis lay dormant in the field of organic chemistry for a number of years due to the fact that organic molecules usually do not absorb in the visible region, but are UV active. UV photoreactions require expensive and restricting photoreactors that are not economically viable.¹ Because organic molecules with C-C bonds are sensitive to high energy UV light, the application of UV photocatalysis is not practical. However, the prospect of transition metal photocatalysts acting as photocatalysts/photosensitizers for organic systems has recently garnered much attention. By operating in the visible region, UV decomposition reactions are avoided and complex organic transformations with weak bonds become feasible.⁴ Mild reaction conditions in visible light allow for more sensitive functional groups, where complex chemoselective transformations can be realized.⁵

A photocatalyst is a specific type of catalyst, which employs light to overcome the activation barrier of the reaction. The chromophore, acting as a catalyst, is sensitive to a given wavelength of light. The absorption of a photon of light by the chromophore results in the excitation of the chromophore from the ground to excited state. This harnessed energy can then be used to drive an otherwise unfavorable chemical reaction forward. Ideally, photocatalysis would harness solar energy, taking advantage

of this free renewable energy resource. The solar spectrum is composed of 3% UV light, 44% visible light, and 53% infrared light, with the majority of the intensity in the visible region.⁶ While the energy available in visible light (390-700 nm; 40-70 kcal/mol) is typically insufficient to directly drive bond formation, it is sufficient to perform oxidation/reduction chemistry facilitating reactions that drive bond formation, frequently through the generation of radical cation intermediates.^{7,8}

Transition metal complexes are ideal visible light photocatalysts due to their many low energy charge transfer excited states that are positioned within the visible region. Due to their unoccupied d orbitals, transition metals coordinate many organic substances. This creates a wide variety of complexes with different stability and solvent compatibility which can be customized for a given photocatalytic system.⁹ Also, their ability to easily undergo oxidation state changes makes these complexes good candidates for redox chemistry, a key mechanism in chemical synthesis.¹⁰ Therefore, large arrays of chemical transformations are conceivable with transition metal photocatalysts.⁵

Photocatalysts are classified as homogeneous or heterogeneous catalysts. For either heterogeneous or homogeneous catalysis, transition metals are most often employed for their available low lying excited states and their ability for transition metal complexes to easily undergo oxidation-reduction reactions.¹¹ Homogeneous catalysts are in the same phase as their reactants, while heterogeneous catalysts are in different phases. Many heterogeneous and homogeneous catalytic methods¹²⁻¹⁹ have been proposed to catalyze CO₂ conversion to CH₃OH. Homogeneous photocatalysis using noble metals such as Ru and Ir have shown promise.²⁰ While current methanol

industrial processes rely on heterogeneous catalysis at high temperatures ($>200\text{ }^{\circ}\text{C}$) and pressures ($>25\text{ bar}$), homogeneous catalytic development for CO_2 hydrogenation to CH_3OH would allow milder reaction conditions ($\leq 145\text{ }^{\circ}\text{C}$ and $\leq 60\text{ bar}$).²⁰ Because there is greater contact with reactants in a homogeneous process, there is a greater effective concentration of catalyst. Therefore, milder conditions can be applied with greater selectivity.³

A. HOMOGENEOUS PHOTOCATALYSIS

The homogeneous photocatalytic process can occur in one of two mechanisms; via outer sphere or inner sphere photocatalysis. The key difference between the two lies in the coordination spheres of the metal complex and its electron transfer partner.²¹ In the outer sphere mechanism, the coordination spheres of electron donor-acceptor pair stay intact as the electron tunnels through in the transition state. In contrast for the inner sphere mechanism, the coordination spheres of the donor-acceptor pair are structurally distorted with bonds forming a ligand bridge through which the electron transfer occurs.²²

B. OUTER SPHERE PHOTOCATALYSIS

In the outer sphere mechanism, the absorption of a photon of light first generates the excited state. A sacrificial electron acceptor/donor then oxidizes/reduces the complex to its oxidized/reduced ground state. From there, the oxidized/reduced complex can participate in the oxidative/reductive electron transfer process to oxidize/reduce a molecule to the desired product, which in turn regenerates the catalyst. The inner sphere mechanism is more complicated in that the solvated metal complex first undergoes a substitution of the solvent to form a bridge between the metal complex

and the desired substrate. The newly formed complex then absorbs a photon of light, generating the excited state. Through the bridging ligand, electron transfer occurs, oxidizing/reducing the metal and reducing/oxidizing the ligand. Following electron transfer, a separation of products occurs, often to include the transfer of the bridging ligand. An electron donor displaces the newly reduced ligand, resulting in the regeneration of the original metal complex.⁹

C. $[Ru(bpy)_3]Cl_2$ AS A PHOTOCATALYST

The most commonly used homogeneous photocatalyst /photoinitiator in literature is tris(bipyridine)ruthenium(II) chloride $[Ru(bpy)_3]Cl_2$. As a photocatalyst/photoinitiator, $[Ru(bpy)_3]^{2+}$ is pretty remarkable. The complex has a broad metal to ligand charge transfer (MLCT) absorption band at $\lambda = 452$ nm, where an electron from the Ru d orbital is transferred to a π^* orbital of a bpy ligand.²³ This absorption of high energy visible light provides adequate energy for further reaction.¹⁰ One feature of $[Ru(bpy)_3]^{2+}$ that is key to the success of this complex as a photocatalyst/photoinitiator is the generation of a long lived excited state.¹ $[Ru(bpy)_3]^{2+}$ is easy to synthesize and is chemically stable at high temperatures as well as acidic or basic conditions.¹ $[Ru(bpy)_3]^{2+}$ can act as a single electron oxidant or reductant, opening up the potential for the application of this photocatalyst to a wide variety of reactions.²⁴ This complex operates in an outer sphere mechanism as shown in Figure 1.1 for oxidation.

The energy transfer mechanism following the absorption of light is surmised as follows. The absorption of light by $[Ru(bpy)_3]^{2+}$ populates many singlet excited states. An internal conversion (IC) relaxes the complex to the first excited singlet 1MLCT_1 state. This state completes a rapid intersystem crossing (ISC) to the triplet manifold. The

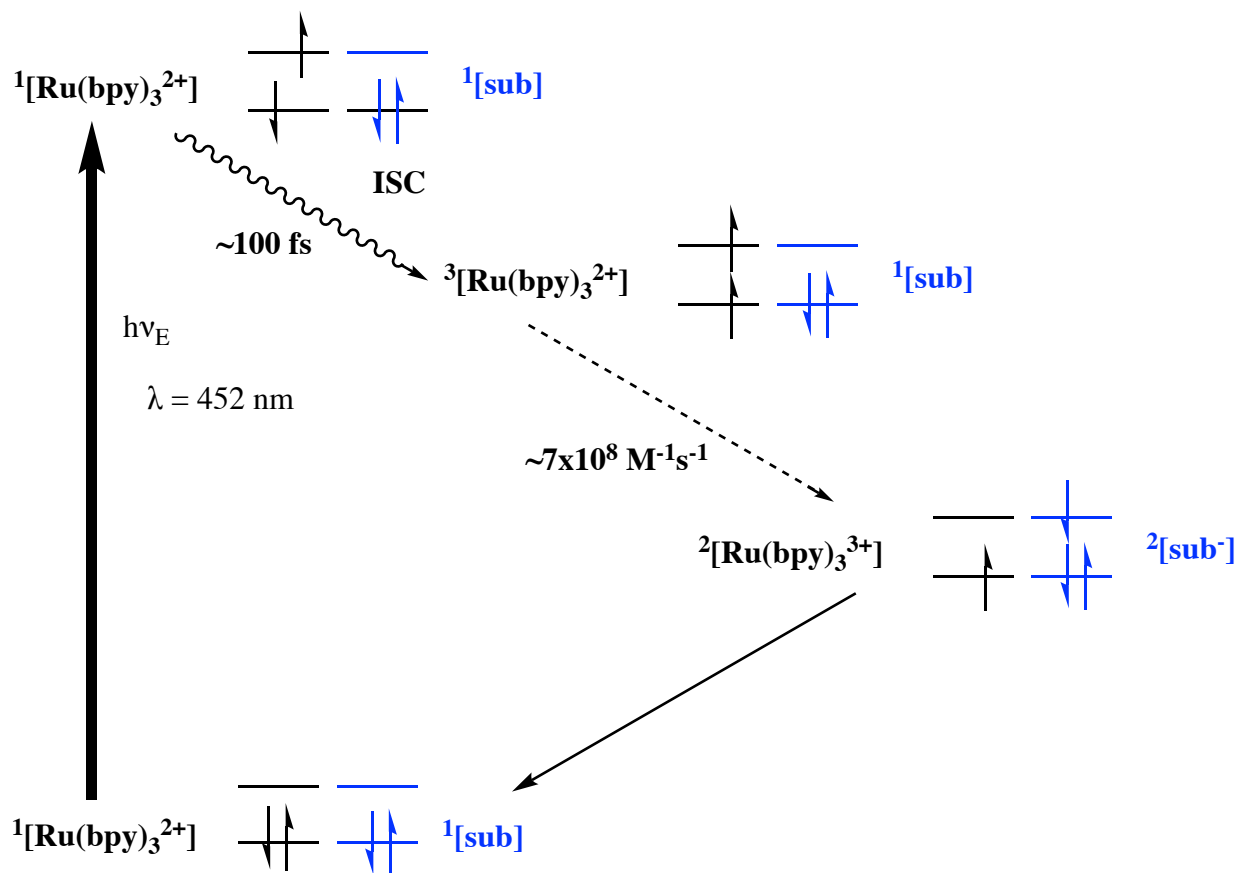


Figure 1.1: Oxidative photocatalytic cycle of $\text{Ru}(\text{bpy})_3^{2+}$ where [sub] represents the oxidative quenching substrate. The approximate rates/lifetimes of the ISC and electron transfer step are provided.^{25,26} A similar diagram could be drawn for the reductive cycle.

long-lived triplet state $^3\text{MLCT}_1$ is then generated by an internal conversion. From the triplet excited state $^3\text{MLCT}_1$, the complex is first quenched by a sacrificial reagent followed by a second electron transfer for desired chemical conversions, which also regenerates the catalyst.¹⁰

Hundreds of organic reactions have been photocatalyzed via $[\text{Ru}(\text{bpy})_3]^{2+}$.^{6,10,24} Some notable characteristics of these reactions include the use of sunlight as a reagent^{4,27}, stereoselective control in a photoreaction²⁷, photocatalyzed C-C bond

formation^{10,28,29}, enantioselective control^{29,30}, and tin-free green friendly reaction conditions.^{31,32} Similar complexes substituting Ru²⁺ for Ir³⁺ have been used.^{4,6}

D. OTHER 2ND AND 3RD ROW TRANSITION METAL PHOTOCATALYSTS

While [Ru(bpy)₃]²⁺ is the most commonly used homogeneous catalyst, organic synthesis has not been limited to this complex. Many Ru complexes have been studied for organic catalysis.^{33,34} Ru complexes with amine ligands provide more activation for certain hydrogenation reactions in addition to promoting product formation.³⁵ Another class of Ru complexes with pincer type ligands have shown great success in hydrogenation, nucleophilic substitutions, and oxidation reactions.^{36–40} Other metal substituted pincer complexes such as Rh, Ir, Pd, and Re have been studied extensively.^{4,37,41} Other second and third row transition metal complexes have been used in catalytic transformations as well. Pd and Rh catalysts are well known for their C-H bond activation and subsequent C-C bond formation.^{42,43} These complexes however are more rare and expensive than Ru, which has also shown capabilities of C-C bond formation.⁴⁴

Ru catalysts are capable of asymmetric hydrogenation of ketones.^{45–48} In fact, one of the driving factors in catalytic research of these systems is the application of these catalysts for enantioselective product formation.³⁵ Polydentate ligands have been shown to be important for the structural stability of the catalyst, in addition to providing better enantiomeric control.³⁵ Rh and Pt catalysts have been shown to provide enhanced regioselectivity in the various synthesis reactions.^{49–51} Rh catalysts have also shown diastereoselectivity⁵² as well as enantioselectivity.⁵³ Ru complexes have the potential for high chemoselectivity.⁵⁴

Often reactions require harsh reaction conditions and toxic or stoichiometric reagents that amount to waste. However, Ru catalysis has been shown to eliminate the need for these harsh conditions, such as efficient hydrogenation of carboxylic esters and amide formation.^{38,54,55}

E. APPLICATION TO CO₂ REDUCTION

Many similar homogenous catalytic systems have also been applied to CO₂ hydrogenation to methanol or other value added products with wide success, with Ru leading the way.⁵⁶ Ruthenium pincer type ligands are at the forefront for this conversion, in addition to Re pincer complexes.^{20,37,57–63} Ir complexes have effectively reduced CO₂, as Ir(III) is in general more strongly reducing than Ru(II).^{13,58,64–66} Os has also been used as the metal catalyst.⁶⁷ Ru and Rh phosphine systems have effectively hydrogenated captured CO₂.^{68–70} Re and Ru macrocyclic and porphyrin type complexes (in addition to bpy ligands) have also been innovative CO₂ photosensitizers.⁷¹

Hydrogen storage is another avenue for alternative energy sources. The reversible hydrogenation of small molecules has this capability, and Ru pincer catalysts have shown useful for mediating this reaction.^{63,72} Iridium catalysts also have success in hydrogen storage, using CO₂ as the hydrogen storage vehicle.⁷³

The literature is saturated with catalysts that have been efficacious in organic transformations and the reduction of CO₂. However, a vast majority of these studies have relied solely on rare second and third row transition metals. The consequence lies in that these complexes are not scalable industrially due to the expense of rare metals.

F. FIRST ROW TRANSITION METAL PHOTOCATALYSTS

Ruthenium along with other precious metals such as Ru, Re, Rh, Pd, Te, Re, Os, Au, Pt, and Ir have abundances fewer than 10^{-3} atoms of element per 10^6 atoms of Si. Starkly contrasting, first row transition metals such as Fe, Ti, Mn, Cr, Zn, Cr, Co, and Ni are much more abundant (between 10^1 and 10^5 atoms of element per 10^6 atoms of Si).⁷⁴ Ideally, Ru could be substituted with one of these metals. However first row transition metals behave a lot differently than second and third row transition metals.

While most research has focused on 2nd and 3rd row transition metal catalysts, there has been a large push to earth abundant 1st row transition metal catalysts, often built on the 2nd and 3rd row complex framework. Much of the work has taken particular interest in iron, which is in the same group as ruthenium. Iron is of great interest as it is the most abundant transition metal (the fourth most abundant element in the earth's crust)⁷⁴, its low toxicity, and low cost. In organic synthesis, Fe pincer complexes are of particular interest.⁷⁵ Fe pincer complexes have effectively hydrogenated ketones, esters, and nitriles in mild waste free mechanisms.^{37,76-80} Co and Ni pincer complexes have been effective at C-C bond transformations and dehydrogenation/hydrogenation reactions.³⁷ A Cu complex has been shown to photocatalyze the photocyclization of [5]helicene using visible light.⁸¹ A salen ligand manifold have been shown to complex with a wide variety of 1st row transition metals to catalyze a wide variety of organic transformations.⁸²⁻⁸⁴ Mn and Zn salen derivative complexes are strongly photoluminescent which could imply long lived excited state character useful for photochemistry.⁸⁵ Cr complexes have very attractive photo-oxidizing potentials and long

excited state lifetimes.⁸⁶ Cr complexes are powerful photooxidants with strong potential to replace ruthenium in photooxidative catalysis.^{87,88}

G. FIRST ROW TRANSITION METAL APPLICATION TO CO₂ REDUCTION

There has also been progress in the application of 1st row transition metal complexes for CO₂ hydrogenation. Iron pincer complexes are capable of reversible CO coordination and methanol and formic acid dehydrogenation reactions.⁸⁹⁻⁹¹ In addition, Fe pincer complexes have hydrogenated CO₂ at low pressures.⁹² Another Fe complex with tetraphosphine based ligands hydrogenated CO₂ to alkyl formates and formamides.⁹³ Iron porphyrins have reduced CO₂ to CO with visible light.⁹⁴ Cu-ceria and Cu-ceria-titania catalysts as well as Cu₄ clusters have hydrogenated CO₂ with methanol in heterogeneous mechanisms.¹² A homogeneous Cu complex was used for visible light photoredox catalysis for C-C bond formation.⁹⁵

While the initial stages of research with these more abundant complexes have proven that catalysis with 1st row transition metals is possible, the realization is muted in comparison to Ru and other 2nd and 3rd row transition metals. The turnover numbers for the 1st row transition metal catalyst are often low as comparing Fe to Ru in the production of H₂ and CO₂ from methanol.^{90,96} Additionally, absorption by the catalyst is often much less intense for a 1st row metal. For instance, [Ru(bpy)₃]²⁺ absorbs visible light ~50 times more strongly than [Cr(bpy)₃]³⁺.⁸⁶ First row transition metals in general behave drastically different than 2nd and 3rd row counterparts. In order for the replacement of rare metals with 1st row transition metals to come to fruition, selective catalytic design with ligand modifications must take place.

H. COMPLICATIONS TO USING FIRST ROW TRANSITION METALS

Second and third row transition metal complexes are generally more stable than first row counterparts due to better orbital overlap with ligand orbitals. 4d and 5d orbitals with radial nodes are much larger than 3d orbitals. The 3d orbitals of first row transition metals are mostly hidden by larger filled 3s and 3p shells, so these orbitals have poor overlap with the ligand orbitals. In general, first row transition metals are much more reactive than second and third row transition metals. Therefore, ligands are non-innocent and catalysts tend to be less stable due to ligand lability. Secondly, first row transition metals are spin active and can occupy different spin states very easily depending on ligands and oxidation states of the complex. Lower row transition metals are restricted to low spin states due to larger d orbital energy splitting. In comparison, first row transition metals exhibit highly different chemistry than heavy metal catalysts. Active spin states also leads to complicated excited state manifolds, which are difficult to characterize.

I. INNER SPHERE PHOTOCATALYSIS

The complications that arise from moving to abundant first row transition metals including ligand lability and complicated excited state manifolds do not typically fare well for the same outer sphere mechanism that works so well for lower transition metals such as Ru(bpy)₃. However, there is potential to exploit these challenges in an inner sphere mechanism. For instance, ligand lability lends itself to weaker metal-ligand bonds, which have the potential to allow a substrate to bind and release from a catalyst. Also, first row transition metals' electron spin activity offers the possibility of controlling the electron spin and play the noninnocence to our advantage. An inner sphere

scenario could potentially allow greater stereocontrol by controlling substrate activation. In addition, the need for sacrificial reagents could potentially be eliminated.

An inner sphere mechanism for the reduction of carbon dioxide (CO_2) to value added chemical feedstocks is shown in Figure 1.2. The inner sphere mechanism proceeds first by CO_2 binding to the metal center of the photocatalyst at an open or solvent protected coordination site (step 1). This complex is then excited with visible light ideally generating a charge separated state where the bound CO_2 is reduced, producing radical character centered on the carbon atom (step 2). This radical abstracts a hydrogen from a C-H bond of a methane molecule, forming a solvent radical cage

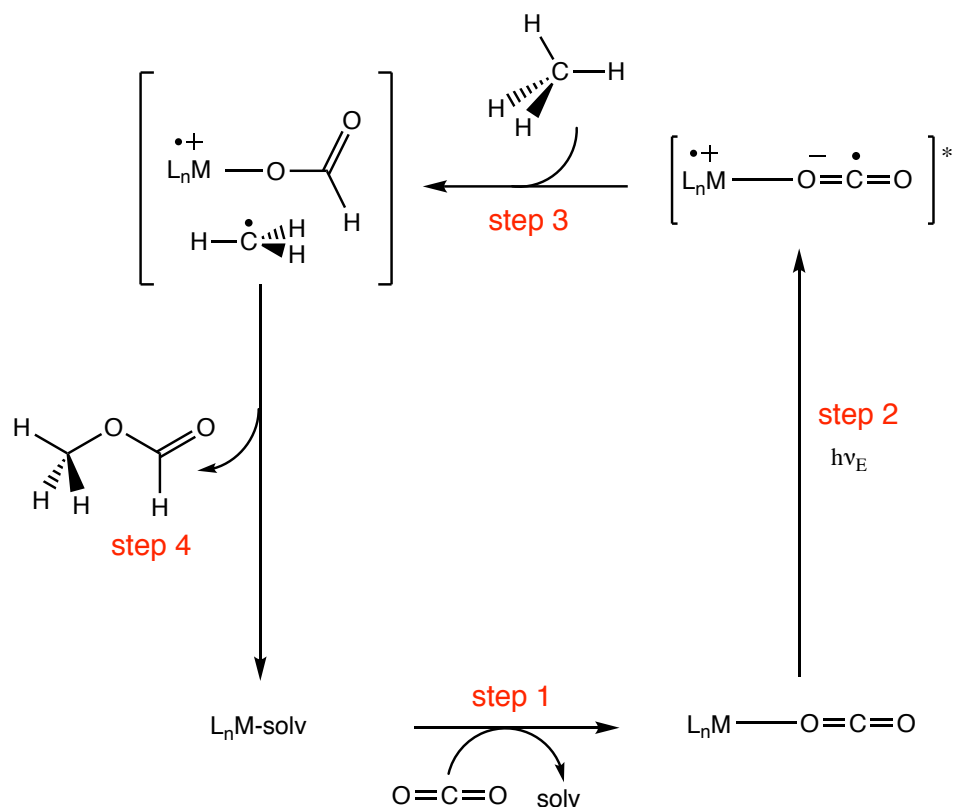


Figure 1.2: The proposed inner sphere photocatalytic reaction for the endothermic conversion of methanol to methyl formate using CO_2 as a terminal oxidant.

(step 3). The caged radical pair combines, yielding methyl formate and the regenerated metal catalyst (step 4).

The inner sphere electron transfer scheme requires sophisticated catalytic design for it to be a practical method for organic transformations, including endothermic reactions. Elucidating how first row transition metal photocomplexes differ from well studied lower transition metal photochemical complexes is of significant interest for making photocatalysis a large scale chemical industrial process. This however is a complicated problem that is difficult to study in a purely experimental fashion. Electronic structure theory has the potential to help answer many of these complex questions.

J. THEORETICAL APPLICATIONS

It would be highly impractical and wasteful to attempt to explore these catalysts by experimentally synthesizing these complexes alone. Rather, with high levels of theory, transition metal complexes can be screened and tuned to optimize the catalyst while gaining knowledge as to what electronic structure properties yield great potential for these organic transformations. Catalysts can first be screened for good photocatalytic properties including by observing their absorption in the visible spectrum, their low excited states and their potential for intersystem crossing. In addition, the orbitals of the complex can be analyzed for their potential for sufficient charge separation and thus electron transfer.

Transition metal photocomplexes are generally large, many electron systems with complicated spin manifolds, which were once intangible for electronic structure calculations. However, with the modern development of density functional theory (DFT) in conjunction with increased computational power, complexes with upwards of a few

hundred atoms can now be calculated with accuracy comparable to expensive wavefunction based methods. By applying a time-dependent formalism, excited states of a complex can be calculated and evaluated with a linear response extension to DFT, time dependent DFT (TDDFT).⁹⁷

K. DFT APPROACHES FOR STUDYING PHOTOCATALYSTS

While understanding the mechanism of these catalytic systems is key to improving the functionality of these catalysts (increased turnover, diastereocontrol, enantioselectivity, and regeneration of the catalyst), there are no easy experimental approaches. DFT plays a significant role in studying the mechanisms of transition metal homogeneous catalysis, by identifying transition state intermediates and near-degenerate states as well as conformational changes.⁹⁸ Conformational changes for controlling charge transfer in Ru donor-acceptor systems were explored with DFT.⁹⁹ Mechanisms pertaining to Ru catalysis have been studied extensively.^{33,38,96,100,101} The mechanism of the hydrogenation of CO₂ of Ir, Co, and Fe pincer complexes have been studied with DFT, revealing the importance of the presence of base and unsaturated ligand for hydrogen activation and regeneration of the catalyst.^{58,65} The important role of proton-transfer shuttles of Ir pincer catalysts was determined in a mechanistic study of Ru and Ir pincer complexes.⁴¹ An alternative mechanism for the asymmetric hydrogenation of acetophenone by a Noyori's Ru catalyst was predicted using DFT.⁴⁵ In addition, DFT has been effective in predicting trends of one-electron redox potentials when a baseline shift to the systematic underestimation of the XC functional is applied.¹⁰² DFT excited state calculations on Ru(II) polypyridine dyads predicted that

extending the π conjugation of the ligand could improve the electron injection step into a semiconductor substrate.¹⁰³

L. TDDFT APPROACHES FOR STUDYING PHOTOCATALYSTS

Calculating excited states is vital to properly understanding photocatalytic systems, as shown in the amount of literature applying TDDFT methodology. Ab initio theoretical optical spectroscopy for transition metal complexes is an underutilized methodology for studying these complexes, but is gaining traction in the field.¹⁰⁴ Theoretical TDDFT spectra of transition metal complexes have been shown to have reasonable agreement with experimental results.^{105–107}

For cases where the metal has unpaired electrons (an open shell system), unrestricted DFT/TDDFT calculations should be applied. As in a study of the theoretical vibrational circular dichroism spectra on Ru, Cr, Co, and Rh complexes, unrestricted calculations corrected previous closed shell calculations, predicting fair results in comparison to experiment.¹⁰⁸ Cr(III)¹⁰⁹, Fe(III)¹¹⁰ and other metal complexes¹⁰⁶ have been studied using unrestricted TDDFT.¹¹¹

For theoretical calculations of these homogeneous systems, the inclusion of solvent (typically via implicit PCM methods) is necessary for accurate results.¹⁰² Without solvent, reactions are often predicted to proceed through alternative pathways and transition states.⁴⁵ Correct interpretation of excited states in TDDFT cannot be accomplished without solvent effects.^{112,113}

The ever-popular Ru complexes have been studied using TDDFT in order to corroborate the experimentally seen excited states with theoretical understanding. The excited states of Ru(bpy)₃²⁺ and its derivatives have been characterized with

TDDFT.^{112,114} The charge transfer and excited states of d^6 metal complexes have been studied extensively.^{103,115,116} Low lying excited states of $[\text{Ru(III)}(\text{acac})_3]$ were predicted upon theoretically calculating their excited states, which experimental data confirmed.¹⁰⁸

First row metal complexes have also been studied with TDDFT, providing preliminary information about these complex systems. McDaniel, Rappé, and Shores demonstrated TDDFT calculations can qualitatively predict certain features in experimental spectra in a wide variety of transition metal complexes.¹⁰⁶ Through TDDFT calculations, it was shown that a bridgehead nitrogen moiety greatly affected the photophysical properties of chromium iminopyridine, highlighting that small changes to the ligand can result in more desired photophysics.⁸⁷ Copper coordination compounds have been studied with TDDFT extensively, often yielding insight into the excitations and excited state structural distortions.¹¹⁸ Absorption bands for oxoiron(IV) complexes have been characterized using TDDFT which provided alignments of the ligand to metal-oxygen charge transfer absorptions that were consistent with experimental observations.¹¹⁹ The excited states of Fe(II) polypyridine complexes for DSSCs was studied, showing two intense transitions were due to metal to ligand charge transfer states, helping to elucidate the nature of experimental observed absorption bands.¹²⁰

As many researchers have noted, important benchmarking should take place in order to select the best exchange-correlation (XC) functional and basis set to properly characterize the system. While electronic structure calculations on transition metals and their complexes are complicated, due to their partially filled d subshells and low lying near degenerate excited states, the selective choice of XC functional and knowledge of the system of study can yield results that can give insight into the given system.¹²¹ Long

range charge transfer energies are notoriously underestimated in TDDFT, and therefore it is important to consider which functional is employed to offset this error.^{102,122} What is important in calculating these complexes with long range charge transfer character is the use of a hybrid XC functional containing a certain amount of Hartree-Fock exact exchange.^{123–125} Some functionals have gone as far as to range (distance) separate local and non-local exchange.¹²⁶ While the various functional approaches can help describe a wide variety of chemical systems, it is difficult to know if the specific features of each functional correctly describe a transition metal complex system.

A notable challenge in 1st row transition metal calculations as compared to 2nd and 3rd row metals is their potential for spin crossover, where the preferential orbital occupation of the d electrons can be altered by external fields such as ligand changes, temperature, magnetic fields, and solvent environment. This is due to the 1st row metals having small ligand field splittings. The ability of DFT to calculate the correct ground state is often problematic, and the appropriate XC functional is important. Pure functionals favor low spin states whereas high spin states are predicted with hybrid functionals.¹²⁷

II. LIGAND METAL TRENDS

The replacement of rare metals such as Ru with earth abundant first row transition metals such as Fe requires the systematic understanding of how 1st row transition metals are different as well as an approach for improving these metals' properties in metal ligand catalyst design. A study of Ru vs. Fe complexes attributed the red shift in absorption energy of the Fe complex to its lower electronegativity, and suggested that π -electron rich ligands can offset this red shift.¹²⁸ Purposeful ligand

modifications must be studied to improve potential catalytic activity of these 1st row transition metal complexes.

III. VIBRONIC EFFECTS

Because coupled vibrational and electronic (vibronic) excitations make up the shape of absorption spectra in gas phase, it is important that these spectral features are accounted for in theoretical calculations. Experimentally, there is no easy way to get at this information. However, if proper steps are taken in a DFT/TDDFT calculation, these vibronic evolutions can be resolved theoretically. The calculations necessary to produce a vibronic spectrum include calculating the structures and vibrational modes of both the ground and desired excited state followed by calculating the allowed vibronic transitions. This inclusion in theoretical spectra could lead to a better analysis of experimental spectra and yield key insight into spectral features, confirming structural information.¹²⁹

IV. PROTONATION STATES

Another important factor to consider is the protonation state of these systems. The protonation state of a complex can have drastic effects on the absorption spectra, structure, and solvent interaction. By understanding the protonation states of a system, protonation can be used as a tunable approach to modifying these complexes for desired photochemical properties, as well as a potential for proton shuttling.⁴¹

V. VANADIUM CHEMISTRY

Following the surveying of metal and ligand interactions for tunable catalysts, trends can be elucidated comparing certain metals as potential for metal substitution. Cr has been shown to be an important catalyst with long lived states.^{86,88} The excited states of [V(II)(bpy)₃] were studied, confirming similarities to Cr complexes¹⁰⁷ and the

inherent stability of high spin d^3 complexes.¹³⁰ While Cr is an Earth-abundant 1st row transition metal, there are concerns with the toxicity and carcinogenic properties of Cr(VI). A question arises whether it is possible to substitute d^3 Cr(III) with a similar d^3 V(II) species. The study and characterization of Cr(III) and V(II) complexes can shed light on this question, illuminating an approach to evolve vanadium chemistry.

VI. COMPARISON TO EXPERIMENT

The relevance of the theoretical results of TDDFT based methods is strengthened by comparisons to experimental results. Therefore, it is important to confirm conclusions derived from theoretical results with experimental evidence. TDDFT absorption spectra can be compared with experimental spectra and absorption peaks' characterization can be confirmed with experimental behavior. Experiment and theory should not live exclusively, but rather collectively enhance the photocatalytic work by working symbiotically with each other's strengths.

In the following chapters important challenges to the computation electronic spectra are tackled and promising results achieved.

REFERENCES

- (1) Yoon, T. P.; Ischay, M. A.; Du, J. Visible Light Photocatalysis as a Greener Approach to Photochemical Synthesis. *Nat. Chem.* **2010**, *2* (7), 527–532.
- (2) Finn, C.; Schnittger, S.; Yellowlees, L. J.; Love, J. B. Molecular Approaches to the Electrochemical Reduction of Carbon Dioxide. *Chem. Commun.* **2012**, *48* (10), 1392–1399.
- (3) Han, Z.; Rong, L.; Wu, J.; Zhang, L.; Wang, Z.; Ding, K. Catalytic Hydrogenation of Cyclic Carbonates: A Practical Approach from CO₂ and Epoxides to Methanol and Diols. *Angew. Chem. Int. Ed.* **2012**, *51* (52), 13041–13045.
- (4) Hurtley, A. E.; Lu, Z.; Yoon, T. P. [2+2] Cycloaddition of 1,3-Dienes by Visible Light Photocatalysis. *Angew. Chem. Int. Ed.* **2014**, *53* (34), 8991–8994.
- (5) Farney, E. P.; Yoon, T. P. Visible-Light Sensitization of Vinyl Azides by Transition-Metal Photocatalysis. *Angew. Chem. Int. Ed.* **2014**, *53* (3), 793–797.
- (6) Schultz, D. M.; Yoon, T. P. Solar Synthesis: Prospects in Visible Light Photocatalysis. *Science* **2014**, *343* (6174), 1239176.
- (7) Yoon, T. P.; Ischay, M. A.; Du, J. Visible Light Photocatalysis as a Greener Approach to Photochemical Synthesis. *Nat. Chem.* **2010**, *2* (7), 527–532.
- (8) Prier, C. K.; Rankic, D. A.; MacMillan, D. W. C. Visible Light Photoredox Catalysis with Transition Metal Complexes: Applications in Organic Synthesis. *Chem. Rev.* **2013**, *113* (7), 5322–5363.

- (9) Cieřła, P.; Kocot, P.; Mytych, P.; Stasicka, Z. Homogeneous Photocatalysis by Transition Metal Complexes in the Environment. *J. Mol. Catal. Chem.* **2004**, *224* (1–2), 17–33.
- (10) Tucker, J. W.; Stephenson, C. R. J. Shining Light on Photoredox Catalysis: Theory and Synthetic Applications. *J. Org. Chem.* **2012**, *77* (4), 1617–1622.
- (11) Kumar, B.; Llorente, M.; Froehlich, J.; Dang, T.; Sathrum, A.; Kubiak, C. P. Photochemical and Photoelectrochemical Reduction of CO₂. *Annu. Rev. Phys. Chem.* **2012**, *63* (1), 541–569.
- (12) Graciani, J.; Mudiyansele, K.; Xu, F.; Baber, A. E.; Evans, J.; Senanayake, S. D.; Stacchiola, D. J.; Liu, P.; Hrbek, J.; Sanz, J. F.; et al. Highly Active Copper-Ceria and Copper-Ceria-Titania Catalysts for Methanol Synthesis from CO₂. *Science* **2014**, *345* (6196), 546–550.
- (13) McNamara, N. D.; Hicks, J. C. CO₂ Capture and Conversion with a Multifunctional Polyethyleneimine-Tethered Iminophosphine Iridium Catalyst/Adsorbent. *ChemSusChem* **2014**, *7* (4), 1114–1124.
- (14) Ghuman, K. K.; Hoch, L. B.; Szymanski, P.; Loh, J. Y. Y.; Kherani, N. P.; El-Sayed, M. A.; Ozin, G. A.; Singh, C. V. Photoexcited Surface Frustrated Lewis Pairs for Heterogeneous Photocatalytic CO₂ Reduction. *J. Am. Chem. Soc.* **2016**, *138* (4), 1206–1214.
- (15) McConnell, I.; Li, G.; Brudvig, G. W. Energy Conversion in Natural and Artificial Photosynthesis. *Chem. Biol.* **2010**, *17* (5), 434–447.
- (16) Lang, X.; Chen, X.; Zhao, J. Heterogeneous Visible Light Photocatalysis for Selective Organic Transformations. *Chem. Soc. Rev.* **2014**, *43* (1), 473–486.

- (17) Banerjee, S.; Pillai, S. C.; Falaras, P.; O'Shea, K. E.; Byrne, J. A.; Dionysiou, D. D. New Insights into the Mechanism of Visible Light Photocatalysis. *J. Phys. Chem. Lett.* **2014**, *5* (15), 2543–2554.
- (18) Ola, O.; Maroto-Valer, M. M. Review of Material Design and Reactor Engineering on TiO₂ Photocatalysis for CO₂ Reduction. *J. Photochem. Photobiol. C Photochem. Rev.* **2015**, *24* (Supplement C), 16–42.
- (19) Zhang, G.; Kim, G.; Choi, W. Visible Light Driven Photocatalysis Mediated via Ligand-to-Metal Charge Transfer (LMCT): An Alternative Approach to Solar Activation of Titania. *Energy Environ. Sci.* **2014**, *7* (3), 954–966.
- (20) Alberico, E.; Nielsen, M. Towards a Methanol Economy Based on Homogeneous Catalysis: Methanol to H₂ and CO₂ to Methanol. *Chem. Commun.* **2015**, *51* (31), 6714–6725.
- (21) Torres, L. M.; Gil, A. F.; Galicia, L.; González, I. Understanding the Difference between Inner- and Outer-Sphere Mechanisms: An Electrochemical Experiment. *J. Chem. Educ.* **1996**, *73* (8), 808.
- (22) Kochi, J. K. Electron Transfer and Charge Transfer: Twin Themes in Unifying the Mechanisms of Organic and Organometallic Reactions. *Angew. Chem. Int. Ed. Engl.* **1988**, *27* (10), 1227–1266.
- (23) Damrauer, N. H.; Cerullo, G.; Yeh, A.; Boussie, T. R.; Shank, C. V.; McCusker, J. K. Femtosecond Dynamics of Excited-State Evolution in [Ru(Bpy)₃]²⁺. *Science* **1997**, *275* (5296), 54–57.
- (24) Narayanam, J. M. R.; Stephenson, C. R. J. Visible Light Photoredox Catalysis: Applications in Organic Synthesis. *Chem. Soc. Rev.* **2011**, *40* (1), 102.

- (25) Yoon, S.; Kukura, P.; Stuart, C. M.; Mathies, R. A. Direct Observation of the Ultrafast Intersystem Crossing in Tris(2,2'-Bipyridine)Ruthenium(II) Using Femtosecond Stimulated Raman Spectroscopy. *Mol. Phys.* **2006**, *104* (8), 1275–1282.
- (26) Wrighton, M.; Markham, J. Quenching of the Luminescent State of Tris(2,2'-Bipyridine)Ruthenium(II) by Electronic Energy Transfer. *J. Phys. Chem.* **1973**, *77* (26), 3042–3044.
- (27) Ischay, M. A.; Anzovino, M. E.; Du, J.; Yoon, T. P. Efficient Visible Light Photocatalysis of [2+2] Enone Cycloadditions. *J. Am. Chem. Soc.* **2008**, *130* (39), 12886–12887.
- (28) Rueping, M.; Koenigs, R. M.; Poscharny, K.; Fabry, D. C.; Leonori, D.; Vila, C. Dual Catalysis: Combination of Photocatalytic Aerobic Oxidation and Metal Catalyzed Alkynylation Reactions—C–C Bond Formation Using Visible Light. *Chem. – Eur. J.* **2012**, *18* (17), 5170–5174.
- (29) DiRocco, D. A.; Rovis, T. Catalytic Asymmetric α -Acylation of Tertiary Amines Mediated by a Dual Catalysis Mode: N-Heterocyclic Carbene and Photoredox Catalysis. *J. Am. Chem. Soc.* **2012**, *134* (19), 8094–8097.
- (30) Nicewicz, D. A.; MacMillan, D. W. C. Merging Photoredox Catalysis with Organocatalysis: The Direct Asymmetric Alkylation of Aldehydes. *Science* **2008**, *322* (5898), 77–80.
- (31) Tucker, J. W.; Nguyen, J. D.; Narayanam, J. M. R.; Krabbe, S. W.; Stephenson, C. R. J. Tin-Free Radical Cyclization Reactions Initiated by Visible Light Photoredox Catalysis. *Chem. Commun.* **2010**, *46* (27), 4985–4987.

- (32) Narayanam, J. M. R.; Tucker, J. W.; Stephenson, C. R. J. Electron-Transfer Photoredox Catalysis: Development of a Tin-Free Reductive Dehalogenation Reaction. *J. Am. Chem. Soc.* **2009**, *131* (25), 8756–8757.
- (33) Bellarosa, L.; Díez, J.; Gimeno, J.; Lledós, A.; Suárez, F. J.; Ujaque, G.; Vicent, C. Highly Efficient Redox Isomerisation of Allylic Alcohols Catalysed by Pyrazole-Based Ruthenium(IV) Complexes in Water: Mechanisms of Bifunctional Catalysis in Water. *Chem. – Eur. J.* **2012**, *18* (25), 7749–7765.
- (34) Zimmer-De Iuliis, M.; Morris, R. H. Kinetic Hydrogen/Deuterium Effects in the Direct Hydrogenation of Ketones Catalyzed by a Well-Defined Ruthenium Diphosphine Diamine Complex. *J. Am. Chem. Soc.* **2009**, *131* (31), 11263–11269.
- (35) Clapham, S. E.; Hadzovic, A.; Morris, R. H. Mechanisms of the H₂-Hydrogenation and Transfer Hydrogenation of Polar Bonds Catalyzed by Ruthenium Hydride Complexes. *Coord. Chem. Rev.* **2004**, *248* (21–24), 2201–2237.
- (36) Younus, H. A.; Su, W.; Ahmad, N.; Chen, S.; Verpoort, F. Ruthenium Pincer Complexes: Synthesis and Catalytic Applications. *Adv. Synth. Catal.* **2015**, *357* (2–3), 283–330.
- (37) Werkmeister, S.; Neumann, J.; Junge, K.; Beller, M. Pincer-Type Complexes for Catalytic (De)Hydrogenation and Transfer (De)Hydrogenation Reactions: Recent Progress. *Chem. – Eur. J.* **2015**, *21* (35), 12226–12250.
- (38) Gellrich, U.; Khusnutdinova, J. R.; Leitus, G. M.; Milstein, D. Mechanistic Investigations of the Catalytic Formation of Lactams from Amines and Water with Liberation of H₂. *J. Am. Chem. Soc.* **2015**, *137* (14), 4851–4859.

- (39) Neumann, J.; Bornschein, C.; Jiao, H.; Junge, K.; Beller, M. Hydrogenation of Aliphatic and Aromatic Nitriles Using a Defined Ruthenium PNP Pincer Catalyst. *Eur. J. Org. Chem.* **2015**, *2015* (27), 5944–5948.
- (40) Gunanathan, C.; Milstein, D. Bond Activation and Catalysis by Ruthenium Pincer Complexes. *Chem. Rev.* **2014**, *114* (24), 12024–12087.
- (41) Qu, S.; Dang, Y.; Song, C.; Wen, M.; Huang, K.-W.; Wang, Z.-X. Catalytic Mechanisms of Direct Pyrrole Synthesis via Dehydrogenative Coupling Mediated by PNP-Ir or PNN-Ru Pincer Complexes: Crucial Role of Proton-Transfer Shuttles in the PNP-Ir System. *J. Am. Chem. Soc.* **2014**, *136* (13), 4974–4991.
- (42) Stache, E. E.; Seizert, C. A.; Ferreira, E. M. Molecular Scaffolds with Remote Directing Groups for Selective Palladium-Catalyzed C–H Bond Functionalizations. *Chem. Sci.* **2012**, *3* (5), 1623.
- (43) Hyster, T. K.; Rovis, T. An Improved Catalyst Architecture for Rhodium(II) Catalyzed C–H Activation and Its Application to Pyridone Synthesis. *Chem. Sci.* **2011**, *2* (8), 1606.
- (44) Arockiam, P. B.; Bruneau, C.; Dixneuf, P. H. Ruthenium(II)-Catalyzed C–H Bond Activation and Functionalization. *Chem. Rev.* **2012**, *112* (11), 5879–5918.
- (45) Dub, P. A.; Henson, N. J.; Martin, R. L.; Gordon, J. C. Unravelling the Mechanism of the Asymmetric Hydrogenation of Acetophenone by [RuX₂(Diphosphine)(1,2-Diamine)] Catalysts. *J. Am. Chem. Soc.* **2014**, *136* (9), 3505–3521.
- (46) Sandoval, C. A.; Ohkuma, T.; Muñiz, K.; Noyori, R. Mechanism of Asymmetric Hydrogenation of Ketones Catalyzed by BINAP/1,2-Diamine–Ruthenium(II) Complexes. *J. Am. Chem. Soc.* **2003**, *125* (44), 13490–13503.

- (47) Hamilton, R. J.; Bergens, S. H. An Unexpected Possible Role of Base in Asymmetric Catalytic Hydrogenations of Ketones. Synthesis and Characterization of Several Key Catalytic Intermediates. *J. Am. Chem. Soc.* **2006**, *128* (42), 13700–13701.
- (48) Hadzovic, A.; Song, D.; MacLaughlin, C. M.; Morris, R. H. A Mechanism Displaying Autocatalysis: The Hydrogenation of Acetophenone Catalyzed by RuH(S-Binap)(App) Where App Is the Amido Ligand Derived from 2-Amino-2-(2-Pyridyl)Propane. *Organometallics* **2007**, *26* (24), 5987–5999.
- (49) Neely, J. M.; Rovis, T. Rh(III)-Catalyzed Regioselective Synthesis of Pyridines from Alkenes and α,β -Unsaturated Oxime Esters. *J. Am. Chem. Soc.* **2013**, *135* (1), 66–69.
- (50) Oberg, K. M.; Lee, E. E.; Rovis, T. Regioselective Rhodium-Catalyzed Intermolecular [2+2+2] Cycloaddition of Alkynes and Isocyanates to Form Pyridones. *Tetrahedron* **2009**, *65* (26), 5056–5061.
- (51) Rooke, D. A.; Ferreira, E. M. Platinum-Catalyzed Hydrosilylations of Internal Alkynes: Harnessing Substituent Effects to Achieve High Regioselectivity. *Angew. Chem. Int. Ed.* **2012**, *51* (13), 3225–3230.
- (52) Duttwyler, S.; Lu, C.; Rheingold, A. L.; Bergman, R. G.; Ellman, J. A. Highly Diastereoselective Synthesis of Tetrahydropyridines by a C–H Activation–Cyclization–Reduction Cascade. *J. Am. Chem. Soc.* **2012**, *134* (9), 4064–4067.
- (53) Dalton, D. M.; Oberg, K. M.; Yu, R. T.; Lee, E. E.; Perreault, S.; Oinen, M. E.; Pease, M. L.; Malik, G.; Rovis, T. Enantioselective Rhodium-Catalyzed [2 + 2 + 2] Cycloadditions of Terminal Alkynes and Alkenyl Isocyanates: Mechanistic Insights

- Lead to a Unified Model That Rationalizes Product Selectivity. *J. Am. Chem. Soc.* **2009**, *131* (43), 15717–15728.
- (54) Saudan, L. A.; Saudan, C. M.; Debieux, C.; Wyss, P. Dihydrogen Reduction of Carboxylic Esters to Alcohols under the Catalysis of Homogeneous Ruthenium Complexes: High Efficiency and Unprecedented Chemoselectivity. *Angew. Chem.* **2007**, *119* (39), 7617–7620.
- (55) Spasyuk, D.; Smith, S.; Gusev, D. G. Replacing Phosphorus with Sulfur for the Efficient Hydrogenation of Esters. *Angew. Chem.* **2013**, *125* (9), 2598–2602.
- (56) Tominaga, K.; Sasaki, Y.; Watanabe, T.; Saito, M. Homogeneous Hydrogenation of Carbon Dioxide to Methanol Catalyzed by Ruthenium Cluster Anions in the Presence of Halide Anions. *Bull. Chem. Soc. Jpn.* **1995**, *68* (10), 2837–2842.
- (57) Rezayee, N. M.; Huff, C. A.; Sanford, M. S. Tandem Amine and Ruthenium-Catalyzed Hydrogenation of CO₂ to Methanol. *J. Am. Chem. Soc.* **2015**, *137* (3), 1028–1031.
- (58) Yang, X. Hydrogenation of Carbon Dioxide Catalyzed by PNP Pincer Iridium, Iron, and Cobalt Complexes: A Computational Design of Base Metal Catalysts. *ACS Catal.* **2011**, *1* (8), 849–854.
- (59) Li, Y.-N.; Ma, R.; He, L.-N.; Diao, Z.-F. Homogeneous Hydrogenation of Carbon Dioxide to Methanol. *Catal. Sci. Technol.* **2014**, *4* (6), 1498–1512.
- (60) Kothandaraman, J.; Goepfert, A.; Czaun, M.; Olah, G. A.; Prakash, G. K. S. Conversion of CO₂ from Air into Methanol Using a Polyamine and a Homogeneous Ruthenium Catalyst. *J. Am. Chem. Soc.* **2016**, *138* (3), 778–781.

- (61) Huff, C. A.; Sanford, M. S. Catalytic CO₂ Hydrogenation to Formate by a Ruthenium Pincer Complex. *ACS Catal.* **2013**, *3* (10), 2412–2416.
- (62) Huff, C. A.; Sanford, M. S. Cascade Catalysis for the Homogeneous Hydrogenation of CO₂ to Methanol. *J. Am. Chem. Soc.* **2011**, *133* (45), 18122–18125.
- (63) Kothandaraman, J.; Czaun, M.; Goepfert, A.; Haiges, R.; Jones, J.-P.; May, R. B.; Prakash, G. K. S.; Olah, G. A. Amine-Free Reversible Hydrogen Storage in Formate Salts Catalyzed by Ruthenium Pincer Complex without PH Control or Solvent Change. *ChemSusChem* **2015**, *8* (8), 1442–1451.
- (64) O. Reithmeier, R.; Meister, S.; Rieger, B.; Siebel, A.; Tschurl, M.; Heiz, U.; Herdtweck, E. Mono- and Bimetallic Ir(III) Based Catalysts for the Homogeneous Photocatalytic Reduction of CO₂ under Visible Light Irradiation. New Insights into Catalyst Deactivation. *Dalton Trans.* **2014**, *43* (35), 13259–13269.
- (65) Ahlquist, M. S. G. Iridium Catalyzed Hydrogenation of CO₂ under Basic Conditions—Mechanistic Insight from Theory. *J. Mol. Catal. Chem.* **2010**, *324* (1–2), 3–8.
- (66) Tanaka, R.; Yamashita, M.; Nozaki, K. Catalytic Hydrogenation of Carbon Dioxide Using Ir(III)–Pincer Complexes. *J. Am. Chem. Soc.* **2009**, *131* (40), 14168–14169.
- (67) Windle, C. D.; Perutz, R. N. Advances in Molecular Photocatalytic and Electrocatalytic CO₂ Reduction. *Coord. Chem. Rev.* **2012**, *256* (21–22), 2562–2570.
- (68) Li, Y.-N.; He, L.-N.; Liu, A.-H.; Lang, X.-D.; Yang, Z.-Z.; Yu, B.; Luan, C.-R. In Situ Hydrogenation of Captured CO₂ to Formate with Polyethyleneimine and Rh/Monophosphine System. *Green Chem.* **2013**, *15* (10), 2825–2829.

- (69) Wesselbaum, S.; vom Stein, T.; Klankermayer, J.; Leitner, W. Hydrogenation of Carbon Dioxide to Methanol by Using a Homogeneous Ruthenium–Phosphine Catalyst. *Angew. Chem.* **2012**, *124* (30), 7617–7620.
- (70) Li, Y.-N.; He, L.-N.; Lang, X.-D.; Liu, X.-F.; Zhang, S. An Integrated Process of CO₂ Capture and in Situ Hydrogenation to Formate Using a Tunable Ethoxyl-Functionalized Amidine and Rh/Bisphosphine System. *RSC Adv.* **2014**, *4* (91), 49995–50002.
- (71) Morris, A. J.; Meyer, G. J.; Fujita, E. Molecular Approaches to the Photocatalytic Reduction of Carbon Dioxide for Solar Fuels. *Acc. Chem. Res.* **2009**, *42* (12), 1983–1994.
- (72) Käß, M.; Friedrich, A.; Drees, M.; Schneider, S. Ruthenium Complexes with Cooperative PNP Ligands: Bifunctional Catalysts for the Dehydrogenation of Ammonia–Borane. *Angew. Chem. Int. Ed.* **2009**, *48* (5), 905–907.
- (73) Hull, J. F.; Himeda, Y.; Wang, W.-H.; Hashiguchi, B.; Periana, R.; Szalda, D. J.; Muckerman, J. T.; Fujita, E. Reversible Hydrogen Storage Using CO₂ and a Proton-Switchable Iridium Catalyst in Aqueous Media under Mild Temperatures and Pressures. *Nat. Chem.* **2012**, *4* (5), 383–388.
- (74) Gordon B. Haxel; Sara Boore; Susan Mayfield. Rare Earth Elements—Critical Resources for High Technology. U.S. Geological Survey November 20, 2002.
- (75) Bhattacharya, P.; Guan, H. Synthesis and Catalytic Applications of Iron Pincer Complexes. *Comments Inorg. Chem.* **2011**, *32* (2), 88–112.

- (76) Chakraborty, S.; Dai, H.; Bhattacharya, P.; Fairweather, N. T.; Gibson, M. S.; Krause, J. A.; Guan, H. Iron-Based Catalysts for the Hydrogenation of Esters to Alcohols. *J. Am. Chem. Soc.* **2014**, *136* (22), 7869–7872.
- (77) Werkmeister, S.; Junge, K.; Wendt, B.; Alberico, E.; Jiao, H.; Baumann, W.; Junge, H.; Gallou, F.; Beller, M. Hydrogenation of Esters to Alcohols with a Well-Defined Iron Complex. *Angew. Chem. Int. Ed.* **2014**, *53* (33), 8722–8726.
- (78) Zell, T.; Ben-David, Y.; Milstein, D. Unprecedented Iron-Catalyzed Ester Hydrogenation. Mild, Selective, and Efficient Hydrogenation of Trifluoroacetic Esters to Alcohols Catalyzed by an Iron Pincer Complex. *Angew. Chem.* **2014**, *126* (18), 4773–4777.
- (79) Langer, R.; Leitus, G.; Ben-David, Y.; Milstein, D. Efficient Hydrogenation of Ketones Catalyzed by an Iron Pincer Complex. *Angew. Chem.* **2011**, *123* (9), 2168–2172.
- (80) Bornschein, C.; Werkmeister, S.; Wendt, B.; Jiao, H.; Alberico, E.; Baumann, W.; Junge, H.; Junge, K.; Beller, M. Mild and Selective Hydrogenation of Aromatic and Aliphatic (Di)Nitriles with a Well-Defined Iron Pincer Complex. *Nat. Commun.* **2014**, *5*, 4111.
- (81) Hernandez-Perez, A. C.; Vlassova, A.; Collins, S. K. Toward a Visible Light Mediated Photocyclization: Cu-Based Sensitizers for the Synthesis of [5]Helicene. *Org. Lett.* **2012**, *14* (12), 2988–2991.
- (82) Canali, L.; Sherrington, D. C. Utilisation of Homogeneous and Supported Chiral Metal(Salen) Complexes in Asymmetric Catalysis. *Chem. Soc. Rev.* **1999**, *28* (2), 85–93.

- (83) Agustin, D.; Rima, G.; Gornitzka, H.; Barrau, J. (Schiff Base) Divalent Group 14 Element Species: Manganese and Iron Complexes (Salen)MMn(CO)₂(H₅-C₅H₅) (M₁₄ = Ge, Sn, Pb) and (Salen)SnFe(CO)₄. *Inorg. Chem.* **2000**, *39* (24), 5492–5495.
- (84) Nindakova, L. O.; Lebed', F. M.; Zamazei, A. Y.; Shainyan, B. A. New C₂-Symmetric Optically Active Salen Ligands and Their Cobalt(II) Complexes. Hydridoborate Reduction of Prochiral C=O and C=C Bonds. *Russ. J. Org. Chem.* **2007**, *43* (9), 1322–1329.
- (85) Lin, H.-C.; Huang, C.-C.; Shi, C.-H.; Liao, Y.-H.; Chen, C.-C.; Lin, Y.-C.; Liu, Y.-H. Synthesis of Alkynylated Photo-Luminescent Zn(II) and Mg(II) Schiff Base Complexes. *Dalton Trans.* **2007**, *0* (7), 781–791.
- (86) McDaniel, A. M.; Tseng, H.-W.; Damrauer, N. H.; Shores, M. P. Synthesis and Solution Phase Characterization of Strongly Photooxidizing Heteroleptic Cr(III) Tris-Dipyridyl Complexes. *Inorg. Chem.* **2010**, *49* (17), 7981–7991.
- (87) McDaniel, A. M.; Tseng, H.-W.; Hill, E. A.; Damrauer, N. H.; Rappé, A. K.; Shores, M. P. Syntheses and Photophysical Investigations of Cr(III) Hexadentate Iminopyridine Complexes and Their Tris(Bidentate) Analogues. *Inorg. Chem.* **2013**, *52* (3), 1368–1378.
- (88) Stevenson, S. M.; Shores, M. P.; Ferreira, E. M. Photooxidizing Chromium Catalysts for Promoting Radical Cation Cycloadditions. *Angew. Chem. Int. Ed.* **2015**, *54* (22), 6506–6510.

- (89) Benito-Garagorri, D.; Puchberger, M.; Mereiter, K.; Kirchner, K. Stereospecific and Reversible CO Binding at Iron Pincer Complexes. *Angew. Chem. Int. Ed.* **2008**, *47* (47), 9142–9145.
- (90) Alberico, E.; Sponholz, P.; Cordes, C.; Nielsen, M.; Drexler, H.-J.; Baumann, W.; Junge, H.; Beller, M. Selective Hydrogen Production from Methanol with a Defined Iron Pincer Catalyst under Mild Conditions. *Angew. Chem. Int. Ed.* **2013**, *52* (52), 14162–14166.
- (91) Zell, T.; Butschke, B.; Ben-David, Y.; Milstein, D. Efficient Hydrogen Liberation from Formic Acid Catalyzed by a Well-Defined Iron Pincer Complex under Mild Conditions. *Chem. – Eur. J.* **2013**, *19* (25), 8068–8072.
- (92) Langer, R.; Diskin-Posner, Y.; Leitun, G.; Shimon, L. J. W.; Ben-David, Y.; Milstein, D. Low-Pressure Hydrogenation of Carbon Dioxide Catalyzed by an Iron Pincer Complex Exhibiting Noble Metal Activity. *Angew. Chem. Int. Ed.* **2011**, *50* (42), 9948–9952.
- (93) Federsel, C.; Boddien, A.; Jackstell, R.; Jennerjahn, R.; Dyson, P. J.; Scopelliti, R.; Laurenczy, G.; Beller, M. A Well-Defined Iron Catalyst for the Reduction of Bicarbonates and Carbon Dioxide to Formates, Alkyl Formates, and Formamides. *Angew. Chem. Int. Ed.* **2010**, *49* (50), 9777–9780.
- (94) Bonin, J.; Robert, M.; Routier, M. Selective and Efficient Photocatalytic CO₂ Reduction to CO Using Visible Light and an Iron-Based Homogeneous Catalyst. *J. Am. Chem. Soc.* **2014**, *136* (48), 16768–16771.

- (95) Pirtsch, M.; Paria, S.; Matsuno, T.; Isobe, H.; Reiser, O. [Cu(Dap)₂Cl] As an Efficient Visible-Light-Driven Photoredox Catalyst in Carbon–Carbon Bond-Forming Reactions. *Chem. – Eur. J.* **2012**, *18* (24), 7336–7340.
- (96) Yang, X. Mechanistic Insights into Ruthenium-Catalyzed Production of H₂ and CO₂ from Methanol and Water: A DFT Study. *ACS Catal.* **2014**, *4* (4), 1129–1133.
- (97) Gross, E. K. U.; Kohn, W. Time-Dependent Density-Functional Theory. In *Advances in Quantum Chemistry*; Löwdin, P.-O., Ed.; Density Functional Theory of Many-Fermion Systems; Academic Press, 1990; Vol. 21, pp 255–291.
- (98) Sameera, W. M. C.; Maseras, F. Transition Metal Catalysis by Density Functional Theory and Density Functional Theory/Molecular Mechanics. *Wiley Interdiscip. Rev. Comput. Mol. Sci.* **2012**, *2* (3), 375–385.
- (99) Meylemans, H. A.; Damrauer, N. H. Controlling Electron Transfer through the Manipulation of Structure and Ligand-Based Torsional Motions: A Computational Exploration of Ruthenium Donor–Acceptor Systems Using Density Functional Theory. *Inorg. Chem.* **2009**, *48* (23), 11161–11175.
- (100) Salassa, L.; Garino, C.; Salassa, G.; Gobetto, R.; Nervi, C. Mechanism of Ligand Photodissociation in Photoactivable [Ru(Bpy)₂L₂]²⁺ Complexes: A Density Functional Theory Study. *J. Am. Chem. Soc.* **2008**, *130* (29), 9590–9597.
- (101) Jakubikova, E.; Snoeberger III, R. C.; Batista, V. S.; Martin, R. L.; Batista, E. R. Interfacial Electron Transfer in TiO₂ Surfaces Sensitized with Ru(II)–Polypyridine Complexes†. *J. Phys. Chem. A* **2009**, *113* (45), 12532–12540.

- (102) Roy, L. E.; Jakubikova, E.; Guthrie, M. G.; Batista, E. R. Calculation of One-Electron Redox Potentials Revisited. Is It Possible to Calculate Accurate Potentials with Density Functional Methods? *J. Phys. Chem. A* **2009**, *113* (24), 6745–6750.
- (103) Jakubikova, E.; Martin, R. L.; Batista, E. R. Systematic Study of Modifications to Ruthenium(II) Polypyridine Dyads for Electron Injection Enhancement. *Inorg. Chem.* **2010**, *49* (6), 2975–2982.
- (104) Neese, F.; Petrenko, T.; Ganyushin, D.; Olbrich, G. Advanced Aspects of Ab Initio Theoretical Optical Spectroscopy of Transition Metal Complexes: Multiplets, Spin-Orbit Coupling and Resonance Raman Intensities. *Coord. Chem. Rev.* **2007**, *251* (3–4), 288–327.
- (105) Lundqvist, M. J.; Nilsing, M.; Lunell, S.; Åkermark, B.; Persson, P. Spacer and Anchor Effects on the Electronic Coupling in Ruthenium-Bis-Terpyridine Dye-Sensitized TiO₂ Nanocrystals Studied by DFT. *J. Phys. Chem. B* **2006**, *110* (41), 20513–20525.
- (106) McDaniel, A. M.; Rappé, A. K.; Shores, M. P. Structural and Electronic Comparison of 1st Row Transition Metal Complexes of a Tripodal Iminopyridine Ligand. *Inorg. Chem.* **2012**, *51* (22), 12493–12502.
- (107) Ketkov, S.; Isachenkov, N.; Rychagova, E.; Tzeng, W.-B. Electronic Excited States of Chromium and Vanadium Bisarene Complexes Revisited: Interpretation of the Absorption Spectra on the Basis of TD DFT Calculations. *Dalton Trans.* **2014**, *43* (47), 17703–17711.

- (108) Mori, H.; Yamagishi, A.; Sato, H. Theoretical Study on Vibrational Circular Dichroism Spectra of Tris(Acetylacetonato)Metal(III) Complexes: Anharmonic Effects and Low-Lying Excited States. *J. Chem. Phys.* **2011**, *135* (8), 084506.
- (109) Fan, J.; Seth, M.; Autschbach, J.; Ziegler, T. Circular Dichroism of Trigonal Dihedral Chromium(III) Complexes: A Theoretical Study Based on Open-Shell Time-Dependent Density Functional Theory. *Inorg. Chem.* **2008**, *47* (24), 11656–11668.
- (110) Hoffert, W. A.; Rappé, A. K.; Shores, M. P. Topological and Electronic Influences on Magnetic Exchange Coupling in Fe(III) Ethynylbenzene Dendritic Building Blocks. *J. Am. Chem. Soc.* **2011**, *133* (51), 20823–20836.
- (111) Luo, S.; Averkiev, B.; Yang, K. R.; Xu, X.; Truhlar, D. G. Density Functional Theory of Open-Shell Systems. The 3d-Series Transition-Metal Atoms and Their Cations. *J. Chem. Theory Comput.* **2014**, *10* (1), 102–121.
- (112) Batista, E. R.; Martin, R. L. On the Excited States Involved in the Luminescent Probe [Ru(Bpy)2dppz]2+. *J. Phys. Chem. A* **2005**, *109* (14), 3128–3133.
- (113) Scalmani, G.; Frisch, M. J.; Mennucci, B.; Tomasi, J.; Cammi, R.; Barone, V. Geometries and Properties of Excited States in the Gas Phase and in Solution: Theory and Application of a Time-Dependent Density Functional Theory Polarizable Continuum Model. *J. Chem. Phys.* **2006**, *124* (9), 094107.
- (114) Jakubikova, E.; Chen, W.; Dattelbaum, D. M.; Rein, F. N.; Rocha, R. C.; Martin, R. L.; Batista, E. R. Electronic Structure and Spectroscopy of [Ru(Tpy)₂]²⁺, [Ru(Tpy)(Bpy)(H₂O)]²⁺, and [Ru(Tpy)(Bpy)(Cl)]⁺. *Inorg. Chem.* **2009**, *48* (22), 10720–10725.

- (115) Albert, V. V.; Badaeva, E.; Kilina, S.; Sykora, M.; Tretiak, S. The Frenkel Exciton Hamiltonian for Functionalized Ru(II)–bpy Complexes. *J. Lumin.* **2011**, *131* (8), 1739–1746.
- (116) Vlček, A.; Záliš, S. Modeling of Charge-Transfer Transitions and Excited States in D6 Transition Metal Complexes by DFT Techniques. *Coord. Chem. Rev.* **2007**, *251* (3), 258–287.
- (117) Ando, H.; Iuchi, S.; Sato, H. Theoretical Study on Ultrafast Intersystem Crossing of Chromium(III) Acetylacetonate. *Chem. Phys. Lett.* **2012**, *535*, 177–181.
- (118) Tsepis, A. C. DFT/TDDFT Insights into the Chemistry, Biochemistry and Photophysics of Copper Coordination Compounds. *RSC Adv.* **2014**, *4* (61), 32504–32529.
- (119) Jackson, T. A.; Rohde, J.-U.; Seo, M. S.; Sastri, C. V.; DeHont, R.; Stubna, A.; Ohta, T.; Kitagawa, T.; Münck, E.; Nam, W.; et al. Axial Ligand Effects on the Geometric and Electronic Structures of Nonheme Oxoiron(IV) Complexes. *J. Am. Chem. Soc.* **2008**, *130* (37), 12394–12407.
- (120) Bowman, D. N.; Blew, J. H.; Tsuchiya, T.; Jakubikova, E. Elucidating Band-Selective Sensitization in Iron(II) Polypyridine-TiO₂ Assemblies. *Inorg. Chem.* **2013**, *52* (15), 8621–8628.
- (121) Cramer, C. J.; Truhlar, D. G. Density Functional Theory for Transition Metals and Transition Metal Chemistry. *Phys. Chem. Chem. Phys.* **2009**, *11* (46), 10757–10816.
- (122) Casida, M. E.; Huix-Rotllant, M. Progress in Time-Dependent Density-Functional Theory. *Annu. Rev. Phys. Chem.* **2012**, *63* (1), 287–323.

- (123) Isegawa, M.; Truhlar, D. G. Valence Excitation Energies of Alkenes, Carbonyl Compounds, and Azabenzenes by Time-Dependent Density Functional Theory: Linear Response of the Ground State Compared to Collinear and Noncollinear Spin-Flip TDDFT with the Tamm-Dancoff Approximation. *J. Chem. Phys.* **2013**, *138* (13), 134111.
- (124) Becke, A. D. Density-functional Thermochemistry. III. The Role of Exact Exchange. *J. Chem. Phys.* **1993**, *98* (7), 5648–5652.
- (125) Zhao, Y.; Truhlar, D. G. Density Functional for Spectroscopy: No Long-Range Self-Interaction Error, Good Performance for Rydberg and Charge-Transfer States, and Better Performance on Average than B3LYP for Ground States. *J. Phys. Chem. A* **2006**, *110* (49), 13126–13130.
- (126) Kuritz, N.; Stein, T.; Baer, R.; Kronik, L. Charge-Transfer-Like $\Pi \rightarrow \pi^*$ Excitations in Time-Dependent Density Functional Theory: A Conundrum and Its Solution. *J. Chem. Theory Comput.* **2011**, *7* (8), 2408–2415.
- (127) Bowman, D. N.; Jakubikova, E. Low-Spin versus High-Spin Ground State in Pseudo-Octahedral Iron Complexes. *Inorg. Chem.* **2012**, *51* (11), 6011–6019.
- (128) Wang, T.-H.; Hsiao, C.-H.; Chen, S.-H.; Cheng, Y.-T.; Chen, L.-Y. DFT and TD-DFT Study on Structures, Related Energies, Frontier Molecular Orbitals and UV-Vis Spectra of $[M(\text{Tp})(\text{PPh}_3)(\text{Cl})(\text{L})]$ ($M = \text{Ru}$ and Fe ; $\text{L} = \text{C}_3\text{H}_4\text{N}_2$ and $\text{C}_{13}\text{H}_{11}\text{N}$). *Polyhedron* **2015**, *102*, 216–223.
- (129) Santoro, F.; Lami, A.; Improta, R.; Bloino, J.; Barone, V. Effective Method for the Computation of Optical Spectra of Large Molecules at Finite Temperature Including

the Duschinsky and Herzberg–Teller Effect: The Qx Band of Porphyrin as a Case Study. *J. Chem. Phys.* **2008**, *128* (22), 224311.

- (130) Bowman, A. C.; Sproules, S.; Wiegardt, K. Electronic Structures of the [V(Tbpy)₃]^z (z = 3+, 2+, 0, 1-) Electron Transfer Series. *Inorg. Chem.* **2012**, *51* (6), 3707–3717.

CHAPTER 2: BENCHMARKING TDDFT CALCULATIONS AND ITS APPLICATION TO PERIODIC AND LIGAND TRENDS¹

I. INTRODUCTION

The application of photocatalysis to organic reactions has led to a renaissance in organic transformations. Catalysts offer the potential for safer, milder, stereochemically controlled reactions without stoichiometric reagents, and thus less waste.¹ Upwards of 90% of industrially-produced chemicals require a catalyst. Ideally, there are several properties this catalyst would have. First, the photocatalyst should be able to catalyze a wide variety of organic reactions. The catalyst should be green; Earth-abundant materials should be used and the use of auxiliary agents should be eliminated. Lastly, there are huge environmental and economical incentives for developing a cheap Earth-abundant catalyst that would ideally be driven by sunlight.² The solar spectrum spans from about 300 nm beyond 800 nm. However the most intense amount of solar energy is present around 440-700 nm. An ideal catalyst would absorb in this region.³

Transition metal complexes have already been shown to catalyze photoredox reactions.⁴ In this process, the metal catalyst is initially excited and rapidly undergoes an intersystem crossing or significant structural distortion to a long lived excited state followed by an outer sphere electron transfer to or from the catalyst, beginning the oxidative or reductive process. Most of these photocatalysts/photoinitiators/photosensitizers are rare second and third row transition

¹ The work in this chapter was done by Collette M. Nite and David J. Boston. Collette M. Nite performed all theoretical calculations and analysis. David J. Boston is responsible for all experimental work, including the syntheses, and absorption spectra of the transition metal complexes. The text was written entirely by Collette M. Nite.

metals.⁵⁻⁸ In order for sustainable industrial photocatalytic processes to develop, these rare metals must be replaced by more abundant alternatives.

First row transition metals would be an ideal replacement as they are much more abundant. However, complications arise from moving to abundant first row transition metals.

First row transition metals are much more labile than second and third row transition metals. These metals' ability to exist in both high and low spin states with multiple oxidation states leads to higher densities of states with shorter lifetimes and diverse reactivity. Ligand lability and complicated excited state manifolds do not typically fare well for the same outer sphere mechanism that works so well for heavier transition metal complexes such as Ru(bpy)₃.⁹ However, there is potential to exploit these challenges in an inner sphere mechanism. For instance, ligand lability lends itself to weaker metal-ligand bonds, which have the potential to allow a substrate to bind and release from a catalyst. Also, first row transition metals' electron spin activity offers the possibility of controlling the electron spin and play the noninnocence to our advantage. An inner sphere scenario could potentially allow greater stereocontrol by controlling substrate activation. In addition, the need for sacrificial reagents could potentially be eliminated.

The properties of first row transition metal complexes are highly dependent on the nature of the coordinating ligands. Minor alterations to the complex can result in very different physical and electrochemical properties such as: the metal's coordination number, geometry, excited state lifetimes, magnetic properties, and chemical reactivity.^{10,11} It is thought that structural features of photocatalysts can be manipulated

to promote high catalytic efficiency by inducing long-lived excited state lifetimes resulting in efficient charge separation.

In terms of ligands, conjugation has been shown in literature to be of utmost importance for high absorption in the visible region. While the presence of a metal is important for absorption of higher energy visible light (i.e. 400-475 nm), conjugated aromatic systems such as organic dyes such like eosin Y8 or polypyridyl ligands as in $[\text{Ru}(\text{bpy})_3]^{2+}$ exhibit strong absorption bands due to $\pi \rightarrow \pi^*$ transitions.¹ Esters in conjunction with iminopyridines have also been shown to improve iminopyridine stability with increased charge transfer (CT) absorption.¹² Specifically, π systems are capable of π -stacking, which results in maximum delocalization and internal conversion for long lifetimes in a charge transfer mechanism. These π -stacking interactions also contributes to charge separation, as delocalization is necessary for quenching, collision pathways, and ground state binding.¹³ Polypyridyl ligand moieties are reputable for promoting metal to ligand charge transfer (MLCT), resulting in strong absorption bands with possibility of sufficient charge separation. Through the nitrogen electron-withdrawing atom of the pyridine, polypyridyl ligands most often result in the oxidation of the metal and reduction of the ligand. Ring rotation lowers excited state energies, resulting in delocalization and charge transfer.¹⁴ Therefore, aryl and polypyridyl type ligands have been heavily exploited in ligand design.

Complexes containing certain privileged class ligands bound to specific metals have shown great promise in replacing rare catalysts.¹⁵ Among these privileged ligand classes are Schiff base type ligands. Schiff bases are a general functional group containing a nitrogen-carbon double bond, with the nitrogen bonded to an alkyl or aryl

group. Aryl groups in general produce more stable and more readily synthesized Schiff bases, while alkyl groups are typically rather unstable. Schiff bases are easily prepared by the condensation between aldehydes and imines as shown in Figure 2.1.

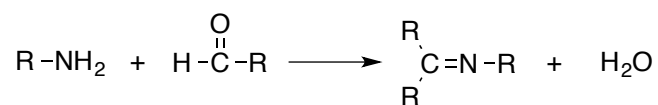


Figure 2.1: Schiff-base synthesis where Schiff base is formed from condensation reaction between an amine and an aldehyde.

The nitrogen in the imine group acts as a π -acceptor, which is valuable for coordinating to the metal center. Schiff bases are “privileged” in that they are characterized for having easy reaction conditions that can be used to prepare libraries of complexes where small changes in metal and ligand structure can be characterized for better understanding. Schiff bases have the ability to stabilize many different metals in various oxidation states and tune ligands through the use of a variety of amines and aldehydes for synthesis. Chiral Schiff bases have the additional ability to transmit chiral information for asymmetric catalysis. Therefore, catalytic screening has centered around the Schiff base moiety.¹⁵

A specific type of Schiff base ligand with high catalytic activity and enantioselectivity is the salen ligand. Salen ligands are synthesized by a reaction of salicylaldehyde or salicylaldehyde derivatives with C_2 symmetric 1,2 diamines, shown in Figure 2.2.^{15,16} The general salen structure exhibits C_2 symmetry. Chiral C_2 and C_3 (as in $[\text{Ru}(\text{bpy})_3]^{2+}$) symmetric complexes have received much attention for asymmetric catalysis, as they reduce the number of possible transition states.¹⁰ When coordinated

to a metal center, salens are classified as a [O,N,N,O] tetradentate ligand, with 4 coordinating sites with π -accepting atoms, and 2 axial sites where organic molecules such as CO₂ can bind. NH and OH groups can facilitate metal coordination and shift reduction potentials to mechanistically tune photocatalytic reactions.¹⁷ A derivative of the salen ligand, known as the salophen ligand, has a phenyl group in the R₂ position. Salophen ligands were also screened, to determine the relationship between conjugation and absorption. The structure of the salophen ligand is shown in Figure 2.3.

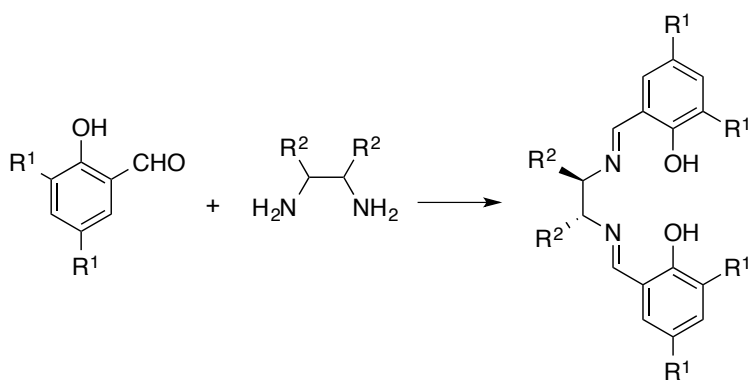


Figure 2.2: Salen-type ligand synthesis from reaction with salicylaldehyde derivative and a 1,2 diamine.

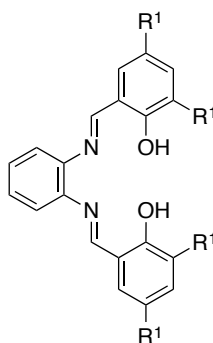


Figure 2.3: Salophen ligand backbone.

Due to 1st row transition metal's sensitivity to ligands, manipulating complexes for mechanistic tuning is in the details. Ligand flexibility is not only dependent on the type of ligand but also on the metal center, its size, and its oxidation state.¹⁵ Ligands with

sterically bulky groups (e.g. polypyridines, aromatics) can be used to tune coordination number, geometry, physical properties and chemical reactivity. Bulky groups near the coordination site have been shown to enhance the catalytic reactivity of Schiff base metal catalysts.¹⁰ In addition, sterics strongly affect packing, which has great effect on electronic properties, such as collision pathways and absorption.¹¹

Theoretical electronic structure methods are a good way to screen these photocatalytic complexes, as calculations can give useful insight into these systems for selective tuning. Density functional theory (DFT)^{18,19} and time dependent density functional theory (TDDFT)²⁰ methods are capable of calculating large molecular systems. In order to explore first row transition metals and different ligand manifolds with TDDFT, it is vital that our method is well optimized in order to ensure good experimental overlap. Benchmark calculations were carried out on select groups of complexes in order to determine the best functional and basis set to be used for this class of complexes.

II. BENCHMARKING

Due to the fact that DFT is an approximation method without any inherent variational qualities to aid in picking out the exchange correlation (XC) functional, benchmarking between different basis sets and functionals is vital. XC functionals are system specific and it is important to understand what qualities of a system are being measured.²¹

Basis sets on the other hand are much more systematic and do scale variationally. A basis set in quantum chemistry is the expression for molecular orbitals as a linear combination of atomic orbitals, ϕ_v , given in Eq. (2.1).

$$\psi = \sum_v^K c_v \phi_v \quad (2.1)$$

As such, larger basis sets (which add in more atomic orbitals) more accurately represent molecular orbitals, resulting in a more accurate calculation. However, adding in more basis functions means more integrals must be solved, increasing the computational time for the calculation. Therefore the smallest basis set that accurately describes the chemical system is selected. This often requires benchmarking to determine how many functions are needed to describe the system well.

An orbital is a one electron wavefunction. For the hydrogen atom, the correct shape of the orbital is calculated with a Slater orbital, characteristic of the exponential, $e^{-\zeta r}$, where ζ is a constant derived from the effective nuclear charge, and r is nucleus–electron distance. While this orbital encompasses the correct behavior, those integrals are notoriously difficult to solve for multi-center systems. Therefore, Gaussian type orbitals with the exponential term, $e^{-\alpha r^2}$, where α was set to mimic a Slater type orbital shape, were shown to be a reasonable substitute for Slater type orbitals. In order to mimic Slater behavior, Pople showed that a linear combination of Gaussian orbitals could be used. Gaussian basis sets are now almost exclusively used by quantum chemists, due to their computational ease. There are many classes of basis sets, but here we will just outline the basis sets used in our benchmarking calculations.

Pople developed a notation for Gaussian orbitals consisting of A-BCG, in which A, B, and C are integers and G implies that this is a Gaussian type basis set. The hyphen indicates that the basis is split into valence and non-valence functions (small and large exponents, respectively). A indicates the number of primitive Gaussians

combined to account for the non-valence (core) orbitals. B and C both indicate the number of primitive Gaussian functions combined for the valence orbitals. B represents the more compact functions and C represents the more extended functions. To account for polarization, where orbitals distort from an atomic shape upon molecule formation, functions of a higher angular momentum, l , can be included. This is indicated by an asterisk, *. One asterisk * indicates that d functions have been added to p atomic orbitals; two asterisks ** indicates that p functions have been added to the hydrogen 1s orbital as well. Diffuse functions, which describe electrons that are far from the nucleus, can also be accounted for in Pople basis sets. These diffuse functions are indicated by a + sign before the G. For our benchmarking purposes we used Pople basis sets 6-31G*, 6-311G*, and 6-311+G*.

Another class of basis set are the correlation consistent (cc) basis sets, cc-pVDZ and cc-pVTZ. These basis sets were developed for calculations that include electron correlation. Correlation of electron position/momentum allows electrons to be near nuclei while maximizing the distance between the electrons. The pVDZ and pVTZ stand for polarized valence double zeta and triple zeta, respectively. cc-pVDZ adds 1s and 1p and 1d function to the set of atomic functions. cc-pVTZ additionally adds another s, p, d, and f function. For our benchmarking we included the cc-pVTZ basis function, which is larger than the Pople basis functions used.

The XC functionals that have been developed for DFT vary widely and must be carefully selected for a given molecular system. The photocomplexes studied here are comprised of transition metals with large ligand manifolds. All XC functionals we benchmarked are hybrid XC functionals. Hybrid XC functionals are range-separated

functionals that include a percentage of exact exchange from Hartree-Fock. This exact exchange is important for long-range character, as HF is a long range approximation method. The most ubiquitous hybrid functional used today is B3LYP.

The XC functionals that we benchmarked for our systems are B3LYP^{22,23}, APF-D²⁴, M11²⁵, and ω B97X-D²⁶. While all four are hybrid functionals, APF-D and ω B97X-D functionals both account for dispersion, which is thought to be important for the weak, long range interactions of these complexes. Dispersion is the weak induced dipole-induced dipole attraction between electrons typically omitted in DFT approaches. The ω B97X-D XC functional incorporates range-separation to account for long range character associated with charge transfer in the complex.

Basis sets and functionals were benchmarked using a low valent Cr(III) and high valent Ni(II) complex with H₂thb(5,6,7,8-tetrahydrotribenzo[b,f,1][1,4,8,11]tetraazacyclotetradecine (THB) in Figure 2.4.

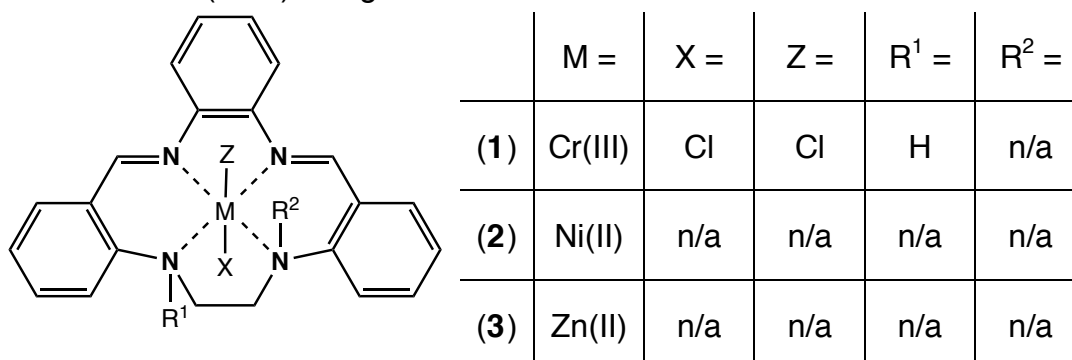


Figure 2.4: Cr(III) and Ni(II) THB complex structures used for benchmarking XC functionals and basis sets in DFT/TDDFT calculations.

This complex encompasses a lot of qualities that are important in screening our functionals: transition metals with both high valent and low valent character, a large π system exhibiting $\pi \rightarrow \pi^*$ transitions, electron withdrawing groups and a flexible geometry.

All four basis sets were first used in calculating the Ni(II) complex (**2**) in Figure 2.4. Theoretical absorption spectra for complex (**2**) calculated with the four basis sets are compared in Figure 2.5.

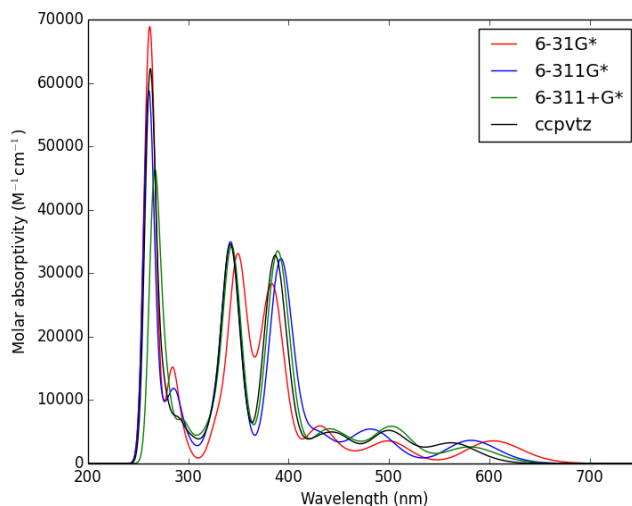


Figure 2.5: Comparison of basis set effect on the theoretical TDDFT absorption spectrum of Ni(II) complex (**2**) using the APFD XC functional.

All basis sets qualitatively described the same absorption characteristics, varying only slightly in excited state energies and oscillator strengths. The basis set, 6-31G* (red) overestimated oscillator strengths in the higher energy regions and underestimated oscillator strengths in visible region. 6-311G* (blue), 6-311+G* (green) and cc-pVTZ (black) basis sets showed very similar absorption patterns, varying in the oscillator strengths of the intense peak at $\lambda \sim 265$ nm. While the intensities are different, a natural transition orbital (NTO) analysis showed that basis sets predict similar behavior, characterizing intense absorption peaks as $\pi \rightarrow \pi^*$ transitions.

The following Table 2.1 compares the total energy and the energy difference of a given basis set relative to the largest basis set used, cc-pVTZ. In looking at the total energies of the complexes calculated using different basis sets listed in Table 2.1, cc-pVTZ had the lowest overall total energy. Through the variational principle, it can be

concluded that using basis set cc-pVTZ provides the most accurate calculation. The cc-pVTZ basis set is the largest, most diffuse, and accordingly computationally expensive basis set. Due to the relatively small -147.5 kcal/mol total energy difference between the calculations run with the 6-311+G* and cc-pVTZ basis sets as well as these two diffuse basis sets showing similar spectral characteristics and geometry, it was concluded that the basis set 6-311+G* was comparable to cc-pVTZ. For more accurate results, 6-311+G* basis set should be used instead of 6-31g*.

Table 2.1: The total energy of Ni(II) complex (**2**) as calculated with DFT with XC functional APF-D for different basis sets and the energy difference between different Pople basis sets and largest basis set, cc-pVTZ.

Basis set	E(Hartree)	ΔE from basis set cc-pVTZ (kcal/mol)
6-31G*	-2575.46194023	366.4380638
6-311G*	-2575.77975291	167.0096536
6-311+G*	-2575.81080989	147.5213055
cc-pVTZ	-2576.04590248	0

To provide a comparison for a low valent open shell system, Cr(III) complex (**1**) in Figure 2.4 was also benchmarked. To compare basis sets, the theoretical absorption spectra in Figure 2.6 were used. Again, each basis set encapsulates a similar trend. However, for high energy states there are some slight discrepancies for the smaller basis sets around 320 nm. In addition, the smaller basis sets are slightly blueshifted at around 490 nm.

Natural transition orbitals (NTOs) were used to characterize the electronic transition of the excited state. Through a diagonalization of the transition density matrix transformed over occupied and virtual orbitals, NTOs show where the electron came from and where the electron went to for a given transition. To compare how the

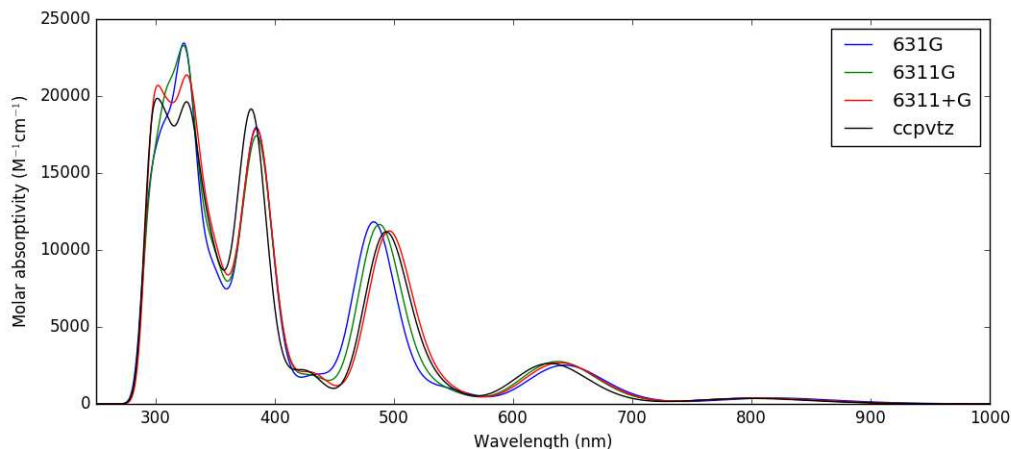


Figure 2.6: Comparison of basis sets effect on the theoretical TDDFT absorption spectrum of Cr(II) complex (**1**) using the APF-D XC functional.

transitions are depicted in the orbitals, Figure 2.7 shows the difference in natural transition orbital density for the excited state at around 640 nm as compared to the largest basis set, cc-pVTZ.

While there is very little difference in where the electron came from and where the electron went to in the transitions for the larger basis sets, there is quite a bit of disparity between the electron density of the calculation using the basis set 6-31G* and cc-pVTZ as evident by the large amount of electron density shown in the 6-31G* difference plot compared to the other basis set plots. A small basis set such as 6-31G* should not be used for these complex systems.

Figure 2.8 compares computational time in CPUs for calculating 48 TDDFT excited states of Cr(III) complex (**1**) for all four basis sets. While the largest basis set, cc-pVTZ, is the most accurate in describing the system, there is a large computational cost for the increased basis functions. Because 6-311+G* compared so well with cc-pVTZ, while taking only a little more than half the computational time, it was concluded

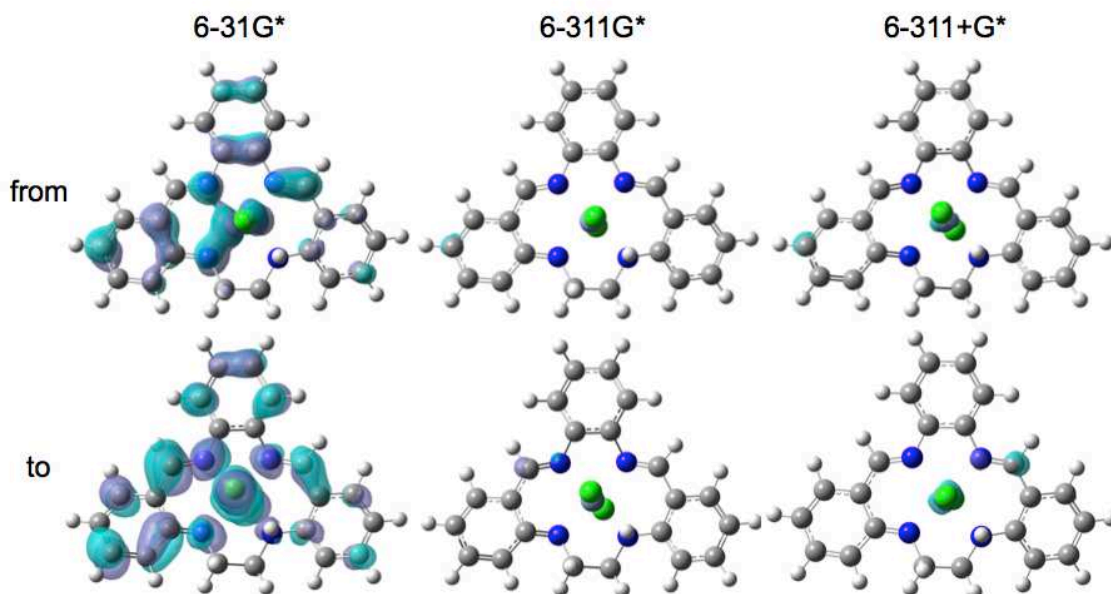


Figure 2.7: The electron density difference plots for a set of NTOs for Cr(III) complex **(1)** for the three Pople basis sets, 6-31G*, 6-311G*, and 6-311+G*, as compared to the largest basis set cc-pVTZ. The top row depicts difference of where the electron came from and the bottom row depicts the difference of where the electron went to in the excitation at around 640 nm as compared to cc-pVTZ basis set.

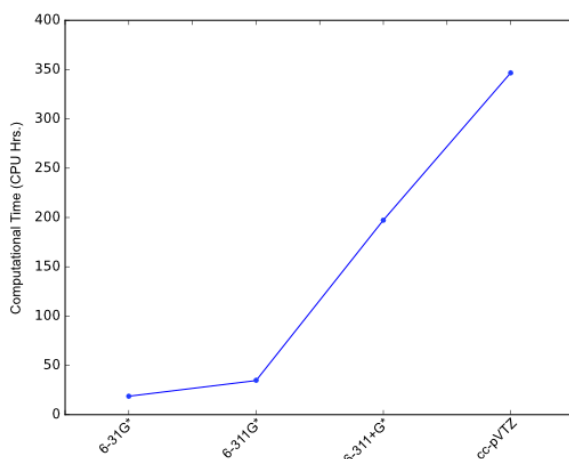


Figure 2.8: Computational time in CPU hours versus basis sets 6-31G*, 6-311G*, 6-311+G*, and cc-pVTZ for calculating 48 excited states of the Cr(III) complex **(1)** using TDDFT with the APF-D XC functional.

that for these large systems the basis set 6-311+G* (which includes both polarization and diffuse functions) should be used.

In 2012, Austin, Petersson, and Frisch published a paper on the development of a new DFT functional, APF-D,²⁴ with a dispersion correction that more accurately described weak long-range interactions. The computational results for weak interactions described by this hybrid functional are comparable to CCSD(T) method with diffuse basis functions, aug-cc-pVTZ. The structures of Ni(II) complex (**2**) and Zn(II) complex (**3**) were optimized with hybrid functionals B3LYP and APF-D with 6-311+G* basis set. It was shown that for all complexes, B3LYP underestimated the excited state energies, where the APF-D spectrum was consistently blue-shifted. The TDDFT spectra are depicted in Figure 2.9.

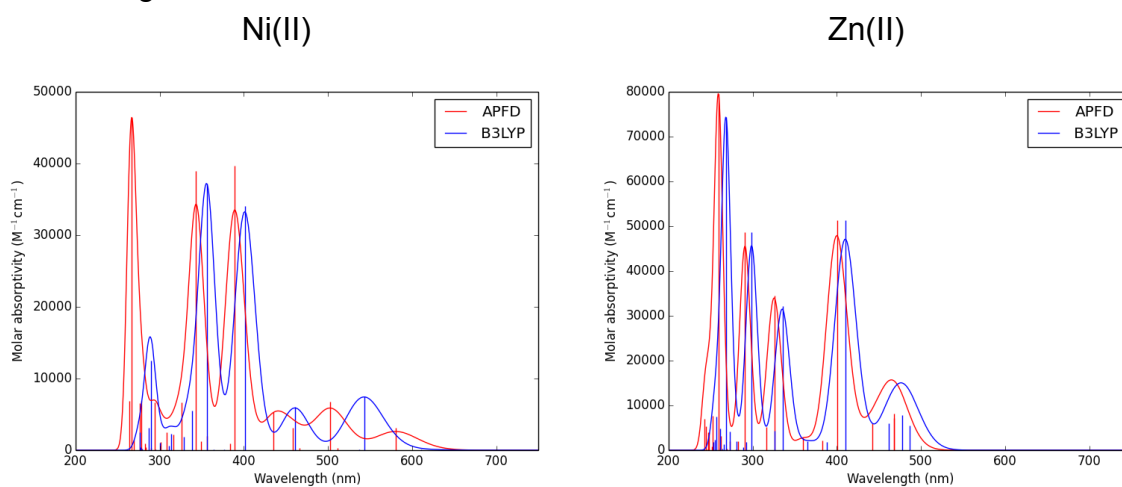


Figure 2.9: TDDFT absorption spectra of complexes (**2**) (left) and (**3**) (right) comparing hybrid XC functionals, APF-D (red) and B3LYP (blue). Basis set 6-311+G* was used in all cases.

Theoretical spectra of the Ni(II) complex (**2**) calculated with XC functionals APF-D and B3LYP is compared to the experimental spectrum of this complex in Figure 2.10. The experimental spectrum was obtained in dimethylformamide (DMF) solvent.

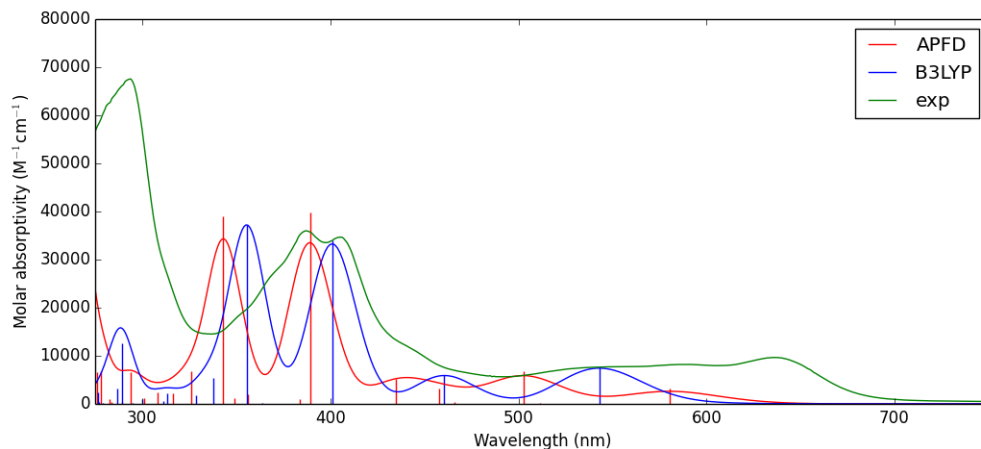


Figure 2.10: Theoretical absorption spectra of Ni(II) complex (2) using APF-D (red) and B3LYP (blue) XC functionals with implicit DMF solvent with experimental spectrum of Ni(II) complex (2) in DMF solvent (green).

Theoretical B3LYP and APF-D spectra were generated from calculations with implicit dimethylformamide (DMF) solvent in order to compare to experimental trends.

Interpretation of functional effect on the correlation between theoretical and experimental spectra was difficult due to many convoluted variables, including solvent effects. Because APF-D and B3LYP spectra show similar behavior, general characterization of excited states can typically be deduced from either hybrid functional. However, it is important to describe energy more correctly, and it is assumed that in order to do so, dispersion must be accounted for. Consequently, the APF-D functional was applied for later calculations to improve results over the B3LYP functional for inclusion of dispersion interaction.

For the low valent Cr(III) complex, XC functionals B3LYP, APF-D, ω B97X-D, and M11 were benchmarked (using basis set 6-311+G*) and the resulting absorption spectra is below in Figure 2.11. As seen in Figure 2.11, the different XC functionals give very different results for the same Cr(III) system. B3LYP and APF-D are the most

similar, with APF-D again being blue shifted as compared to B3LYP. All functionals show different results for the high energy states below 400 nm. Perhaps most striking though is that ω B97X-D and M11 do not show any significant character of the low energy states, past 500 nm. This is troubling when we are concerned with transition metals and low energy visible transitions.

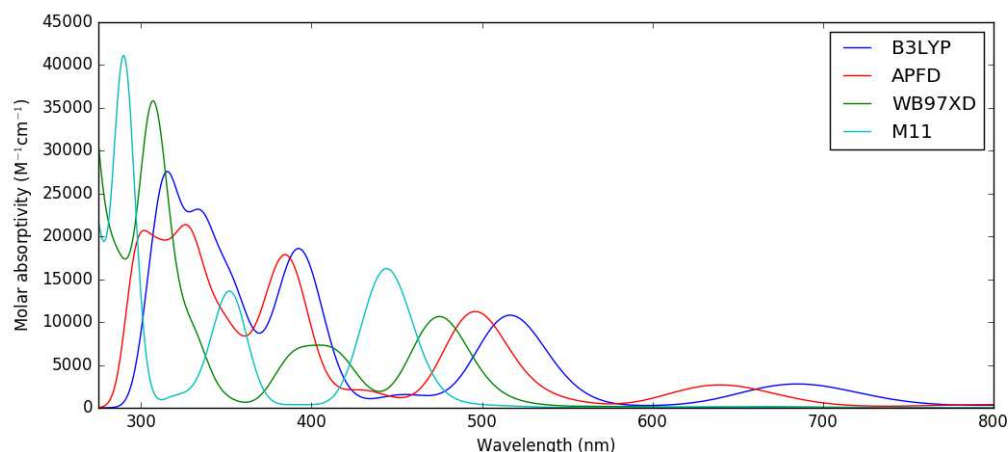


Figure 2.11: TDDFT absorption spectra with molar absorptivity ($M^{-1}cm^{-1}$) vs. wavelength (nm) of Cr(III) complex (**1**) comparing XC correlation functionals B3LYP (blue), APF-D (red), ω B97X-D (green), and M11 (aqua). Basis set 6-311+G* was used in all cases.

Figure 2.12 shows the spectrum of each functional for the Cr(III) complex (**1**) as compared to the experimental spectrum of the Cr(III) complex (shown in black). The experimental spectrum does indeed have low energy excitations that must be accounted for. The blue shifted APF-D functional corresponds to experimental peak positions better than B3LYP as seen at 650 nm, 500 nm, and 300 nm.

For the rest of the calculations, our method will utilize the 6-311+G* basis set with the APF-D XC functional.

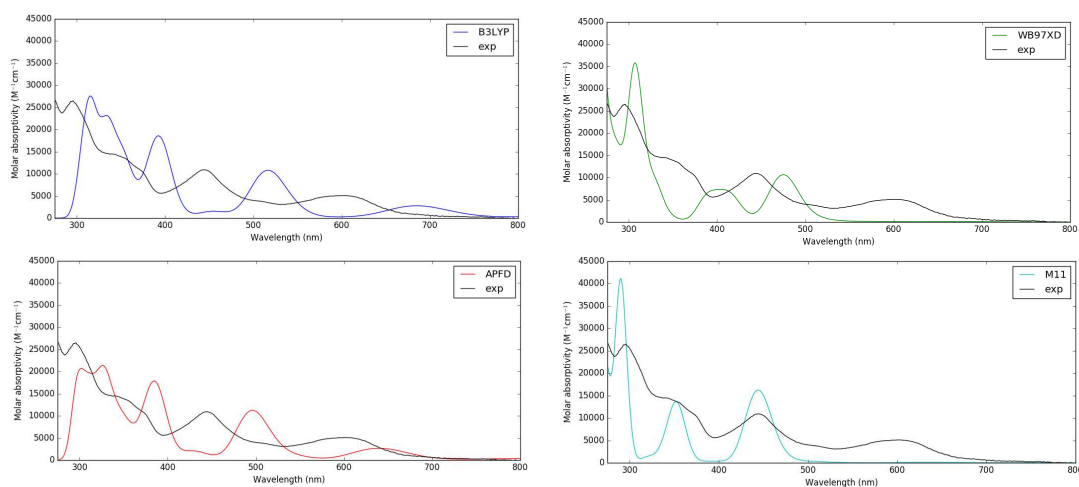


Figure 2.12: TDDFT absorption spectra of Cr(III) complex (**1**) using XC correlation functionals B3LYP (blue: top left), APF-D (red: bottom left), ω B97X-D (green: top right), and M11 (aqua: bottom right) as compared to the experimental spectrum of Cr(III) complex (**1**) in DMF. Basis set 6-311+G* and implicit solvent DMF was used in all cases.

III. METHODS

Restricted and unrestricted hybrid self-consistent field (SCF) density functional theory (DFT) and time-dependent DFT (TD-DFT) calculations were carried out using the Gaussian09 suite of electronic structure codes. Complexes were calculated using hybrid functional APF-D in order to account for intramolecular dispersion forces, as well as a more diffuse basis set, 6-311+G*, in attempt to better describe long range charge transfer character.

To account for solvent associated with experimental spectra, the polarized continuum model (PCM) was used, describing the solvent implicitly. The solvent was accounted for through implicit polarized continuum solvent model with integral equation formalism variant (IEF-PCM). DMF solvent was used, corresponding to experimental work on complexes.

It should be noted that our theoretical spectra comparison to experimental spectra does include implicit solvent (DMF in this case) using the polarized continuum model (PCM). Spectral comparison of the solvent effect shows that including the DMF solvent captures higher intensities and blue shifted energies further matching experimental results as seen in Figure 2.13.

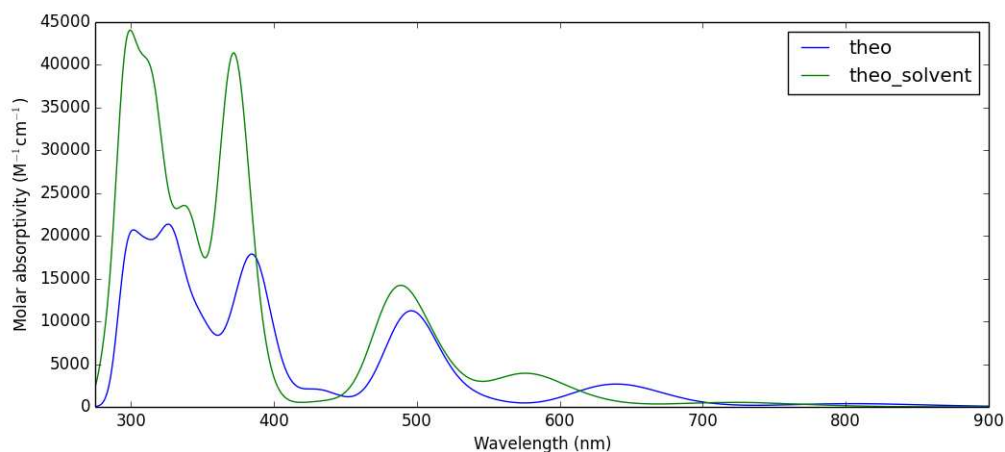


Figure 2.13: TDDFT(APF-D/6-311+*) spectra of Cr(III)THB complex (**1**) with and without implicit DMF solvent.

Following optimization of the ground state, TD-DFT calculation of the first 48 excited states of each complex was carried out. The TD-DFT calculations were run under the assumption that vertical excitation is a rapid process in which the molecule's excited state geometry and ground state geometry are the same. If solvent is involved, it is assumed that the process is too rapid for the solvent to have time to fully respond as well. This procedure is known as a non-equilibrium procedure, in which the TD calculation is run directly from the optimization of the ground state, without optimizing the excited state. The TD-DFT calculation produces excited state energies, wavelengths, and oscillator strengths, and orbital character of the 48 excited states, which were used for further analysis.

Excitation energy and oscillator strength results from the TD-DFT excited state calculations were used to generate theoretical spectra. The theoretical spectra were produced through a python program. The energies in nm and oscillator strengths of the 48 excited states resulting from TDDFT calculation were plotted on the spectrum in the form of bars. This program simulated the absorption spectra by convoluting the spectrum, where the two functions are the excited state energies (eV) and oscillator strengths (unitless) from the TD-DFT calculation, with a Gaussian line shape with a 0.219 eV line width. In order to acquire intensities in molar absorptivity, ϵ , the resultant spectra were scaled by a factor of $1/4.32 \times 10^{-9}$ due to the relationship between oscillator strength (f) and molar absorptivity (ϵ) given in Eq. (2.2):

$$f = 2303 \frac{mc_0^2}{N_A \pi e^2 n} \int \epsilon(\bar{\nu}) d\bar{\nu} = \frac{4.32 \times 10^{-9}}{n} \int \epsilon(\bar{\nu}) d\bar{\nu} \quad (2.2)$$

where c_0 is the speed of light, m and e are the mass and the charge of an electron, respectively, N_A is Avogadro's number, n is the index of refraction, and $\bar{\nu}$ is the wavenumber (in cm^{-1}).³⁴ The theoretical spectra were readily compared to corresponding experimental spectra.

In order to better understand what was happening to the electrons in the complexes at each absorption band, a natural transition orbital (NTO) analysis was done. Interpreting the characteristics of the excited states can be very difficult, due to the complex-mixture of orbital nature of the excited states. The TD-DFT calculation results in a set of coefficients describing the contribution each particle-hole pair makes on the excited state. However, determining the physical origin of the electronic transitions from these excitation amplitudes is difficult. A pair of unoccupied and occupied natural transition orbitals (NTOs) representing the "hole" and the "electron",

respectively, is generated by diagonalizing the transition density matrix correlating the ground and excited state. By decomposing the transition density matrix into three contributions (an unoccupied matrix, the diagonalized transition density matrix, and a virtual matrix), a compact physical NTO representation correlating where the electron came from in the ground state and where the electron went to in the excited state is derived. The NTOs provide a pictorial description, which allows for a straightforward characterization of the excited state electron transfer (i.e. MC, MLCT, LMCT, $\pi \rightarrow \pi^*$).

IV. RESULTS AND DISCUSSION

In the beginning of our work, a wide variety of conjugated complexes were surveyed in effort to determine ligand trends. Late transition metals, Ni(II), Cu(II) and Zn(II) were studied in efforts to understand ligand trends without complex spin state manifolds. Ligand properties were represented with the Zn(II) complexes since Zn(II) has a full set of d orbitals. In addition, late transition metals are prone to square planar salen type complexes.

In looking specifically at ligand systems, the Schiff base type ligand with imine groups (in black) was compared to hydrogen substituted tertiary amine groups (in orange) in the Zn(II) complexes shown in Figure 2.14. As it can be seen, there is a much brighter absorption for the Zn(II) Schiff base complex as compared to its amine counterpart. By having the imine C=N double bond, the conjugation of the ligand is completed, yielding much brighter $\pi \rightarrow \pi^*$ transitions. While the absorption of this Zn(II) Schiff base type complex does not extend far into the visible region, it was thought that this is where the metal's d orbitals of a different first row transition metal would come into play. By switching out the metal in a common ligand scaffold, the absorption

spectrum changes rather drastically, as seen for a Schiff base tripodal ligand derivative with a nitrogen bridge as seen in Figure 2.15. The theoretical absorption spectra are also shown.

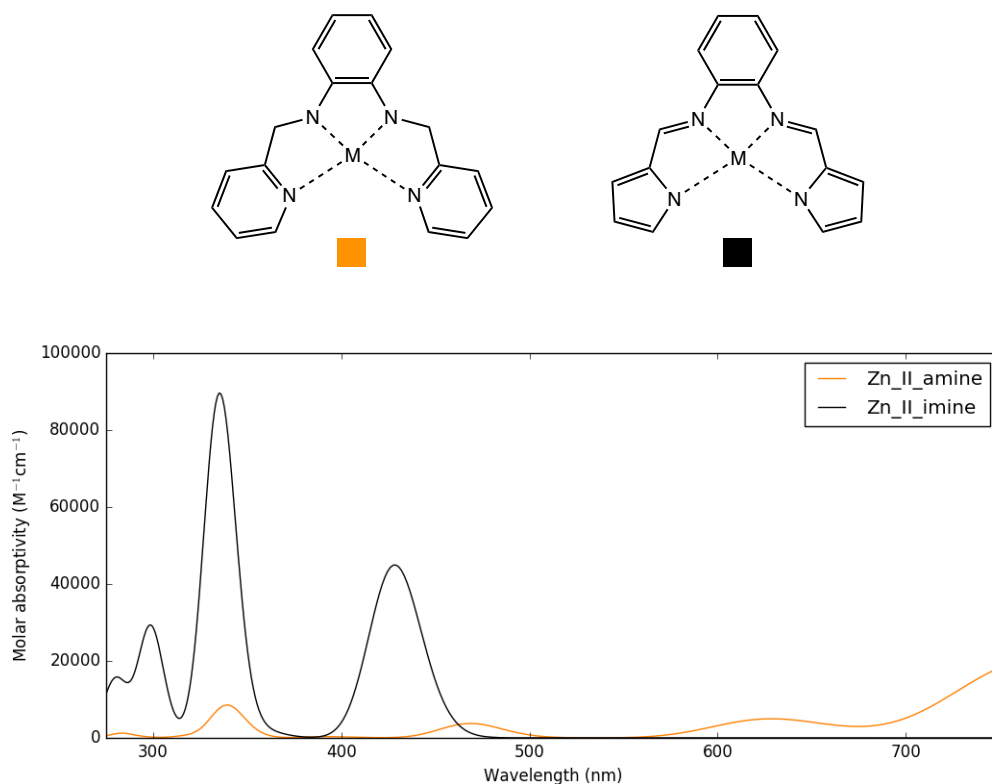


Figure 2.14: Zn(II) Schiff base type complex (black) as compared to a Zn(II) hydrogen substituted tertiary amine type complex (orange) via the TDDFT(APF-D/6-311+G*) absorption spectra with molar absorptivity ($M^{-1}cm^{-1}$) versus wavelength (nm).

While the Zn(II) complex does not extend past 400 nm into the visible region, other metals with the same ligand extend far into the visible region. Most notably, the V(II) and Co(III) complexes show a fair amount of absorption at around 630 nm and 460 nm, respectively. These spectra showed great promise in the ability to selectively tune a ligand with a given metal for optimal spectrochemical properties.

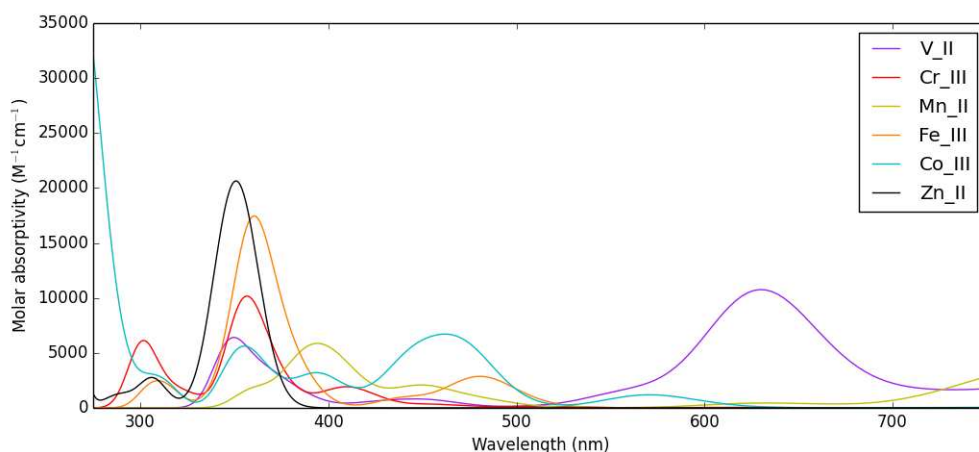
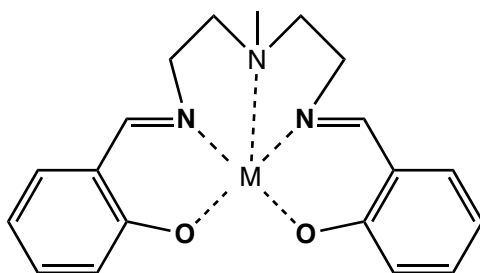


Figure 2.15: The TDDFT absorption spectra of a Schiff base tripodal complex with metals V(II), Cr(III), Mn(II), Fe(III), Co(III), and Zn(II) with molar absorptivity ($M^{-1}cm^{-1}$) versus wavelength(nm).

Following extensive literature on a specific Schiff base class, the salen complexes, we decide to explore the salen ligand in Figure 2.16. The salen ligand complexes in a square planar fashion, so we focused on Ni(II), Cu(II) and Zn(II) complexes. For these three complexes, the theoretical spectra are depicted in Figure 2.17. All three complexes have a similar absorption peak at around 350 nm. Ni(II) and Cu(II) both extend further into the visible region, albeit the absorption of these transitions is rather weak. Modifications to the ligand were explored in order to enhance this absorption.

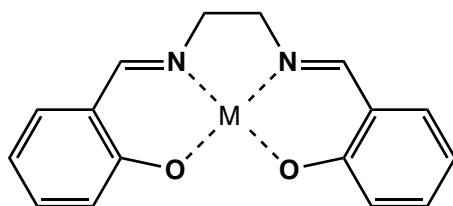


Figure 2.16: Salen ligand complexed to metal

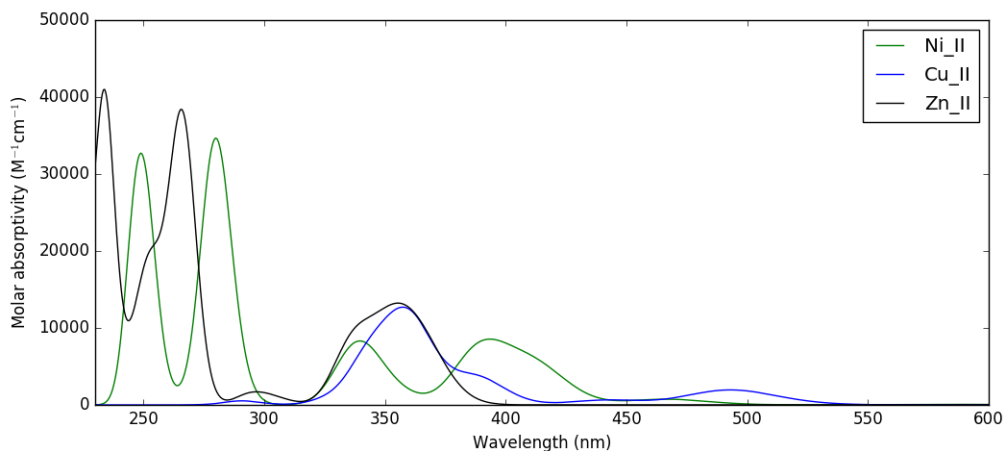


Figure 2.17: The TDDFT (APF-D/6-311+G*) absorption spectra of the salen complex with high valent metals Ni(II), Cu(II), and Zn(II).

The coordinating nitrogen and oxygen atoms were modified (alternating nitrogen and oxygen atoms) in order to determine the effect and importance of those electron-withdrawing groups. By substituting the oxygen atoms for nitrogen atoms, the following theoretical absorption spectra were obtained in Figure 2.18.

For all three complexes, the nitrogen-substituted complexes are redshifted, pushing the absorption further into the visible region. For the Cu(II) complex, while both salen type complexes had a fair peak at around 510 nm, the nitrogen-substituted complex had a much broader absorption with more excited states from around 390-500 nm. Most promising was the Ni(II) nitrogen substituted salen complex, where a broad absorption peak around 500 nm emerges. NTOs of the excited state of the Zn(II)

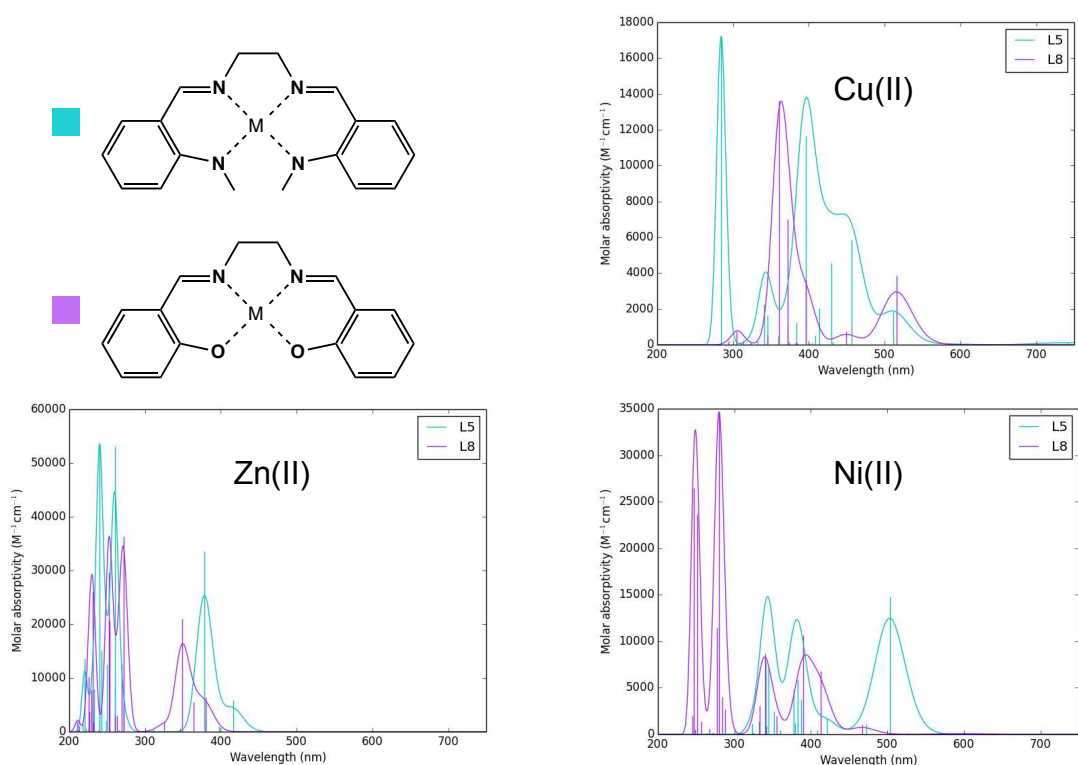
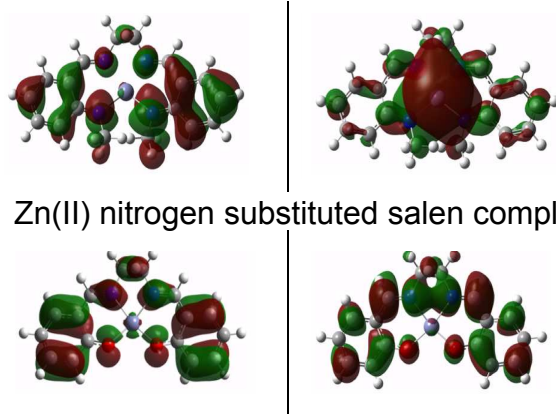


Figure 2.18: The TDDFT (APF-D/6-311+G*) absorption spectra of the salen (purple) and nitrogen substituted salen (aqua) complexes with metals Ni(II), Cu(II), and Zn(II).

nitrogen substituted salen complex at 260 nm and to the excited state of Zn(II) salen complex at 271 nm are compared in the following Figure 2.19.

Comparison of NTOs of the original salen to the nitrogen modified salen complex showed that there was much more electron density on the nitrogen coordinating groups than the oxygen coordinating groups, elucidating that nitrogen is a more active coordinating group. This gives rationale to the intense peak shifts to the spectra in Figure 2.18.

Following up on these observations, other first row transition metals were screened with this four nitrogen coordinated salen derivative, and the absorption spectra were calculated in Figure 2.20.



Excited state of Zn(II) nitrogen substituted salen complex at $\lambda = 260$ nm

Excited state of the Zn(II) salen complex at $\lambda = 271$ nm

Figure 2.19: NTOs for the Zn(II) nitrogen substituted salen complex (top) and the Zn(II) salen complex (bottom). The left image shows where the electron came from during the excitation and the right image shows where the electron went to during excitation.

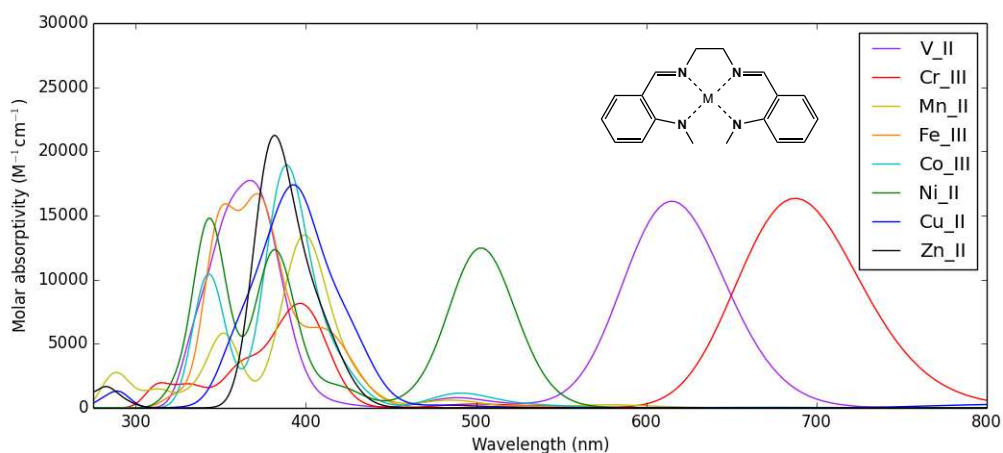


Figure 2.20: TDDFT(APF-D/6-311+G*) absorption spectra of nitrogen coordinated salen complex with metals V(II), Cr(III), Mn(II), Fe(III), Co(III), Ni(II), Cu(II), and Zn(II).

All metals for the given complex showed similar absorption in the near UV region from around 320-420 nm. Most complexes besides Zn(II) continued a little into the visible region. Ni(II) has a prominent absorption peak centered at 500 nm. Most striking were the absorption peaks at around 610 nm and 690 nm of the V(II) and Cr(III) complexes, respectively. These complexes with excitation further out into the visible

region could conceivably provide the photochemical properties we are looking for in this exploration.

While the salen complexes gave us fair results, we desired to continue pressing forward for increased intensity in visible absorption. Therefore, the salophen ligand along with other ethyl bridge substitutions on the salen ligand were explored following these results. Figure 2.21 below compares the theoretical absorption of the salen ligand (in green), the modified isopropanol bridging ligand (in orange), and the salophen ligand (in purple) complexed with Zn(II).

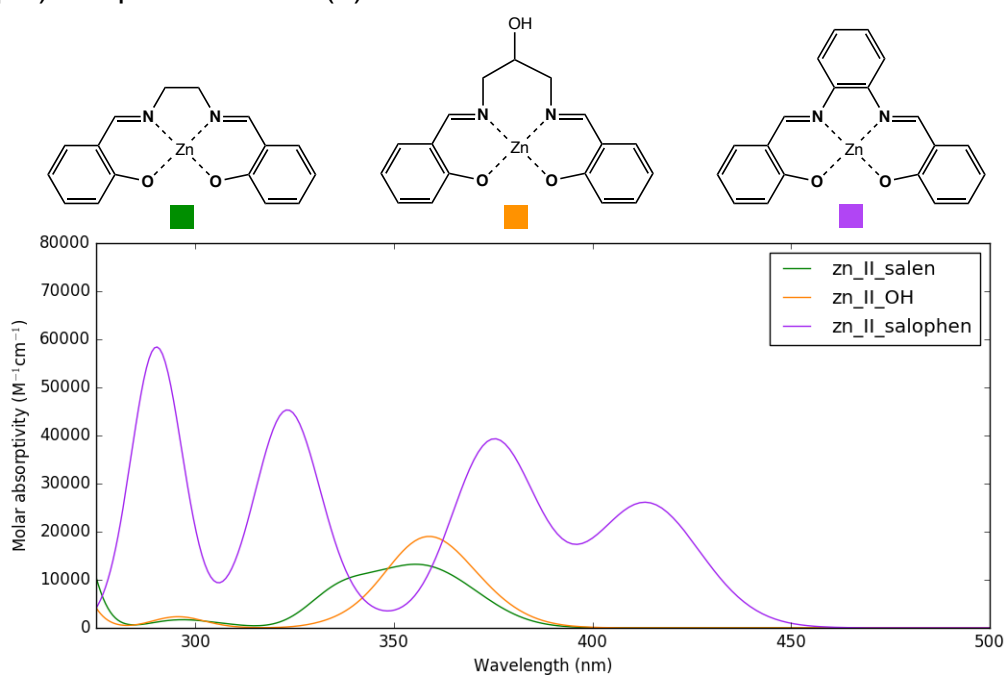


Figure 2.21: TDDFT (APF-D/6-311+G*) absorption spectra of Zn(II) salen (green), a modified isopropanol bridging derivative (orange) and salophen (purple) complex.

While substitution of the salen ethyl bridge for an isopropanol bridge showed similar absorption, the salophen ligand with the aryl substitution of the ethyl bridge resulted not only in a more intense absorption throughout, but also significantly extended the absorption into the visible region. While the first two complexes'

absorption features end at 400 nm, the further conjugated salophen complex has two broad peaks centered at around 375 nm and 425 nm. As we can presume from the results in Figure 2.21, a metal substitution of the salophen complex could extend this absorption further into the visible region.

The next ligand modification was the adaptation of the salophen ligand to a four nitrogen coordinated salophen derivative with an ethyl bridge connecting the two nitrogen amines, closing the system (see Figure 2.22). This adaptation was inspired by other macrocyclic systems such as porphyrins.

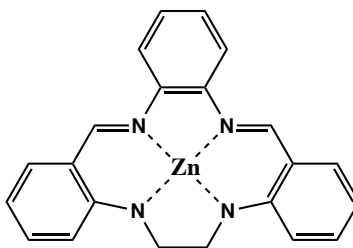


Figure 2.22: Zn(II)THB complex with a nitrogen ethyl bridge enclosing the system.

Figure 2.23 summarizes the progression of the studied ligands through their absorption spectra. The green spectrum shows the original Schiff base complex with a peak centered around 350 nm. By moving specifically to the salen complex (red spectrum), the absorption peak at around 350 nm is slightly broadened. By substituting the oxygen atoms for nitrogen atoms in the salen complex (blue spectrum), the spectrum is red shifted towards the visible region, with a broader peak now centered at around 390 nm. In moving to the salophen ligand (purple spectrum), multiple broad peaks arise that are more intense and further into the visible region (the furthest centered around 425 nm). By modifying the salophen complex to a macrocycle (black

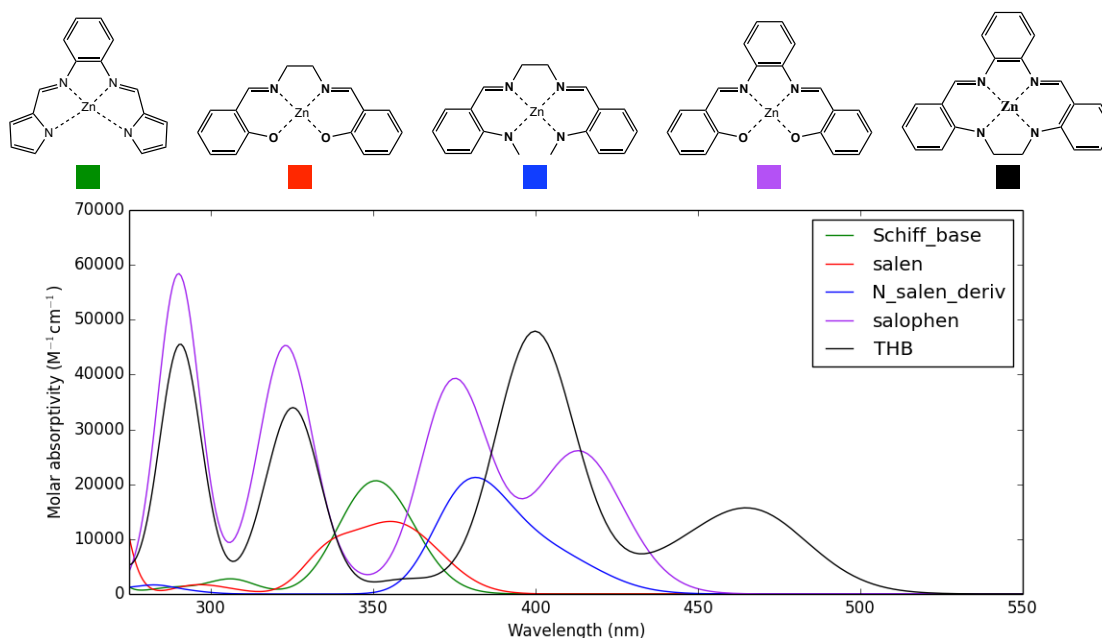


Figure 2.23: A comparison of the TDDFT (APF-D/6-311G*) absorption spectra of Zn(II) complexes, showing the progression of ligand design.

spectrum) the absorption moves appreciably into the visible region, with the most intense peak centered around 400 nm, and another substantial peak at around 470 nm.

V. CONCLUSION

TDDFT is a critical tool for studying the excited states of first row transition metal complexes. Benchmarking functionals and basis sets is a vital step in ensuring that calculations accurately represent experimental reality. It was concluded that for these large transition metal complexes, the hybrid exchange correlation functional that contains a dispersion term, APF-D, should be used with a large diffuse basis set, 6-311+G*.

Through ligand and metal screening, a catalyst can be tuned to promote strong absorption intensities in the visible region, which is important for a photocatalyst to harness sunlight. In studying ligand properties, it was shown that modification of the

ligand has a drastic effect on the photochemical properties of a system. With metal substitution, we believe this ligand manifold could be very favorable for our future endeavors in developing an inner sphere photocatalyst. By replacing Zn(II) with V(II) or Cr(III) which prefer octahedral geometry as to square planar, sacrificial axial ligands could be substituted to the desired bound reagent to enable the inner sphere electron transfer mechanism.

REFERENCES

- (1) Tucker, J. W.; Stephenson, C. R. J. Shining Light on Photoredox Catalysis: Theory and Synthetic Applications. *J. Org. Chem.* **2012**, *77* (4), 1617–1622.
- (2) Yoon, T. P.; Ischay, M. A.; Du, J. Visible Light Photocatalysis as a Greener Approach to Photochemical Synthesis. *Nat. Chem.* **2010**, *2* (7), 527–532.
- (3) Qiang, F. Radiation (Solar). *Elsevier Sci. Ltd* **2003**, 1859–1863.
- (4) Cieřła, P.; Kocot, P.; Mytych, P.; Stasicka, Z. Homogeneous Photocatalysis by Transition Metal Complexes in the Environment. *J. Mol. Catal. Chem.* **2004**, *224* (1–2), 17–33.
- (5) Alberico, E.; Nielsen, M. Towards a Methanol Economy Based on Homogeneous Catalysis: Methanol to H₂ and CO₂ to Methanol. *Chem. Commun.* **2015**, *51* (31), 6714–6725.
- (6) Ischay, M. A.; Anzovino, M. E.; Du, J.; Yoon, T. P. Efficient Visible Light Photocatalysis of [2+2] Enone Cycloadditions. *J. Am. Chem. Soc.* **2008**, *130* (39), 12886–12887.
- (7) Tucker, J. W.; Nguyen, J. D.; Narayanam, J. M. R.; Krabbe, S. W.; Stephenson, C. R. J. Tin-Free Radical Cyclization Reactions Initiated by Visible Light Photoredox Catalysis. *Chem. Commun.* **2010**, *46* (27), 4985–4987.
- (8) Werkmeister, S.; Neumann, J.; Junge, K.; Beller, M. Pincer-Type Complexes for Catalytic (De)Hydrogenation and Transfer (De)Hydrogenation Reactions: Recent Progress. *Chem. – Eur. J.* **2015**, *21* (35), 12226–12250.

- (9) Narayanam, J. M. R.; Stephenson, C. R. J. Visible Light Photoredox Catalysis: Applications in Organic Synthesis. *Chem. Soc. Rev.* **2011**, *40* (1), 102.
- (10) Gibson, S. E.; Castaldi, M. P. C₃ Symmetry: Molecular Design Inspired by Nature. *Angew. Chem. Int. Ed.* **2006**, *45* (29), 4718–4720.
- (11) McDaniel, A. M.; Rappé, A. K.; Shores, M. P. Structural and Electronic Comparison of 1st Row Transition Metal Complexes of a Tripodal Iminopyridine Ligand. *Inorg. Chem.* **2012**, *51* (22), 12493–12502.
- (12) McDaniel, A. M.; Tseng, H.-W.; Hill, E. A.; Damrauer, N. H.; Rappé, A. K.; Shores, M. P. Syntheses and Photophysical Investigations of Cr(III) Hexadentate Iminopyridine Complexes and Their Tris(Bidentate) Analogues. *Inorg. Chem.* **2013**, *52* (3), 1368–1378.
- (13) Consiglio, G.; Failla, S.; Finocchiaro, P.; Oliveri, I. P.; Di Bella, S. An Unprecedented Structural Interconversion in Solution of Aggregate Zinc(II) Salen Schiff-Base Complexes. *Inorg. Chem.* **2012**, *51* (15), 8409–8418.
- (14) Meylemans, H. A.; Lei, C.-F.; Damrauer, N. H. Ligand Structure, Conformational Dynamics, and Excited-State Electron Delocalization for Control of Photoinduced Electron Transfer Rates in Synthetic Donor-Bridge-Acceptor Systems. *Inorg. Chem.* **2008**, *47* (10), 4060–4076.
- (15) Cozzi, P. G. Metal-Salen Schiff Base Complexes in Catalysis: Practical Aspects. *Chem. Soc. Rev.* **2004**, *33* (7), 410.
- (16) Nindakova, L. O.; Lebed', F. M.; Zamazei, A. Y.; Shainyan, B. A. New C₂-Symmetric Optically Active Salen Ligands and Their Cobalt(II) Complexes.

- Hydridoborate Reduction of Prochiral C=O and C=C Bonds. *Russ. J. Org. Chem.* **2007**, 43 (9), 1322–1329.
- (17) McDaniel, A. M.; Klug, C. M.; Shores, M. P. Synthesis of Functionalized Hexadentate Iminopyridine FeII Complexes – Toward Anion-Dependent Spin Switching in Polar Media. *Eur. J. Inorg. Chem.* **2013**, 2013 (5–6), 943–950.
- (18) Hohenberg, P.; Kohn, W. Inhomogeneous Electron Gas. *Phys. Rev.* **1964**, 136 (3B), B864–B871.
- (19) Kohn, W.; Sham, L. J. Self-Consistent Equations Including Exchange and Correlation Effects. *Phys. Rev.* **1965**, 140 (4A), A1133–A1138.
- (20) Runge, E.; Gross, E. K. U. Density-Functional Theory for Time-Dependent Systems. *Phys. Rev. Lett.* **1984**, 52 (12), 997–1000.
- (21) Casida, M. E.; Huix-Rotllant, M. Progress in Time-Dependent Density-Functional Theory. *Annu. Rev. Phys. Chem.* **2012**, 63 (1), 287–323.
- (22) Becke, A. D. Density-functional Thermochemistry. III. The Role of Exact Exchange. *J. Chem. Phys.* **1993**, 98 (7), 5648–5652.
- (23) Lee, C.; Yang, W.; Parr, R. G. Development of the Colle-Salvetti Correlation-Energy Formula into a Functional of the Electron Density. *Phys. Rev. B* **1988**, 37 (2), 785–789.
- (24) Austin, A.; Petersson, G. A.; Frisch, M. J.; Dobek, F. J.; Scalmani, G.; Throssell, K. A Density Functional with Spherical Atom Dispersion Terms. *J. Chem. Theory Comput.* **2012**, 8 (12), 4989–5007.
- (25) Peverati, R.; Truhlar, D. G. Improving the Accuracy of Hybrid Meta-GGA Density Functionals by Range Separation. *J. Phys. Chem. Lett.* **2011**, 2 (21), 2810–2817.

(26) Chai, J.-D.; Head-Gordon, M. Long-Range Corrected Hybrid Density Functionals with Damped Atom–atom Dispersion Corrections. *R. Soc. Chem.* **2008**, *10*, 6615–6620.

CHAPTER 3: UNRAVELING THE SOURCE OF INTERSYSTEM CROSSING OF CHROMIUM BIPYRIDINE TYPE COMPLEXES¹

I. INTRODUCTION

The development of photoredox catalysis as a synthetically useful tool¹⁻³ and the maturation of dye sensitized solar cells⁴ have revitalized interest in the photophysics of metal polypyridyl complexes. The design of photocatalysts requires knowledge on both the photophysics and photochemistry of a system in order to understand how the complex is absorbing photons as well as interacting with substrates.⁵ In order to enhance the photocatalyst, the excitation pathways must be properly understood.

Transition metal complexes provide a rich array of excited states generally characterized as being ligand field (LF), metal to ligand charge transfer (MLCT), or ligand to metal charge transfer (LMCT). For first row transition metal complexes, the lowest energy transitions are very weak LF transitions with more intense MLCT and LMCT transitions at higher energy. The spectroscopy of second row transition metal complexes tends to be dominated by charge transfer transitions. Photoexcitation of polypyridyl metal complexes such as Ru(II)(bipy)₃ typically result in the population of higher MLCT excited states that undergo internal conversion to eventually populate the lower, longer-lived excited states.⁵ Classic models for transitions, based on organic

¹ The work in this chapter was done by Collette M. Nite, Anthony K. Rappé, Jacob M. Nite, and Romeo Portillo. Collette M. Nite and Anthony K. Rappé calculated the optimized structures for all complexes including the chromium complexes as well as the TDDFT excited states, absorption spectra, Franck-Condon analysis and NEVPT2 calculations. Jacob M. Nite calculated the vibrational distortion plots, including the structure alignments. Romeo Portillo provided the experimental spectrum of Cr(III)(bpy)₃. Collette M. Nite contributed solely to the text of the chapter.

molecules, subscribe to the notion that the rates of reactions follow the progression of a fast vibrational relaxation within an excited state, followed by an internal conversion to lower excited states of the same spin and then an intersystem crossing ($k_{vib} > k_{IC} > k_{ISC}$) to an alternate, typically triplet, spin state. Ru(II)(bipy)₃ generally follows this pattern with the exception that the lowest energy long lived excited state(s) is a spin-orbital coupled admixture of states. As described in 1970 by König and Herzog⁶ the spectroscopy of Cr(III)(bipy)₃ is more complex. The nominally d-d transitions expected to be observed in the 400-460 nm region were ascribed as being too intense to be LF transitions. Further, they displayed pronounced vibrational structure, which was considered anomalous for LF transitions. The authors characterized these transitions as having limited charge-transfer character.⁶

This anomalous 400-460 nm feature was subsequently reported for Cr(III)(NH₃)₄(bipy) and Cr(III)(NH₃)₂(bipy)₂, and Cr(III)(NH₃)₄(phen).⁷ In order to understand the nature of this portion of the electronic spectrum, a TD-DFT and NEVPT2 calculational study has been carried out on Cr(III)(NH₃)₄(bipy) and Cr(III)(bipy)₃. In addition, a vibronic analysis of the lowest energy allowed transition for Cr(III)(NH₃)₄(bipy) was performed. The theoretical methodology is described in section II, results and discussion are presented in section III, and the derived conclusions are presented in section IV.

II. THEORETICAL METHODOLOGY

All DFT calculations were carried out in the G16 suite of electronic structure codes.⁸ The geometry of Cr(III)(bpy)₃ quartet ground state was optimized using DFT with both APF-D⁹ and ω B97X-D¹⁰ XC functionals with a 6-311+G* basis set. The lowest

12 excited states were calculated using TDDFT as these lowest electronic states contained the states of interest while reducing computational costs. The electronic absorption spectra were generated using the oscillator strengths and peak positions from the TDDFT calculation. Each electronic state was convoluted with a Gaussian line shape with a linewidth of 0.093 eV at the full-width half-maximum as an approximate average excited state linewidth.

For Cr(III)(NH₃)₄(bpy), quartet ground state was optimized using DFT with APF-D/6-311+G*. The first 12 excited states were calculated with TDDFT. The geometry of the first excited state from the TDDFT calculation was then optimized. Frequency calculations of the ground state and the first excited state were performed. The vibronic spectrum for the lowest excited state were reproduced using the Franck-Condon-Herzberg-Teller analysis using ground state and TDDFT 1st excited state vibrational frequencies for a one photon absorption as prescribed by Santoro et al.¹¹

The ground state singlet S₀ and first triplet excited state T₁ of the isolated bipyridine ligand was optimized using APF-D/6-311+G*. A frequency calculation was performed on the S₀ and T₁ states. The distortion coordinate of the displacement between the ground state and the excited state was projected onto the normal vibrational modes for the ground state, twisted cis bipyridine conformation, flat cis bipyridine, and the excited state of Cr(III)(NH₃)₄(bpy) and Cr(III)(bpy)₃. An NTO analysis was also done on the first excited state of these systems in order to describe the character of the orbitals.¹²

The spin character of the electrons was evaluated by examining the spin-determinants from CASSCF calculations using the ORCA 4.0.1 suite of electronic

structure codes.¹³ An active space of CAS(5,5) and CAS(5,7) were used for Cr(III)(bpy)₃ and Cr(III)(NH₃)₄(bpy), respectively, using a cc-pVDZ basis set. The converged CAS wavefunctions were used in an NEVPT2 calculation to get the final orbital energies.

III. RESULTS AND DISCUSSION

The experimental spectrum of Cr(III)(bpy)₃ is shown in Figure 3.1. The theoretical spectra calculated with TDDFT (APF-D shown in blue/ ω B97X-D shown in green) corroborates the experimental spectra. The experimental peaks are centered at around 305, 345, and 430 nm. While the functional ω B97X-D blue shifted the spectrum with corresponding peaks at 285, 378, and 405 nm respectively, the excited states calculated with APF-D have excellent agreement with the experimental spectrum, with peaks centered around 306, 344, and 425 nm, respectively. APF-D best reproduced the spectrum and therefore was used as the XC functional going forward.

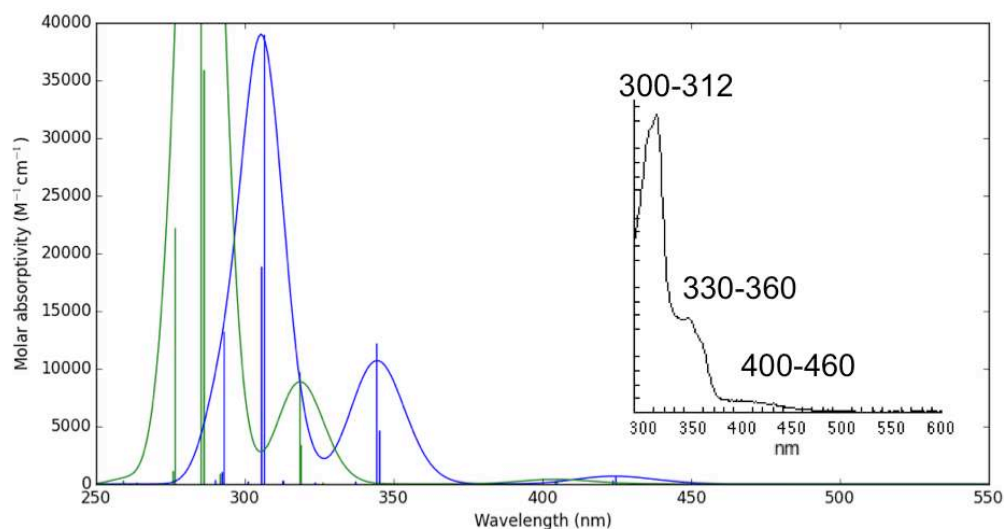


Figure 3.1: TDDFT absorption spectra of Cr(III)(bpy)₃ with APF-D (blue) and ω B97X-D (green) XC functional with basis set 6-311+G* (left). The experimental spectrum of Cr(III)(bpy)₃ is also included (right).

The most intriguing portion of the spectrum with respect to photocatalysis is the feature at around 425 nm, traditionally considered part of the $d \rightarrow d$ transition manifold. As observed by König and Herzog in 1970, this transition should not readily be observed, and therefore concluded that vibrational transitions within the bipy ligands are coupling with the chromium $d \rightarrow d$ transitions in order to observe this feature. As also noted by König and Herzog, vibrational features on $d \rightarrow d$ bands of first row transition metals are rarely observed experimentally.⁶ Therefore, there is high incentive to study these transitions computationally.

The purely electronic spectrum of $\text{Cr(III)(NH}_3)_4(\text{bpy})$ calculated with TDDFT and the APF-D functional is shown in Figure 3.2. The first excited state at 435 nm is characterized by its electronic intensity and convoluted with a symmetric Gaussian function. No vibronic character is included. This depiction is lacking in its description of the vibronic character of this complex. The experimental spectra of $\text{Cr(III)(NH}_3)_n(\text{bipy})_m$ published by Josephsen and Schäffer depicted several vibrational peaks dependent on the number of bipy ligands present in the complex.⁷

The vibronic features observed for the lowest excited state of $\text{Cr(III)(NH}_3)_4(\text{bpy})$ were reproduced using a Franck-Condon-Herzberg-Teller analysis using the ground state and TDDFT first excited state vibrational frequencies.¹¹ The vibronic spectrum is in Figure 3.3.

The vibronic spectrum of the first excited state of $\text{Cr(III)(NH}_3)_4(\text{bpy})$ is far superior in resolving the true behavior of the complex. Additional information can help understand the nature of this excited state.

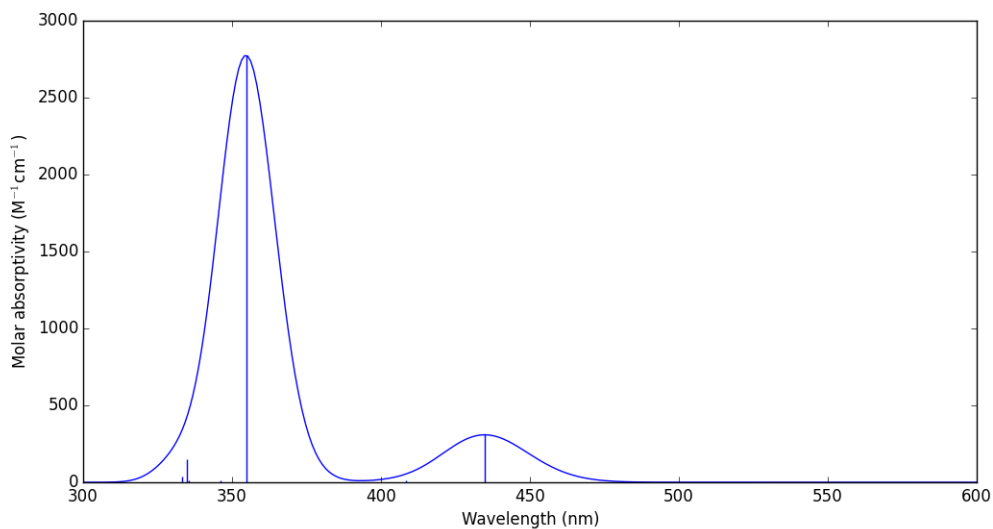


Figure 3.2: Pure electronic spectrum of $\text{Cr(III)(NH}_3)_4(\text{bpy})$ calculated with TDDFT (APF-D/6-311+G*).

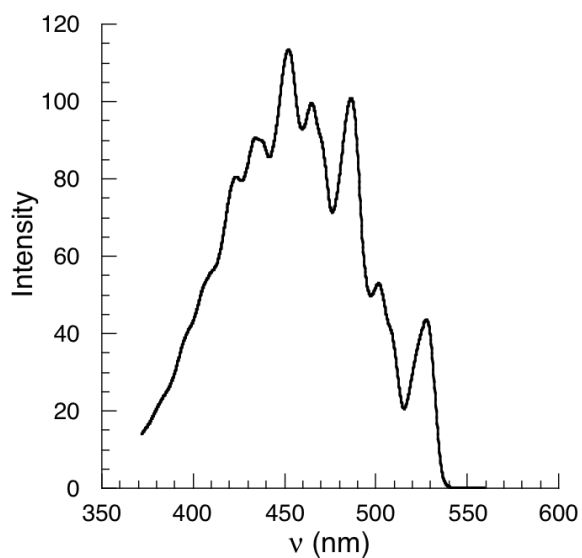


Figure 3.3: The vibronic spectrum of the first excited state $\text{Cr(III)(NH}_3)_4(\text{bpy})$ as calculated using DFT/TDDFT (APF-D/6-311+G*) with a Franck-Condon-Herzberg Teller analysis.

The ground state and triplet excited state geometries of bipyridine and $\text{Cr(III)(NH}_3)_4(\text{bpy})$ are shown in Figure 3.4. Their respective bond distances are also included.

From the bond distances, it is clear that the bipyridine ligand distorts upon relaxation to the first excited state. The bond distance of the C-C bond linking the two pyridine rings together in the ground state is of single bond character at 1.493 Å, while that bond distance is compressed to double bond character at 1.399 Å. This same trend is present for $\text{Cr(III)(NH}_3)_4(\text{bpy})$, where the C-C bond linking the two pyridine rings shrinks from 1.466 Å to 1.381 Å upon relaxation to the first excited state.

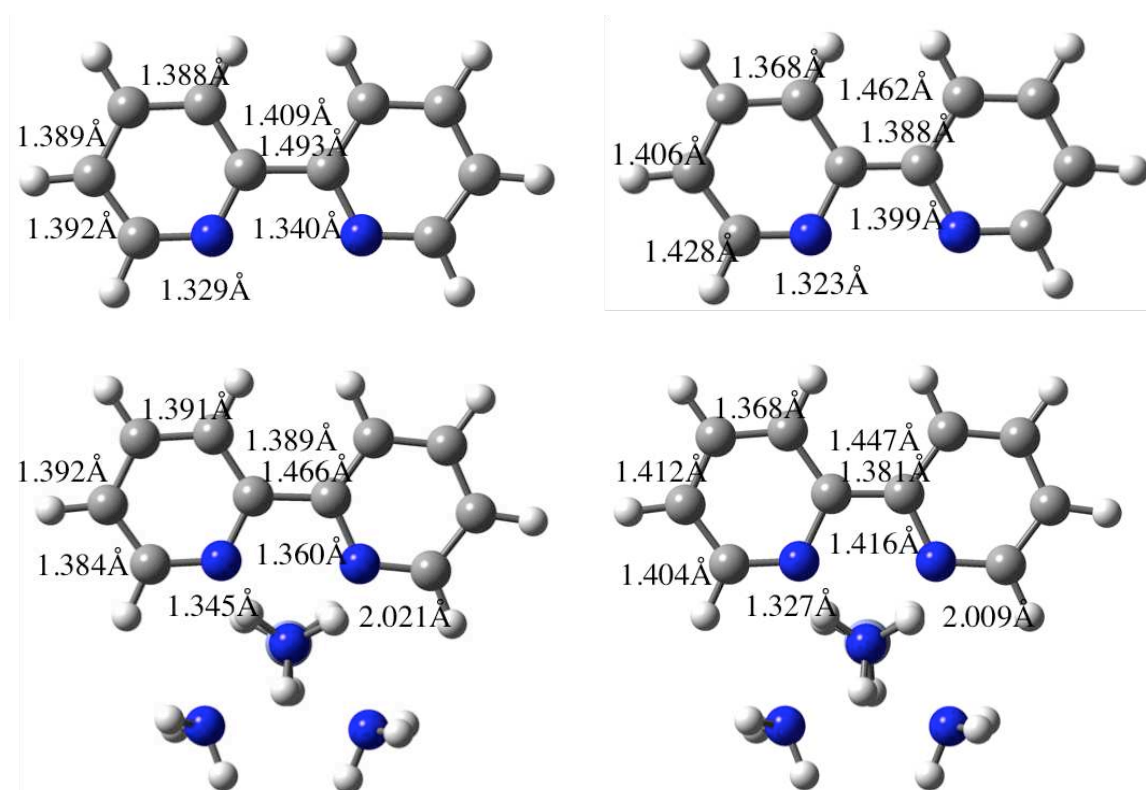


Figure 3.4: DFT(APF-D/6-311+G*) optimized geometries and bond distances of ground state (top left) and triplet excited state (top right) of bipyridine and ground (bottom left) and triplet excited state (bottom right) of $\text{Cr(III)(NH}_3)_4(\text{bpy})$.

In order to analyze the character of the distortions, the vibrational normal modes were projected onto the coordinates of the displacement between the ground and excited state. This data was plotted with the vibrational frequencies of all normal modes of the ground state by the intensity, in this case how much of each vibrational normal mode contributes to that distortion. The distortion plots are given in Figure 3.5.

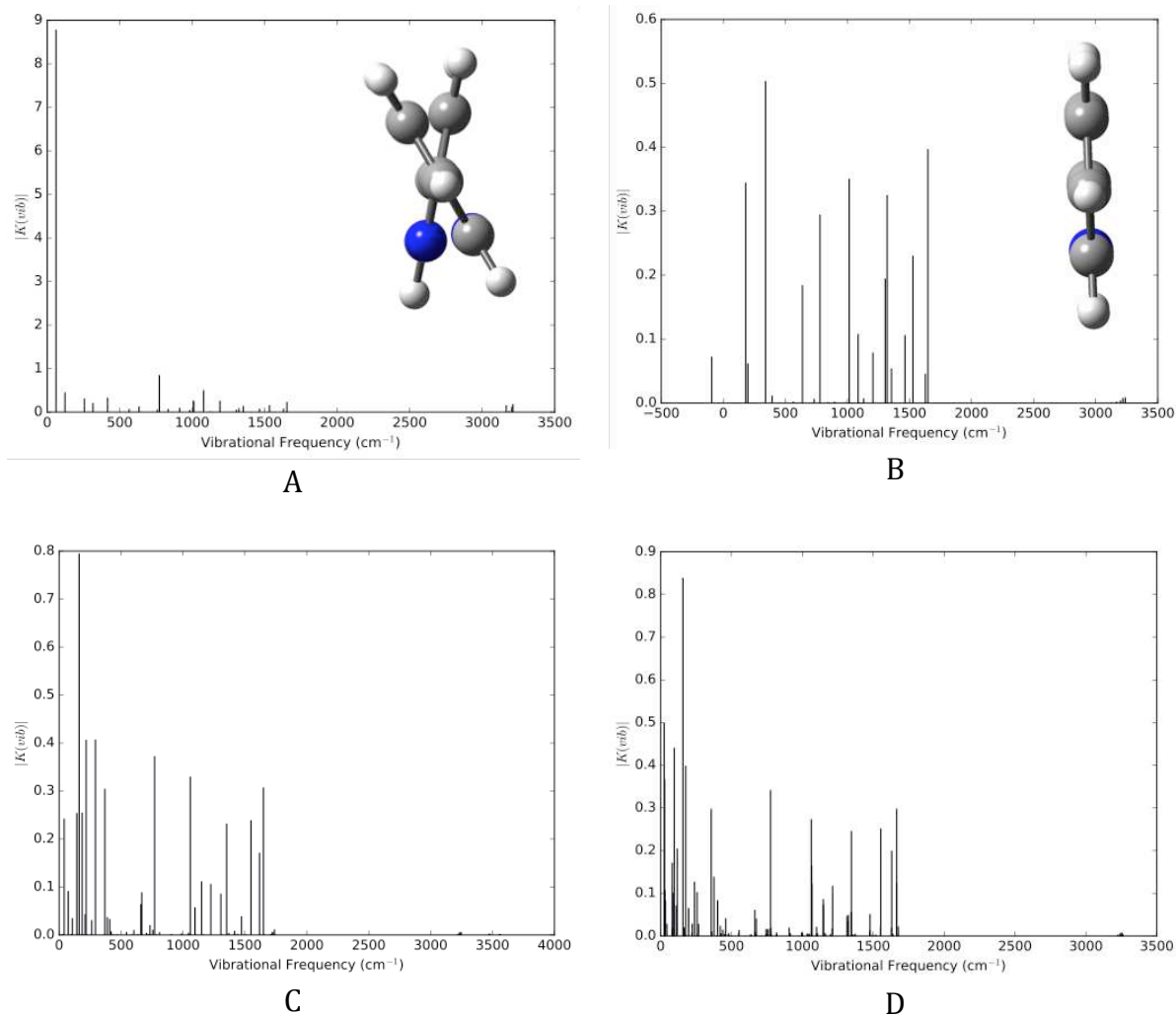


Figure 3.5: Vibrational projection plots of the geometric transition between the ground state and excited state geometries of distorted cis bipyridine (A), flat cis bipyridine (B), Cr(III)(NH₃)₄(bpy) (C), and Cr(III)(bpy)₃ (D). The y-axis units are in Å amu^{1/2}.

In Figure 3.5.A, the character of the distortion mode of cis bipyridine is dominated by the low energy torsional mode at around 80 cm⁻¹ due to the torsion of the pyridine

rings at the C-C bond. The distortion of the flat cis bipyridine molecule (Figure 3.5.B), mimicking the structure of the bipyridine as a ligand, is characterized by bending modes with a little stretching. There is a concentration of low energy modes with large amplitudes that can be populated easily. With respect to the Cr(III) complexes, Cr(III)(NH₃)₄(bpy) and Cr(III)(bpy)₃ (Figure 3.5.C and Figure 3.5.D), their vibrational contributions look eerily similar to the lone flat cis bipyridine contributions, with heavily populated bending and stretching modes concentrated around 1000-1500 cm⁻¹.

The geometry change upon excitation of the bipyridine ligands are characterized by many low energy modes with large amplitudes. Through these vibronic modes is how the intersystem crossing is occurring. As the ligand undergoes the vibrational relaxation to the first excited state, the complex can stretch into the triplet position, thereby using these stretches to change potential energy surfaces through the intersystem crossing. The geometry change is consistent with triplet bipyridine. This was also confirmed through an NTO analysis.

NTOs of the first excited state of bipyridine and Cr(III)(NH₃)₄(bpy) are in Figure 3.6. The left column describes where the electron came from and the right where the electron went to upon excitation. For the Cr(III)(NH₃)₄(bpy) case, the second row describes the α electron and the third row describes the β electron.

For the isolated bipyridine molecule, the first excited state is characterized by a predictable $\pi \rightarrow \pi^*$ transition, characteristic of triplet bipyridine. For the quartet Cr(III)(NH₃)₄(bpy) case, the α component of the transition can also be characterized by a $\pi \rightarrow \pi^*$ transition, with a little electron density on the Cr(III). In looking at the β transition, there is more character on the Cr(III) and the transition can be characterized

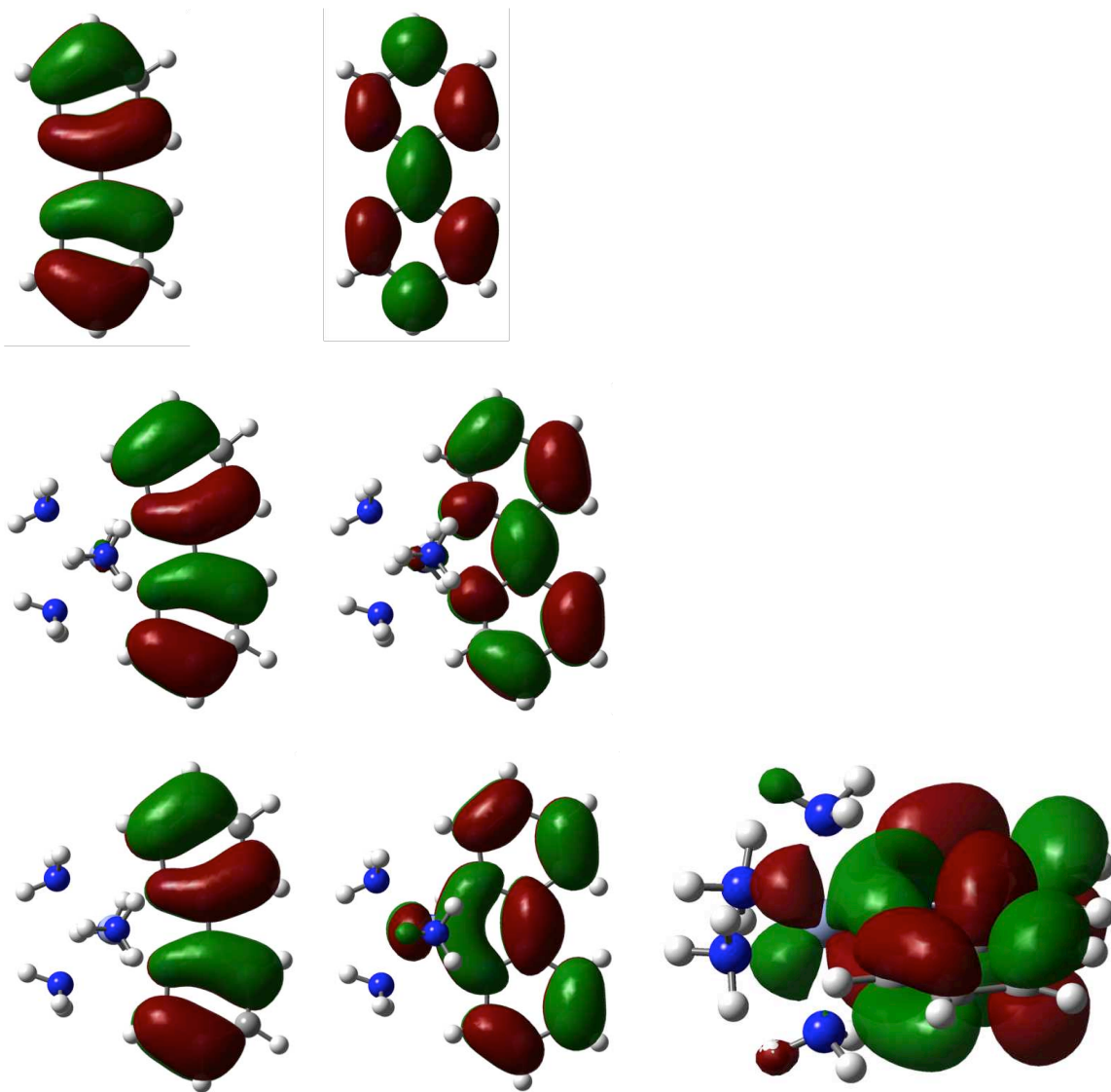


Figure 3.6: NTOs of the first excited states of bipyridine (first row), and $\text{Cr(III)(NH}_3)_4(\text{bpy})$ α electron (second row), and $\text{Cr(III)(NH}_3)_4(\text{bpy})$ β electron (third row) showing where the electron came from in the excitation (left) and where the electron went to (right). The third figure in the third row is a side view of the second figure in that row.

by a $d \rightarrow \pi^*$ transition. The d_{yz} character of the Cr(III) can be seen in the bottom right NTO of Figure 3.6.

In order to confirm this analysis, and provide a more precise description of the lowest TDDFT quartet excited state of Cr(III)(NH₃)₄(bpy), a spin state study was done with a CASSCF/NEVPT2 calculation. The modest basis set CASSCF/NEVPT2 used is not able to reproduce experimental excitation energies but does provide a description of the spin coupling in the five open shell quartet excited state. The CASSCF and NEVPT2 excitation energies for the seventh quartet are 3.842 eV and 3.49 eV respectively. The eighth doublet excitations are 3.447 eV and 3.408 eV using CASSCF and NEVPT2. Coefficients of the spin-determinants from the seventh quartet state (the five open shell quartet excited state) and the eighth doublet (the five open shell electron doublet excited state) are printed in Table 3.1 and Table 3.2. From the computed spin couplings these two states are two thirds of a doublet, quartet, sextet Heisenberg antiferromagnetic spin ladder. The corresponding sextet state is at 3.578 eV CASSCF, and 3.671 eV NEVPT2.

Table 3.1: Spin determinant components and coefficients that comprise the seventh quartet state. Each row represents a single spin-determinant with their corresponding coefficient.

π	t_{2g}	t_{2g}	t_{2g}	π^*	e_g	e_g	coefficient
β	α	α	α	α	0	0	-0.516963949
α	β	α	α	α	0	0	0.348638985
α	α	β	α	α	0	0	0.346837396
α	α	α	β	α	0	0	0.356099333
α	α	α	α	β	0	0	-0.534611765

Table 3.2: Spin-determinant components for the eight doublet state. Each row is representative of a single spin-determinant with their corresponding coefficient.

π	t_{2g}	t_{2g}	t_{2g}	π^*	e_g	e_g	coefficient
β	β	α	α	α	0	0	0.222742025
β	α	β	α	α	0	0	0.222069413
α	β	β	α	α	0	0	-0.218220048
β	α	α	β	α	0	0	0.216607890
α	β	α	β	α	0	0	-0.222355890
α	α	β	β	α	0	0	-0.220843389
β	α	α	α	β	0	0	-0.661419327
α	β	α	α	β	0	0	0.217833914
α	α	β	α	β	0	0	0.216994025
α	α	α	β	β	0	0	0.226591389

Traditionally, the lowest quartet for Cr(III) complexes is thought to either be a LF transition or a MLCT transition. Based on the coefficients of the determinants, it is evident that the spin eigenfunctions of this quartet state can be broken up into two key components, representing a combination of a triplet and quartet state. The two -0.5 coefficients are characterized by a β electron in the π and π^* orbitals. This ($\alpha\beta + \beta\alpha$) state for the π and π^* orbitals is indicative of a triplet bipyridine state, depicted in Figure 3.7.

For the spin determinants with coefficients around 0.35, each determinant contains a β electron present in the first, second, or third t_{2g} orbital. This yields an overall quartet eigenstate. The slightly lower doublet from the CASSCF/NEVPT2 has the quartet Cr(III) antiferromagnetically coupled to triplet bipyridine. The sextet and

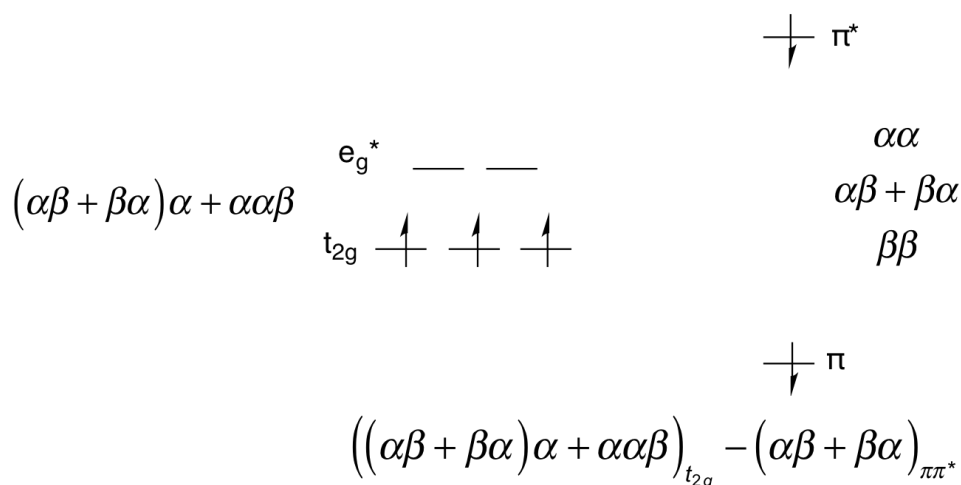


Figure 3.7: The electronic configuration of one of the excited doublet states of Cr(III)(NH₃)₄(bpy) where the ligand is in a triplet state and the metal center is in a quartet state; the ligand and the metal center are antiferromagnetically coupled making an overall doublet state.

doublet states are describable by DFT while the quartet requires multiple determinants, accessible in TD-DFT but not ground state DFT.

IV. CONCLUSIONS

The geometric distortion upon excitation, the character of the orbitals involved in excitation, and CAS spin character are all consistent with a ligand-based triplet excitation coupled with a quartet Cr(III) ground state. While it is commonly thought that the relaxation of the Cr(III) complex from the ⁴T_{2g} excited state to the ²E state, these calculations show that Cr(III) remains in its quartet ⁴T_{2g} state. The triplet bipyridine charge transfer state is actually what results in the fast intersystem crossing, coupling to the quartet Cr(III) state and keeping the system in between a doublet and sextet excited state. This suggests that the electron-electron exchange interactions involving the Cr d³ electron configuration is a source for novel reactivity. Therefore, tuning ligands to favor

this pathway, such as using a ligand with a lower energy triplet state, is a promising path forward for optimizing these systems for photocatalysis.

REFERENCES

- (1) Yoon, T. P.; Ischay, M. A.; Du, J. Visible Light Photocatalysis as a Greener Approach to Photochemical Synthesis. *Nat. Chem.* **2010**, *2* (7), 527–532.
- (2) Tucker, J. W.; Stephenson, C. R. J. Shining Light on Photoredox Catalysis: Theory and Synthetic Applications. *J. Org. Chem.* **2012**, *77* (4), 1617–1622.
- (3) Prier, C. K.; Rankic, D. A.; MacMillan, D. W. C. Visible Light Photoredox Catalysis with Transition Metal Complexes: Applications in Organic Synthesis. *Chem. Rev.* **2013**, *113* (7), 5322–5363.
- (4) Gong, J.; Sumathy, K.; Qiao, Q.; Zhou, Z. Review on Dye-Sensitized Solar Cells (DSSCs): Advanced Techniques and Research Trends. *Renew. Sustain. Energy Rev.* **2017**, *68*, 234–246.
- (5) Juban, E. A.; McCusker, J. K. Ultrafast Dynamics of 2E State Formation in Cr(Acac)₃. *J. Am. Chem. Soc.* **2005**, *127* (18), 6857–6865.
- (6) König, E.; Herzog, S. Electronic Spectra of Tris (2, 2'-Bipyridyl) Complexes—I: The Chromium Series [Cr (Bipy) ₃]_z, Z=+ 3,+ 2,+ 1, 0. *J. Inorg. Nucl. Chem.* **1970**, *32* (2), 585–599.
- (7) Jens Josephsen; Claus Erik Schäffer. The Position of 2,2'-Bipyridine and 1,10-Phenanthroline in the Spectrochemical Series. *Acta Chem. Scand.* **1977**, *31A*, 813–824.
- (8) Frisch, M. J.; Trucks, G. W.; Schlegel, H. B.; Scuseria, G. E.; Robb, M. A.; Cheeseman, J. R.; Scalmani, G.; Barone, V.; Petersson, G. A.; Nakatsuji, H.; et al. *Gaussian 16 Revision A.03*.

- (9) Austin, A.; Petersson, G. A.; Frisch, M. J.; Dobek, F. J.; Scalmani, G.; Throssell, K. A Density Functional with Spherical Atom Dispersion Terms. *J. Chem. Theory Comput.* **2012**, *8* (12), 4989–5007.
- (10) Chai, J.-D.; Head-Gordon, M. Long-Range Corrected Hybrid Density Functionals with Damped Atom–atom Dispersion Corrections. *R. Soc. Chem.* **2008**, *10*, 6615–6620.
- (11) Santoro, F.; Lami, A.; Improta, R.; Bloino, J.; Barone, V. Effective Method for the Computation of Optical Spectra of Large Molecules at Finite Temperature Including the Duschinsky and Herzberg–Teller Effect: The Qx Band of Porphyrin as a Case Study. *J. Chem. Phys.* **2008**, *128* (22), 224311.
- (12) Martin, R. L. Natural Transition Orbitals. *J. Chem. Phys.* **2003**, *118* (11), 4775–4777.
- (13) Neese, F. The ORCA Program System. *Wiley Interdiscip. Rev. Comput. Mol. Sci.* **2012**, *2* (1), 73–78.

I. INTRODUCTION

Acid-base reactions play an essential role in both biological and industrial chemical reactions. The reaction pathways of a system are often dictated by the pH of the environment. The protonation state of an atom can mediate a given reaction and promote certain pathways. Small protonation/deprotonation changes to a molecule or complex can dramatically impact the structural stability and lead to conformational changes of a system.¹ Therefore, there is potential to tailor a complex to a given reaction pathway by understanding and exploiting the protonation state of the system.

Photocatalysis is an area in chemistry that could benefit from the understanding of protonation impact of a system, where protonation/deprotonation of a catalyst could tune the system to promote a certain reaction. Danforth and Kohler showed the reduction of a hexaaqua(III) complex in aqueous solution occurs by deprotonation of a water ligand without a net change in the oxidation state of the iron via photon-initiated hydrolysis.² The potential for light to change the pH and therefore the behavior of a catalytic system could yield new reaction pathways for photocatalysts. In addition, the protection of a complex's oxidation state in the process could be important for protecting long lived excited states of certain oxidation states while allowing for new chemical reactions via protonation/deprotonation.

¹ The work in this chapter was done by Collette M. Nite and David J. Boston. Collette M. Nite performed all theoretical calculations and analysis. David J. Boston is responsible for all experimental work, including the synthesis, and absorption spectra, and crystallography of the transition metal complexes. The text was written entirely by Collette M. Nite.

CH₃OH, citing the involvement of the second coordination sphere.⁵ Han et al. determined that the –NH moiety could be significant in reducing carbonate species.⁶ Interaction of the nitrogen atom with the ligand backbone could potentially control the π donation by the presence of the –NH moiety.⁷ Therefore the position of the –NH moiety with respect to the metal center is important for the involvement of the –NH moiety in improving catalytic activity and selectivity as well as recognition and activation of substrates.

One of the most interesting features about this –NH moiety of the THB ligand is that the N atom can be in different protonation states depending on reaction conditions. This proton source can play a significant role in the tuning of this complex for a given reaction, which is compounded by the presence of two acidic –NH moieties in the THB ligand.

While experimental characterization of these transition metal complexes in a given pH environment is challenging, theoretical methods can aid this process. Density functional theory (DFT) and its time dependent method (TDDFT) for calculating and characterizing excited states has improved in terms of accuracy and efficiency and can be used for calculating large transition metal complexes with a high level of accuracy.^{8,9}

Our group investigated the impact of the protonation states on the photochemistry of the THB complex using TDDFT, confirmed with experimental results. The results of this study show the potential for tuning this and other complexes for desirable photo properties for reaction schemes.

II. EXPERIMENTAL

Spin-unrestricted hybrid self-consistent field (SCF) density functional theory (DFT) and time-dependent DFT (TD-DFT) calculations were carried out using the Gaussian09 suite of electronic structure codes.¹⁰ Complexes were optimized using hybrid functional, APF-D, in order to account for intramolecular dispersion forces, as well as a more diffuse basis set, 6-311+G*, in attempt to better describe long range charge transfer character. A PCM solvent model was used with dimethylformamide (DMF) solvent to mimic experimental procedures. The first 48 excited states of the complexes were calculated using TDDFT. From the oscillator strengths and peak positions calculated in TDDFT calculation, the theoretical absorption spectra were generated. Each electronic state was convoluted with a Gaussian line shape with a 0.219 eV line width. From the DFT energy calculations, the spin density plots for the complexes were plotted. BF₄ molecules were added such that each system had a net zero charge.

III. RESULTS/DISCUSSION

The theoretical absorption spectra of Cr(III)THB and Cr(II)THB are in Figure 4.2 and Figure 4.3, respectively. The spectrum in red represents the THB ligand, complex (1), where both secondary amines are protonated. The green spectrum represents complex (2) where one amine is deprotonated and the blue spectrum represents complex (3) where both amines are deprotonated.

One interesting feature when comparing the Cr(III) species is that for the doubly protonated complex (in red) there are no spectral features after around 400 nm, an important quality for a photocatalyst that is lacking in this case. However, for the mono-

protonated (in green) and deprotonated cases (in blue), there are long wavelength features out past 600 nm. Therefore it is evident that tuning the pH environment of this photocomplex can have important implications for its performance as a photocatalyst.

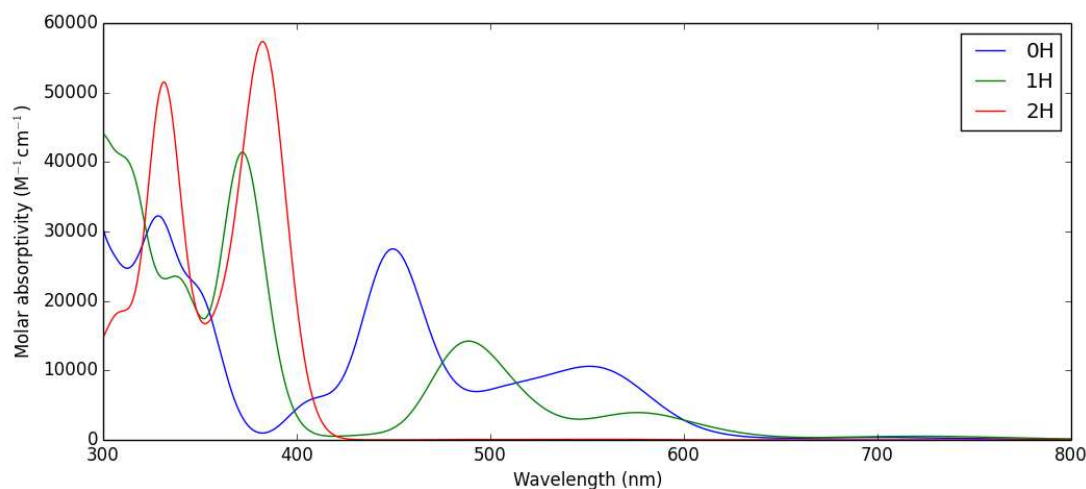


Figure 4.2: TDDFT(APF-D/6-311+G*) absorption spectra of Cr(III)(THB) with implicit DMF solvent in various protonation states; complex (1) (red), complex (2) (green), and complex (3) (blue).

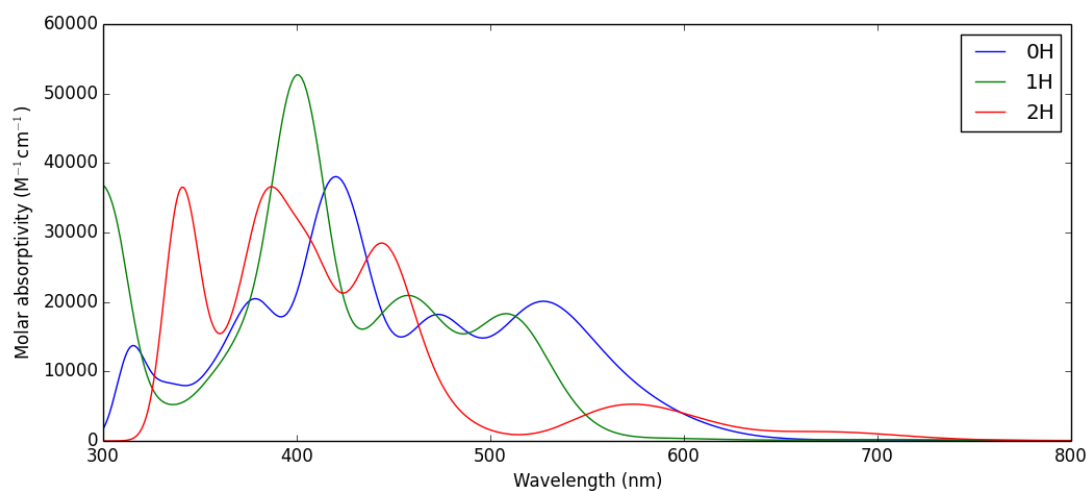


Figure 4.3: TDDFT(APF-D/6-311+G*) absorption spectra of Cr(II)(THB) with implicit DMF solvent in various protonation states; complex (4) (red), complex (5) (green), and complex (6) (blue).

In looking at Figure 4.3, Cr(II)THB complexes all span well into the visible region, including the case with the doubly protonated THB ligand (red). The spectra of

Cr(II)THB complexes as a whole differ from the spectra of Cr(III)THB complexes. It is evident that the oxidation state of these complexes can also be tuned to promote certain photochemical properties that would be useful for a given photocatalytic transformation. Therefore, the oxidation state as well as the protonation state of these complexes should be well characterized and understood in order to tune these complexes for the desired photochemistry. However, this is a difficult process that involves both theoretical and experimental collaboration, as these transition metal complexes are notoriously complex.

The theoretical spectra of the mono-protonated THB complex with Cr oxidation states II, III, and IV (green, blue, and orange, respectively) are given in Figure 4.4. All three complexes share a similar spectral peak around 570 nm. However, Cr(III)THB also has a distinct peak around 500 nm. Comparable experimental spectra of the complexes are in Figure 4.5. Only Cr(III) and Cr(IV) THB complexes are featured. The material thought to be Cr(II) gives the same spectra as Cr(III) and it therefore suggests that a true Cr(II)THB complex had not been synthesized.

Spin density plots of Cr(II), Cr(III), and Cr(IV) complexes were generated and are shown in Figure 4.6 to elucidate the differences between the Cr(II) and Cr(III) complexes. From the spin density plots, it is evident that the Cr in the Cr(II) complex actually behaves as Cr(III) with d^3 electronic configuration on the metal and the β electronic character out on the ligand. The Cr(IV) spin density plot shows d^2 configuration on the metal. From the spin density plots it was shown that the Cr(II) complex is not really a true Cr(II) complex but rather a Cr(III) complex with opposite spin character pushed out onto the ligand.

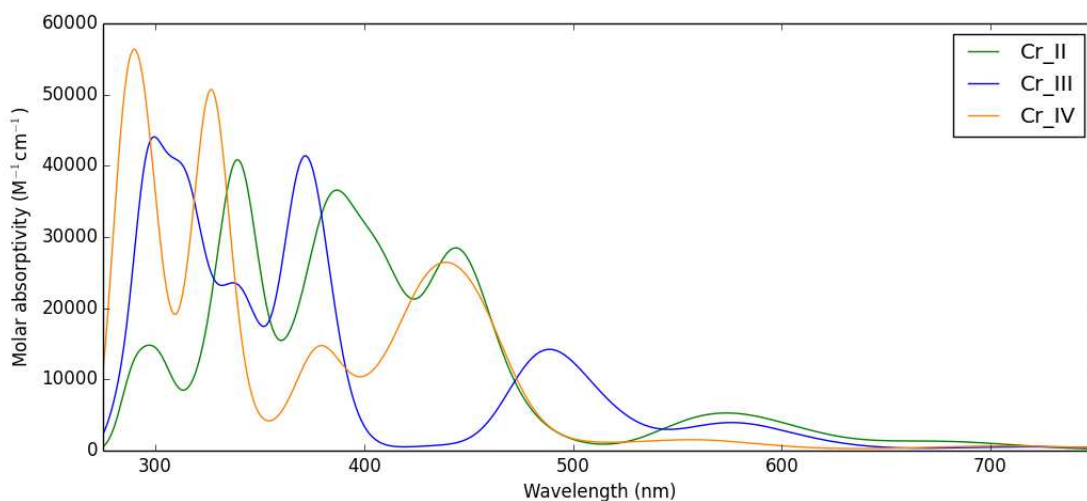


Figure 4.4: TDDFT(APF-D/6-311+G*) absorption spectra of chromium THB complex with implicit DMF solvent in various oxidation states; Cr(II) complex (**6**) in green, Cr(III) complex (**2**) blue and Cr(IV) complex (**7**) in orange.

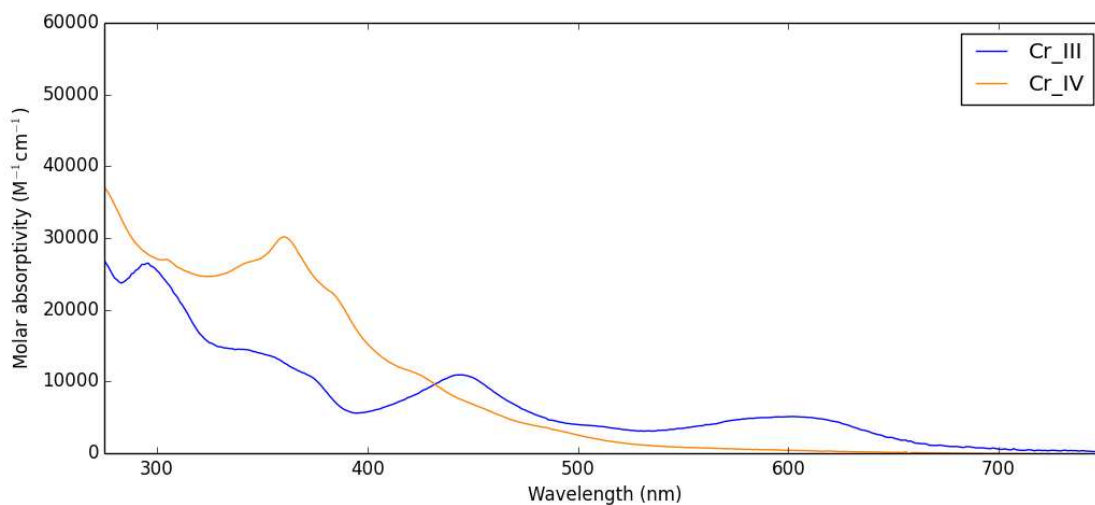
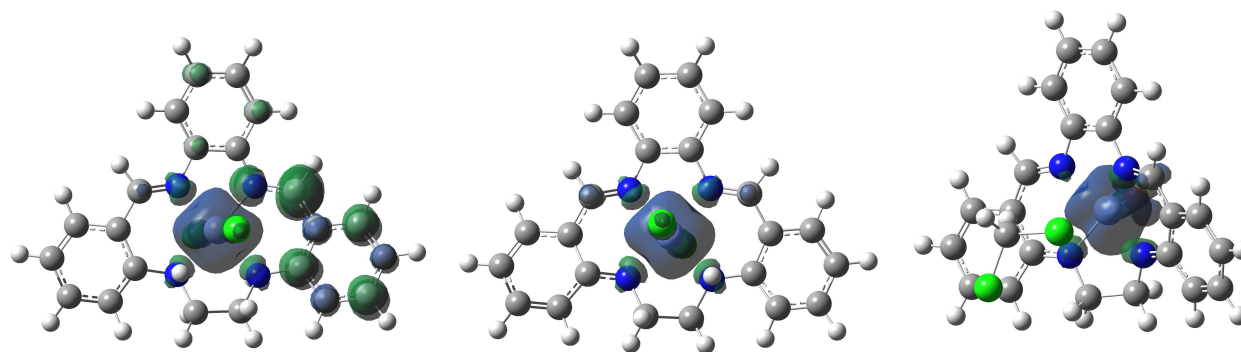


Figure 4.5: Experimental UV-vis spectra of Cr(III) (blue) and Cr(IV) (orange) THB complexes in DMF solvent.



Cr(II)

Cr(III)

Cr(IV)

Figure 4.6: Spin density plots of Cr(II), complex **(2)** (left), Cr(III), complex **(6)** (center), and Cr(IV), complex **(7)** (right) THB complexes showing where the unpaired spin is located. The α spin is shown in blue, and the β spin is shown in green.

The theoretical spectrum of the Cr(III)THB species is overlaid with the experimental spectrum of the complex in Figure 4.7. While the peak positions do not correspond quantitatively due to approximations to experimental factors such as solvent in addition to TDDFT underestimating the energies, there is fair qualitative agreement between the spectra. Omitting the red shift of the theoretical spectrum, the peak shapes and order match.

This qualitative agreement seemed to validate our theoretical method for characterizing these difficult systems. It is concluded that the experimental chromium THB complex in DMF solvent is a Cr(III) metal center complexed to the THB ligand where one secondary amine nitrogen bound to the metal is deprotonated.

An experimental crystal structure for the complex has been obtained, confirming these conclusions, as shown in Figure 4.8.

IV. CONCLUSIONS

Through this study on the chromium THB complex, it has been shown that protonation state of a given complex can drastically affect the photochemical properties

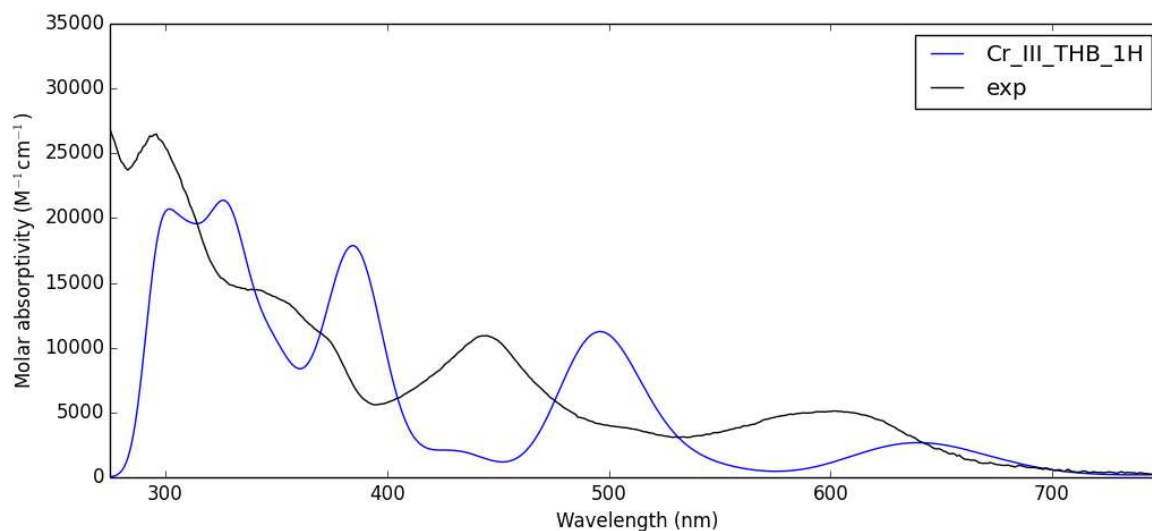


Figure 4.7: The theoretical TDDFT spectrum (blue) and the experimental spectrum (black) of the Cr(III)THB complex (**2**) in DMF.

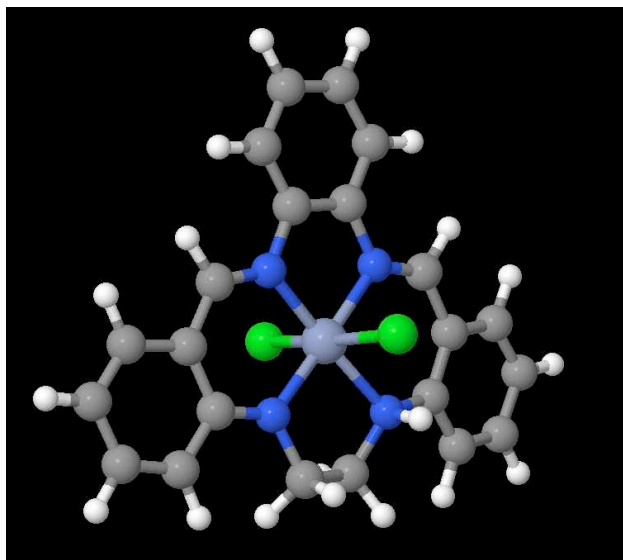


Figure 4.8: The experimental crystal structure of the Cr(III) THB complex, showing one deprotonated secondary amine.

of a complex. By controlling the pH environment, the complex can be modified to mediate a given photocatalytic process. Similarly, the oxidation state of the complex has also been shown to impact the photochemistry as well. This selective tuning of these complicated systems is a complex process that requires intricate methods for

characterization. Theoretical DFT/TDDFT methods have proven to be an integral part of characterizing this Cr(III) monoprotonated THB complex. This procedure has validated our TDDFT method for characterizing these systems towards selective photocatalytic tuning and will continue to push forward efforts for an inner sphere photocatalyst.

REFERENCES

- (1) Huang, Y. M.; You, W.; Caulkins, B. G.; Dunn, M. F.; Mueller, L. J.; Chang, C. A. Protonation States and Catalysis: Molecular Dynamics Studies of Intermediates in Tryptophan Synthase. *J. Mol. Recognit. JMR* **2014**, *27* (9), 537–548.
- (2) Danforth, R. A.; Kohler, B. Ultrafast Photochemical Dynamics of the Hexaaquairon(III) Ion. *Chem. Phys. Lett.* **2017**, *683* (Supplement C), 315–321.
- (3) Stevenson, S. M.; Shores, M. P.; Ferreira, E. M. Photooxidizing Chromium Catalysts for Promoting Radical Cation Cycloadditions. *Angew. Chem. Int. Ed.* **2015**, *54* (22), 6506–6510.
- (4) Zhao, B.; Han, Z.; Ding, K. The N⁺H Functional Group in Organometallic Catalysis. *Angew. Chem. Int. Ed.* **2013**, *52* (18), 4744–4788.
- (5) Kothandaraman, J.; Goepfert, A.; Czaun, M.; Olah, G. A.; Prakash, G. K. S. Conversion of CO₂ from Air into Methanol Using a Polyamine and a Homogeneous Ruthenium Catalyst. *J. Am. Chem. Soc.* **2016**, *138* (3), 778–781.
- (6) Han, Z.; Rong, L.; Wu, J.; Zhang, L.; Wang, Z.; Ding, K. Catalytic Hydrogenation of Cyclic Carbonates: A Practical Approach from CO₂ and Epoxides to Methanol and Diols. *Angew. Chem. Int. Ed.* **2012**, *51* (52), 13041–13045.
- (7) Käß, M.; Friedrich, A.; Drees, M.; Schneider, S. Ruthenium Complexes with Cooperative PNP Ligands: Bifunctional Catalysts for the Dehydrogenation of Ammonia–Borane. *Angew. Chem. Int. Ed.* **2009**, *48* (5), 905–907.
- (8) Casida, M. E.; Huix-Rotllant, M. Progress in Time-Dependent Density-Functional Theory. *Annu. Rev. Phys. Chem.* **2012**, *63* (1), 287–323.

- (9) Cramer, C. J.; Truhlar, D. G. Density Functional Theory for Transition Metals and Transition Metal Chemistry. *Phys. Chem. Chem. Phys.* **2009**, *11* (46), 10757–10816.
- (10) Frisch, M. J.; Trucks, G. W.; Schlegel, H. B.; Scuseria, G. E.; Robb, M. A.; Cheeseman, J. R.; Scalmani, G.; Barone, V.; Mennucci, B.; Petersson, G. A.; et al. *Gaussian 09 Revision D.01*.

CHAPTER 5: COMPARISON OF EXCITED STATE PROPERTIES OF CHROMIUM(III) AND VANADIUM(II) COMPLEXES: POTENTIAL AS PHOTOCATALYSTS¹

I. INTRODUCTION:

Across all chemical industries there is a push for more environmentally friendly and sustainable processes. Photocatalysis has become an attractive prospect for chemical transformations that conventionally rely on harsh reaction conditions and stoichiometric reagents generating waste. Many research groups have shown that photocatalysts can be used to mediate traditional synthetic reactions. Yoon et al. showed that visible light could actually be used as a reagent with a $\text{Ru}(\text{bpy})_3^{2+}$ photocatalyst for [2+2] cycloadditions.¹ However, this reaction as well as other successful phototransformations have relied on the use of metal catalysts made up of ruthenium and other rare metals such as rhenium and iridium which are not sustainable or economically viable in large scale application.²

There is a need for a more earth abundant alternative to these rare metals. First row transition metals are several orders of magnitude more abundant than rare metals. There is potential for first row transition metal photocatalysts. Stevenson et al. showed that a chromium(III) complex was capable of photooxidizing catalyzed Diels-Alder cycloadditions. It is theorized that rare metal complexes can be substituted by earth

¹ The work in this chapter was done by Collette M. Nite and Jacob M. Nite. Collette M. Nite calculated the optimized structures for all complexes including the vanadium and chromium complexes with the PDO, pyridine, and multidentate ligands. She also calculated all TDDFT excited states and absorption spectra. Jacob M. Nite calculated the vibrational distortion plots, including the structure alignments. He also performed all calculations involving the SORCI plots. Both authors contributed equally to the text of the chapter.

abundant first row transition metal complexes for phototransformations on a much broader scale. However, pursuit of this goal requires in depth theoretical and experimental research, as first row transition metal complexes behave differently than second and third row transition metal complexes.

First row transition metal complexes are much more labile than second and third row metals, yielding much more reactive and less stable catalysts. In addition, first row metals are electron spin active, resulting in wildly different chemistry with complicated excited state manifolds and thus difficult characterizations. There is much more interplay between first row transition metals and their ligands, requiring a higher degree of care in their complex design than second and third row counterparts.

The choice of ligand is therefore very important when designing these catalysts. Ligands are often noninnocent and can have a drastic effect on the photoabsorption of a complex. Ligands often dictate the spin state of a metal in a given complex, determining if the complex will be high- or low-spin. Substitution of a different metal in the same ligand can yield very different results, because metals interact differently with ligands. The differences between metal-swapped complexes can be more abrupt than changes to the ligands due to the limited metal center candidates combined with the substantial difference in properties of the metal centers. Compared to an enormous range of ligand design choices, the handful of metals in the first-row dictate that careful selection of the proper metal is crucial.

In this paper we focus on vanadium and its potential for photocatalysis. V(II) is of d^3 electronic configuration, just as Cr(III). While Cr(III) has beneficial properties such as long excited state lifetimes and demonstrable photocatalytic ability, it is not the most

desirable metal for environmental concerns. V(II) is not readily oxidizable into carcinogenic species. Comparing the photophysical and photochemical between V(II) and Cr(III) may lead to insight on how the properties of the ligand dictate the total complex properties when electronic configuration is held constant. In this paper we use theoretical methods in order to compare Cr(III) and V(II) complexes on the basis of their photophysical and photochemical properties in order to elucidate their differences and vanadium's potential as a photocatalyst.

II. THEORETICAL METHODS:

The complexes studied were comprised of the V(II), Cr(III), Mn(II), Fe(III), Co(III), and Zn(II) metal centers paired with several ligands: a Schiff base tripodal ligand with a bridgehead nitrogen, a salen derivative, bipyridine, and 1,3-propanedionato(PDO).

A. STRUCTURE OPTIMIZATION AND THEORETICAL SPECTRA:

The structures of each complex were optimized using DFT with the APF-D functional and the 6-311+G* basis set. The time-dependent density functional theory (TDDFT) excited states were calculated for the first 24 excited states of each complex to insure all relevant excited states were included. Convoluting each TDDFT transition with a Gaussian line shape with a linewidth of 0.093 eV at the full-width half-maximum, theoretical absorption spectra were plotted. The linewidth was chosen to approximate average excited state linewidths. The lowest excited doublet state was obtained by broken-symmetry DFT. The spin density plots were calculated using Gausview using a course grain cube and an isovalue of 0.003 to insure optimal visualization of the differences between the chromium and vanadium complexes. All DFT calculations were computed using the Gaussian 09d software suite.³

B. Cr / V(PDO)₃:

Additionally, the complexes with the ligand 1,3-propanedionato (PDO) were studied to gain an insight into the excited state behavior of Cr(III) and V(II). The electronic states are references to an O_h point group to remain consistent with the literature.⁴ The ⁴A_{2g} ground states of Cr(III)PDO₃ and V(II)PDO₃ were optimized using the same DFT approaches used above. The lowest excited state structures of the Cr(III) and V(II) complexes were calculated corresponding to the Jahn-Teller distorted ⁴T_{2g} state constrained to the C₂ symmetry point group. These structures are analogous to the Cr(III)(AcAc)₃ ⁴T_{2g} cited previously in literature.⁴ We aligned the ground state and excited state structures to form a linear pathway in the form of Miller et al. and formed linearly interpolated structures along path.⁵

The excited states of each structure along the distortion coordinate were calculated using the spectroscopy oriented configuration interaction (SORCI) method to construct the excited state pathways between the ground state and relaxed excited state. The initial wave function for each structure was calculated using the B3LYP functional with a cc-(p)VDZ basis set for all atoms except the metal center which used a cc-pCVTZ basis set. Each wave function was refined using a complete active space self-consistent field wave function (CASSCF) with a 3,5 active space and state averaging. All SORCI calculations utilizing the CASSCF wave functions were done including additional core electrons beyond the CASSCF active space. The B3LYP DFT, CASSCF, and SORCI calculations were computed using the ORCA 3.0.3 electronic structure suite.⁶

C. VIBRATIONAL PROJECTIONS:

The vibrational contributions to the difference between the ground state and excited states of Cr(III)bpy₃ and V(II)bpy₃ were calculated using a vibrational mode projection scheme used by Ando et al.⁴ Briefly, the vibrational normal modes of both Cr(III)bpy₃ and V(II)bpy₃ were calculated for the ground state geometry. The excited state structure was aligned to the ground state structure using the same criteria used for the linear reaction pathway in the SORCI calculations where any translational and angular momentum were removed from the structure. The excited state center of mass was translated to the center of mass of the ground state and the excited state structure was rotated by the Euler indices that satisfy the equation

$$\sum_i m_i (\vec{R}_i^r \times \vec{R}_i^p) = 0 \quad (0.1)$$

where i is over all atoms, m_i is the mass of atom i , and \vec{R}_i is the Cartesian coordinates of atom i .⁵ The resulting structures were examined to ensure that the alignment did not contain any unphysical atom movements between the structures. This ensures that no vibrational modes are projected onto differential distortions due to translations or rotations of the whole complex.

The frequency calculation of the ground state includes the eigenvalues and eigenvectors of the diagonalized Hessian, which describe the vibrational energies and mode motion in terms of atom displacements, \mathbf{L}_{gs} . A Duschinsky vector, \mathbf{K}_{gs} , is calculated using the formula

$$\mathbf{K}_{gs} = \mathbf{M} \mathbf{L}_{gs} \mathbf{R}_d \quad (0.2)$$

where \mathbf{M} is a matrix containing the masses of each atom and, \mathbf{R}_d is the difference vector of atomic coordinates between the ground and excited states.⁴ This results in a

vector, \mathbf{K}_{gs} , that describes a relative amount of each vibrational mode resulting from the distortion between the ground and excited states.

III. RESULTS & DISCUSSION:

A. TDDFT:

When first analyzing potential ligand frameworks for photocatalysis, the focus was first on Schiff base moieties, a class of ligands containing a nitrogen-carbon double bond with the nitrogen bonded to an alkyl or aryl group. These ligands were known for straightforward syntheses with the ability to stabilize many different metals. The structure of the Schiff base moiety and the theoretical absorption spectra of the Schiff base ligand complexed various first row transition metals are shown in Figure 5.1. What was particularly intriguing when comparing the spectra of varying metals was the unique spectral feature of the V(II) complex (in purple) at around 630 nm. No other metal exhibited a broad intense peak at the low energy visible region.

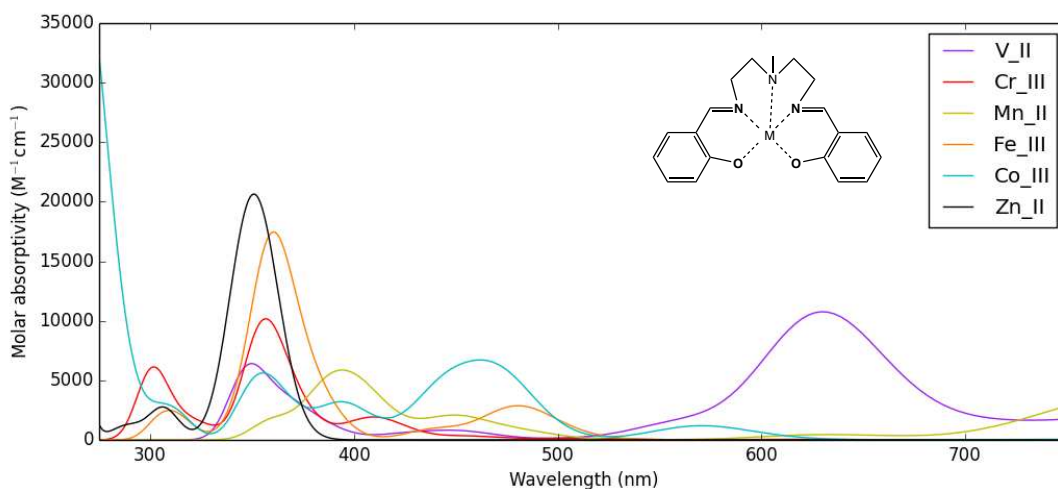


Figure 5.1: TDDFT(APF-D/6-311+G*) spectra of various first row transition metal Schiff base complexes.

Spectra of complexes of the salen Schiff base-derived ligand were also computed and analyzed for photochemical properties. The salen ligand is known for its

two imine nitrogens and two oxygen atoms complexed to the metal center. In Figure 5.2, a structural derivative was analyzed with amido groups substituted for the oxygen atoms. The theoretical spectra of the given complex with different first row metals are in Figure 5.2.

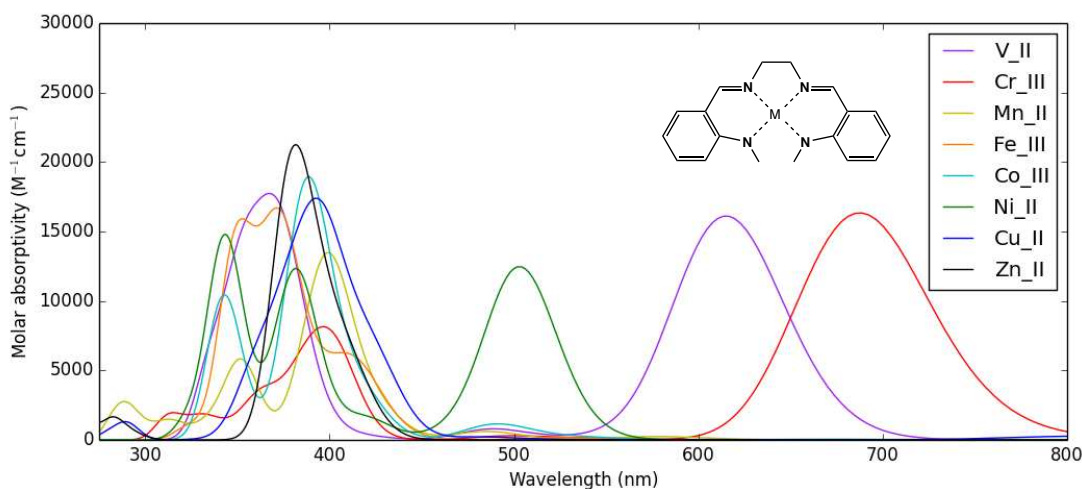


Figure 5.2: TDDFT(APF-D/6-311+G*) spectra of various first row transition metal salen type complexes.

Again, the V(II) salen derivative complex (in purple) had intense absorption in the low energy visible region marked by a broad peak centered around 610 nm. Notable also is the almost identical broad structural feature of the Cr(III) salen complex (in red), which is red shifted from the V(II) complex centered at around 690 nm. This spectrum led to the promising hypothesis that a d^3 V(II) metal complex could have similar photochemical properties as a d^3 Cr(III) metal complex, and therefore vanadium could be exploited as an alternative photocatalyst.

B. SPIN DENSITY PLOTS:

Electronic structure calculations were then used to explore potential differences between Cr(III) and V(II) complexes. Spin density shows where the unpaired spin electron is with respect to the metal and ligand of the complex. Spin density plots for a

few Cr(III) and V(II) complexes for their ground quartet states (left column) and their excited doublet states (right column) are shown in Table 5.1, Table 5.2, and Table 5.3.

Looking at the Cr(III)trisbipyridine case, the quartet state is immediately evident as the three unpaired alpha spin electrons are represented by the blue (alpha spin) cubic structure centered on the Cr(III) metal. In the doublet case, there is nodal beta spin character (represented in green) now on the metal where there is now one unpaired spin. Similar behavior can be described for the V(II) d^3 metal, where the spin density on the metal looks very similar to the Cr(III) case. However, a notable difference is the presence of spin density out on the bipyridine ligands in both the quartet and the doublet cases for vanadium. The importance of this density on the V(II) complex is related to the decreased quartet-doublet energy difference for the V(II) complex compared to the Cr(III) complex (1.08 eV versus 1.62 eV). The beta electron density on the ligand and energy differences suggests that the doublet state is more stable for the V(II) complex compared to the Cr(III) analog, decreasing the available chemical potential to catalyze reactions.

Another common photocomplex structure, the podand ligand complex, was compared. For the Cr(III) case there was again similar quartet and doublet behavior on the metal, with most spin density centered around the metal. In the V(II)pod complex doublet case, a large portion of the unpaired spin is again pushed out far onto the ligand structure.

Ester groups were added to the pod ligand structure in order to try inhibit the ligand from containing significant amounts of unpaired spin density. The trend still held

Table 5.1: Spin density plots of quartet and doublet states of the Cr(III)bpy₃ and V(II)bpy₃ photocomplexes.

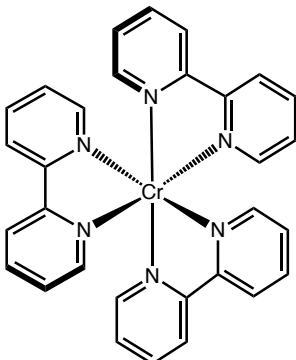
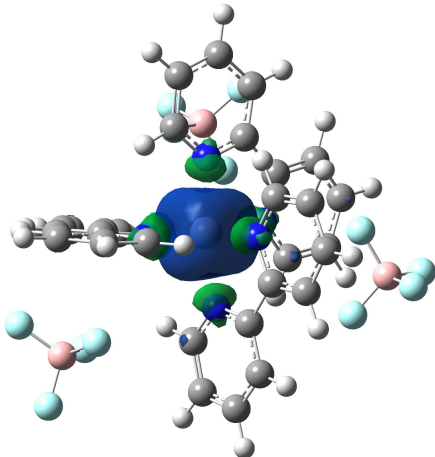
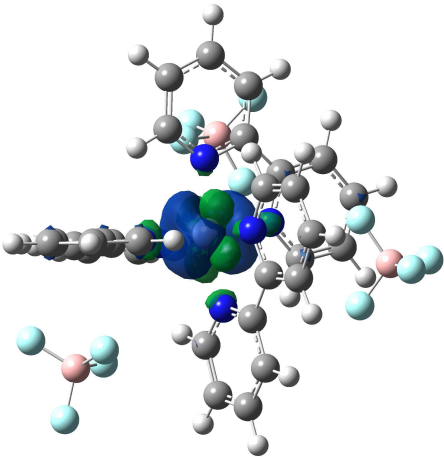
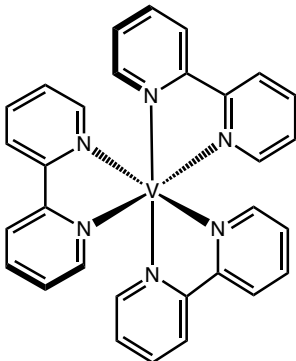
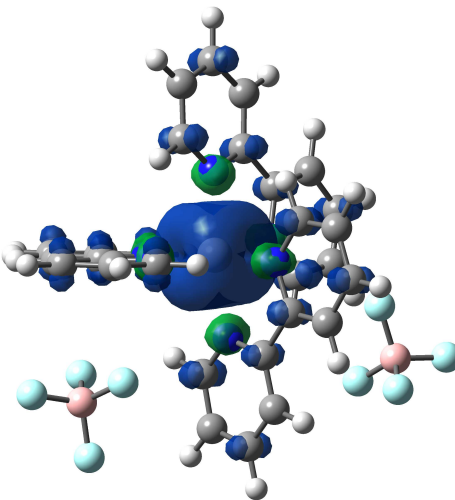
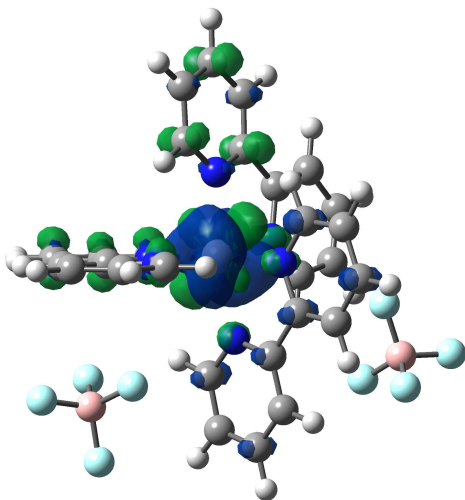
	Quartet	Doublet
<p>Cr(III)bpy₃</p>  <p>The chemical structure shows a central Chromium (Cr) atom coordinated to three bipyridine (bpy) ligands in an octahedral geometry. Each bipyridine ligand consists of two pyridine rings connected at the 2 and 6 positions. The Cr atom is coordinated to the nitrogen atoms of the three bipyridine ligands.</p>	 <p>Spin density plot of the Cr(III)bpy₃ complex in the Quartet state. The central Cr atom is shown with a large blue spin density lobe. The bipyridine ligands are shown with smaller spin density lobes, indicating delocalization of the unpaired electron density.</p>	 <p>Spin density plot of the Cr(III)bpy₃ complex in the Doublet state. The central Cr atom is shown with a large blue spin density lobe. The bipyridine ligands are shown with smaller spin density lobes, indicating delocalization of the unpaired electron density.</p>
<p>V(II)bpy₃</p>  <p>The chemical structure shows a central Vanadium (V) atom coordinated to three bipyridine (bpy) ligands in an octahedral geometry. Each bipyridine ligand consists of two pyridine rings connected at the 2 and 6 positions. The V atom is coordinated to the nitrogen atoms of the three bipyridine ligands.</p>	 <p>Spin density plot of the V(II)bpy₃ complex in the Quartet state. The central V atom is shown with a large blue spin density lobe. The bipyridine ligands are shown with smaller spin density lobes, indicating delocalization of the unpaired electron density.</p>	 <p>Spin density plot of the V(II)bpy₃ complex in the Doublet state. The central V atom is shown with a large blue spin density lobe. The bipyridine ligands are shown with smaller spin density lobes, indicating delocalization of the unpaired electron density.</p>

Table 5.2: Spin density plots of quartet and doublet states of the Cr(III)pod and V(II)pod photocomplexes.

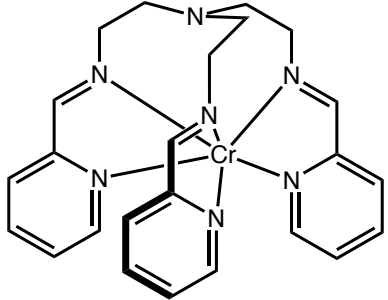
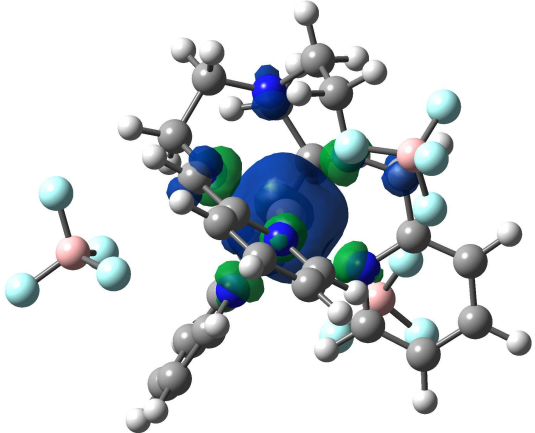
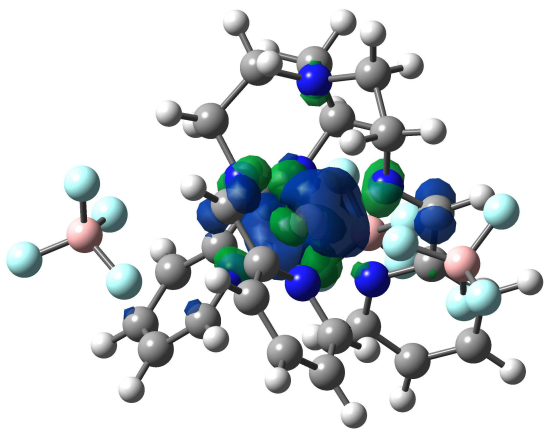
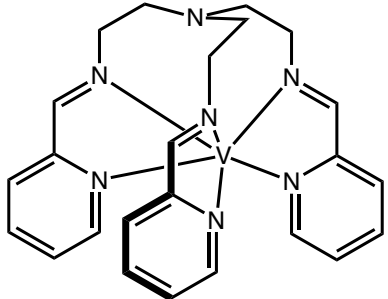
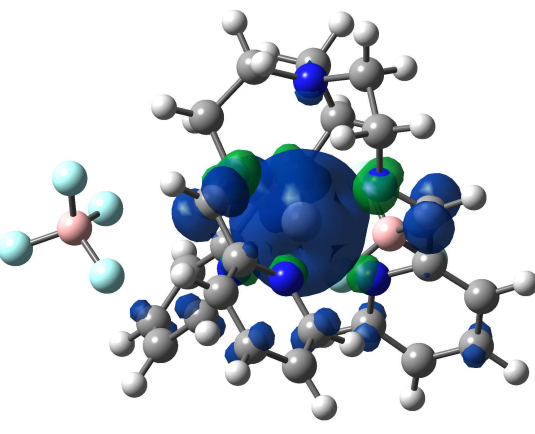
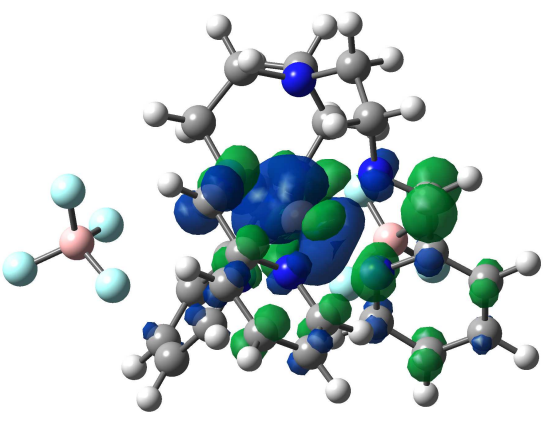
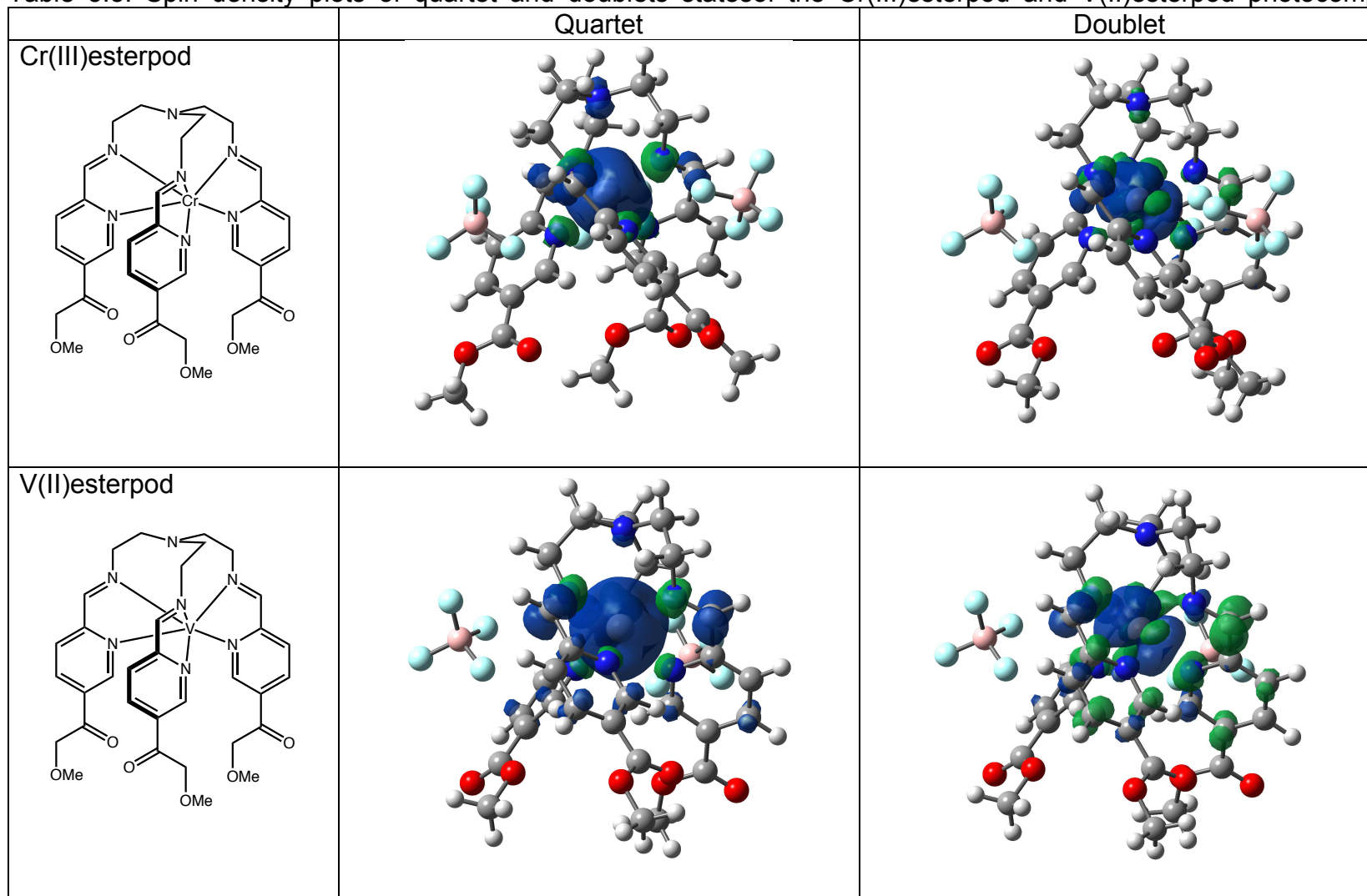
	Quartet	Doublet
Cr(III)pod 		
V(II)pod 		

Table 5.3: Spin density plots of quartet and doublet states of the Cr(III)esterpod and V(II)esterpod photocomplexes.



with Cr(III) complex keeping much electron density centered on the metal while the spin density of the V(II) complex was again displaced out onto the ligand.

As evident from these spin density plots, there is a strong difference where the lone electron is going following excitation to the doublet state in the Cr(III) and V(II) case. In the V(II) case there is significant delocalization of the quartet spin on the ligand as well as the doublet state with antiparallel spin. In fact, increasing donating ligands by methyl substituting the pyridine ligands didn't make much of a difference. There seems to be favorable exchange for the quartet state, but in the case of the doublet state for V(II), the α and β electrons want to be delocalized as much as possible. The d orbitals on the vanadium metal are much larger than the d orbitals of the chromium metal due to d orbital expansion. Therefore this delocalization decreases the magnitude of excitation for the vanadium complexes, which greatly hinders its potential as a prominent photocatalyst.

C. VIBRATIONAL PROJECTION SPECTRA:

The vibrational distortion projection plots highlight additional differences between the Cr(III) and V(III) complexes by comparing the vibrational normal mode components that make up the distortion from the ground state to the excited state. Comparing the plots for Cr(III)(bpy)₃ and V(II)(bpy)₃ shows a two to six times larger dependence on very low modes less than 100 cm⁻¹ for the V(II) complex compared the Cr(III) complex (See Figure 5.3). For V(II)(bpy)₃, the dominant modes are those that consist of symmetric ligand wags, symmetric torsions between the pyridines, and symmetric ligand stretches with the metal center. Many of the Cr(III)(bpy)₃ dominant modes are shared with V(II)(bpy)₃ such as the symmetric ligand wags and stretches, but also

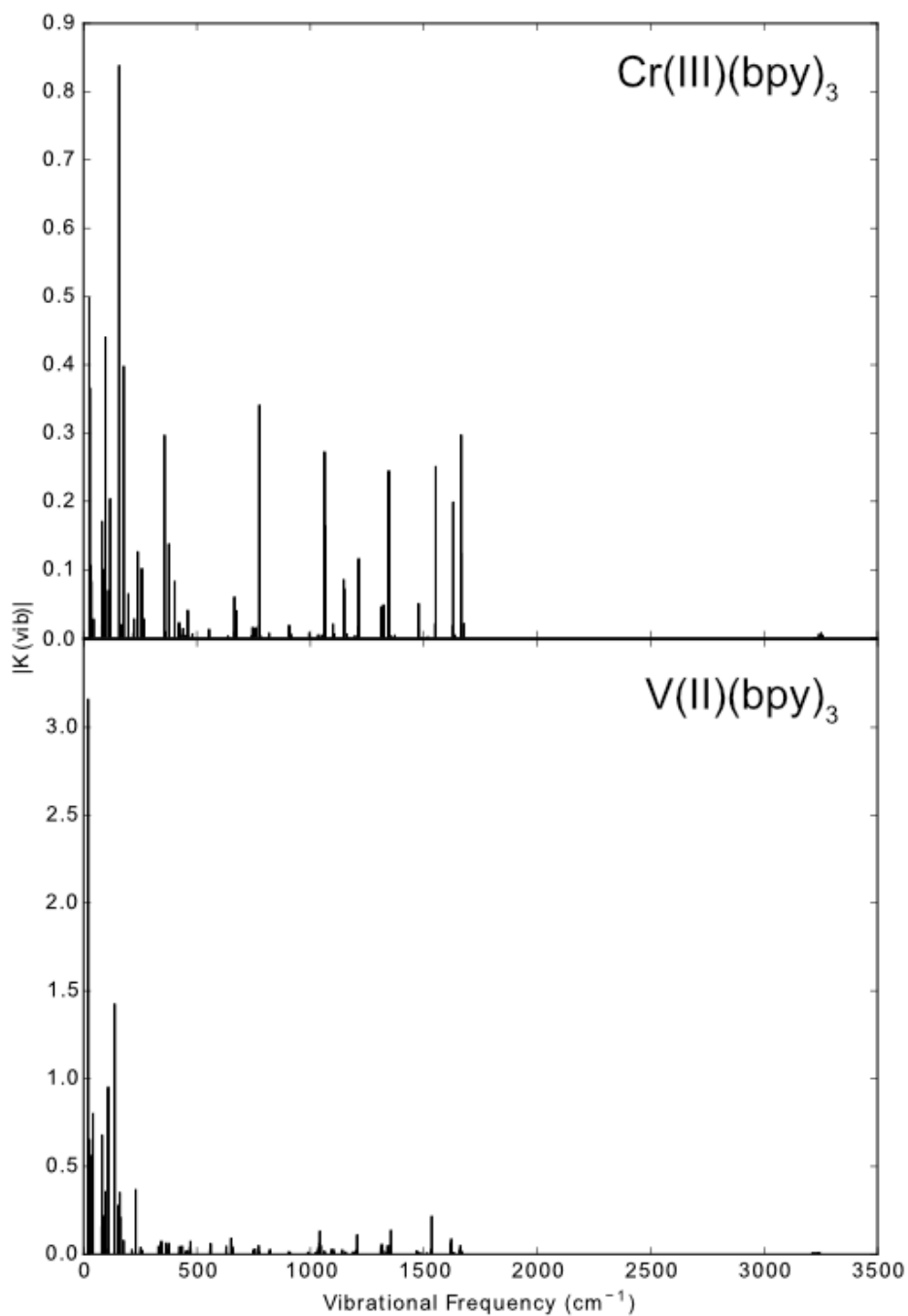


Figure 5.3: Vibrational distortion projection plot between the ground state and excited state quartet structures for Cr(III)(bpy)_3 and V(II)(bpy)_3 . The units of the K elements are in $\text{\AA amu}^{1/2}$.

includes an asymmetric pyridine torsion, asymmetric ligand wag, and an asymmetric ligand-metal center stretch. In addition, an intraligand stretch on a single ligand is also a dominant mode. This implies that not only are the excited state structures different between the two metal center based ligands, the excited state pathway that the complex takes upon excitation is very different. Whether the different pathways lead to an intersystem crossing event requires additional measurements to determine. However, these results suggest that Cr and V isoelectronic complexes with identical ligands cannot be assumed to behave similar in their excited states.

D. SORCI:

The excited state potential energy surfaces of the PDO ligand complexes for Cr(III) and V(II) provide additional insight into the differences between the two metals within similar complexes. The Cr(III)(AcAc)₃ complex has been widely studied in literature. The complex ground state is ⁴A_{2g}. Upon initial excitation, the complex is promoted to the ⁴T_{2g} state. The complex rapidly relaxes to the ²E_g, a long-lived state that is thought to be primary state through which the complex performs catalytic functions.

Plotting the excited states of each state along the linear path between the ⁴T_{2g} and ²E_g excited states, an immediate difference is seen between the Cr(III)(PDO)₃ and the V(II)(PDO)₃ complexes, see Figure 5.4. For the Cr(III) complex, a prominent feature of the plot is the crossing of the lowest excited quartet states with the lowest doublets around R = 0.67 along the distortion coordinate. This provides a low barrier pathway to the ²E_g state since the states in the crossing region do exhibit mixed doublet/quartet character when spin-orbit coupling contributions are included in the calculation. This

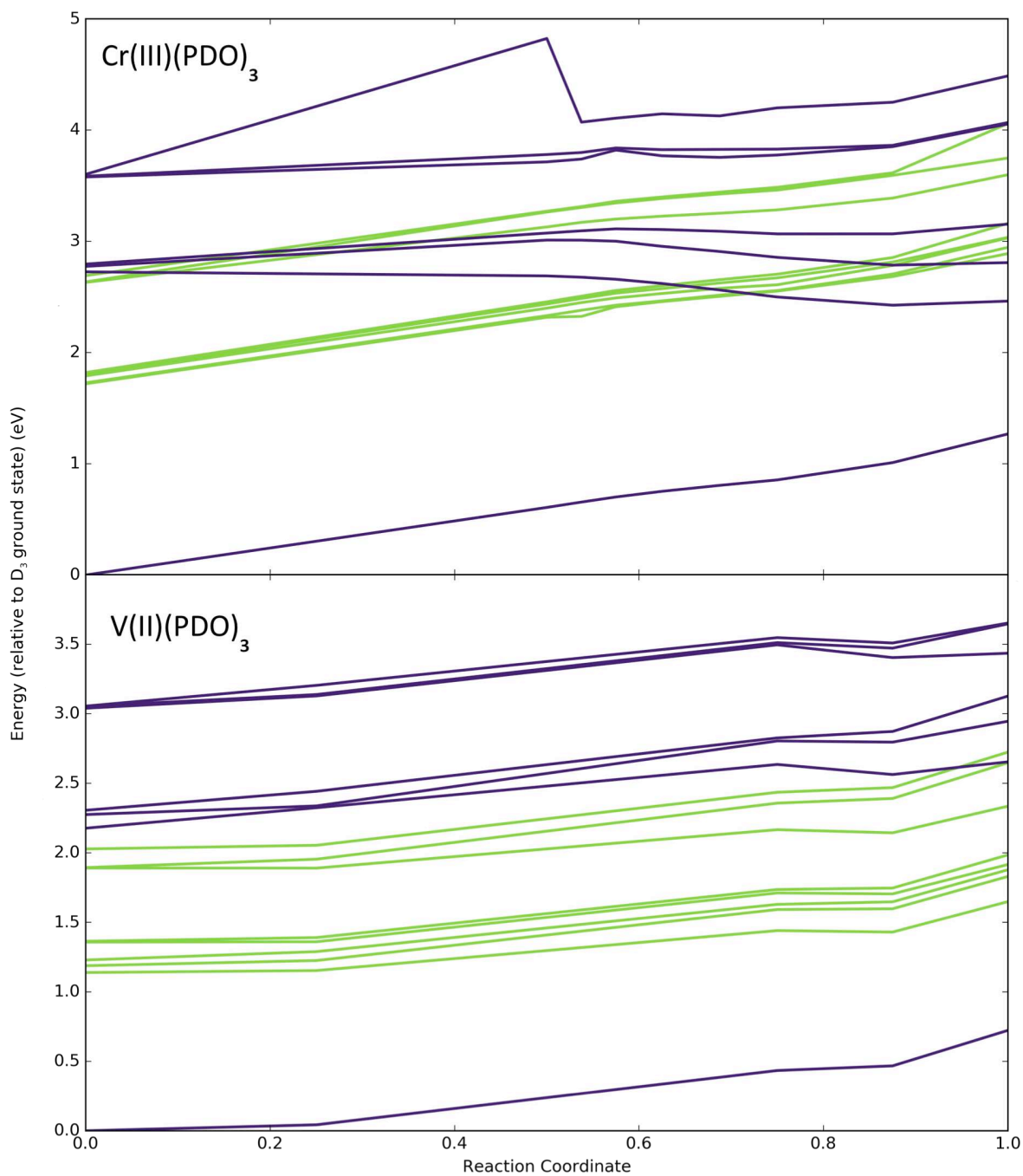


Figure 5.4: Plot of excited state energies of $X(\text{PDO})_3$ complexes where X is Cr(III) or V(II) along a linear distortion reaction coordinate between the $^4A_{2g}$ and $^2T_{2g}$ optimized geometries. The purple lines represent the quartet states and the green lines represent the doublet states. The V(II) and Cr(III) complexes show strikingly different behavior along the distortion coordinates, where the Cr(III) complex shows a complete crossing several doublet and quartet states while the V(II) complex shows minimal places where the states are degenerate.

agrees with experimental results demonstrating the fast intersystem crossing to the 2E_g state in Cr(III)(AcAc)_3 .

The excited states along the distortion coordinate show a different trend for the V(II)(PDO)_3 complex. The lowest excited quartets rise in energy with the doublets as the structure distorts towards the stable ${}^4T_{2g}$ state. This contrasts the Cr(III) complex where the lowest excited quartets decrease in energy as a function of distortion. This causes no crossings between the excited quartets and doublets in the V(II) complex. While the difference between these two excited state pathways is not definitive proof that V(II)(PDO)_3 is unable to reach the 2E_g state, it does suggest that V(II) complexes may be significantly less likely to reach a stable doublet state upon excitation compared to a Cr(III) analog. Without a complete map of the potential energy surface, it is not known whether other low barrier quartet to doublet transitions exist, but the most direct path does not contain one.

IV. CONCLUSIONS:

We have highlighted the substantial differences exhibited by various transition metal complexes with Cr(III) and V(II) with respect to their excited states. The absorption spectra demonstrate the wide range of excited states that are populated upon vertical absorption, which can lead to shifts of more than 100 nm in the visible range. This is a very useful property to try to exploit to obtain catalysts that absorb in a desired range. However, the change in absorption also implies a change to excited state dynamics as well. The spin density plots, vibrational distortion plots, and SORCI derived excited state potential energy curves demonstrate a significant change to the excited state dynamics from the substitution of Cr(III) with V(II) . Having a complex with

desirable excited state properties is critical to a photocatalyst's ability to participate in redox chemistry. Evidence demonstrating that V(II) based photocatalysts do not easily form a long-lived excited state through intersystem crossing reduces their utility as photocatalysts.

REFERENCES

- (1) Yoon, T. P.; Ischay, M. A.; Du, J. Visible Light Photocatalysis as a Greener Approach to Photochemical Synthesis. *Nat. Chem.* **2010**, 2 (7), 527–532.
- (2) Tucker, J. W.; Stephenson, C. R. J. Shining Light on Photoredox Catalysis: Theory and Synthetic Applications. *J. Org. Chem.* **2012**, 77 (4), 1617–1622.
- (3) Frisch, M. J.; Trucks, G. W.; Schlegel, H. B.; Scuseria, G. E.; Robb, M. A.; Cheeseman, J. R.; Scalmani, G.; Barone, V.; Mennucci, B.; Petersson, G. A.; et al. *Gaussian 09 Revision D.01*.
- (4) Ando, H.; Iuchi, S.; Sato, H. Theoretical Study on Ultrafast Intersystem Crossing of Chromium(III) Acetylacetonate. *Chem. Phys. Lett.* **2012**, 535, 177–181.
- (5) Miller, W. H.; Ruf, B. A.; Chang, Y.-T. A Diabatic Reaction Path Hamiltonian. *J. Chem. Phys.* **1988**, 89 (10), 6298–6304.
- (6) Neese, F. The ORCA Program System. *Wiley Interdiscip. Rev. Comput. Mol. Sci.* **2012**, 2 (1), 73–78.

CHAPTER 6: ELUCIDATING EXPERIMENTAL RESULTS OF MACROCYCLE PHOTOCOMPLEXES THROUGH TDDFT¹

I. INTRODUCTION

Photocatalysis is an important industrial field that has made a lot of progress in the last decade. Many photocatalysts have been shown to be useful for many phototransformations.¹⁻⁴ However, virtually all of these photocatalysts rely on the use of a rare metal that is both expensive and unsustainable.^{5,6} There is large potential for using earth abundant first row transition metals for photocatalytic reactions, but this relies heavily on characterizing and tuning the metals and ligands of these photocomplexes.

With appropriate experimental and theoretical collaborations, it is conceivable to tune these photocomplexes for an inner sphere photocatalytic mechanism that would take advantage of the lability of these first row transition metals to produce value-added products. An inner sphere photomechanism opens up the possibility of producing enantioselective products without the use of wasteful stoichiometric reagents. The use of transition metal complexes for enantioselective inner sphere phototransformations will require a unique system that can only be deduced from a complex characterization using both experimental and theoretical techniques.

Our group has shown that the use of TDDFT is an effective method for characterizing the excited states and absorption spectra of a given system. The use of

¹ The work in this chapter was done by Collette M. Nite and David J. Boston. Collette M. Nite performed all theoretical calculations and analysis. David J. Boston is responsible for all experimental work, including the synthesis, and absorption spectra of the transition metal complexes. The text was written entirely by Collette M. Nite.

this method has been shown beneficial for selectively tuning ligand manifolds for desired absorption in the visible region (see Chapter II). In addition, this method has gone beyond qualitative trends to collaboratively characterizing structural differences within the metal and ligand framework as with the protonation state of the Cr(III)THB complex to navigate synthetic difficulties (see Chapter IV).

This study again focuses on the H₂thb(5,6,7,8-tetrahydrotribenzo[b,f,1][1,4,8,11]tetra-azacyclotetradecine (THB) ligand that has been of great interest to our group and our collaborators as a potential inner sphere photocatalyst. As previously discussed (see Chapters II and IV), the THB ligand contains a decent amount of conjugation within the ligand manifold to provide intense absorption in the visible region. Different coordinating metals also provides a source of tunability for changing where specifically the complex is absorbing, different coordination sites, as well as different spin manifolds for the potential for long lived lifetimes. The –NH secondary amine moieties of the complex have aided in metal complexation in addition to proton sources that can change how this complex behaves photochemically (see Chapter IV). This chapter first compares the theoretical TDDFT spectra of first row transition metal THB complexes to their experimental spectra. A TDDFT study is then conducted that looks at the nature of acetonitrile binding as a potential substrate to the Cr(III) THB complex in order to analyze its potential for inner sphere photocatalysis.

II. EXPERIMENTAL

All calculations utilized Gaussian G09d suite of electronic structure codes.⁷ Complexes were first optimized using DFT and then the first 24 excited states were

calculated using TDDFT. The Cr (III), Fe(II), Co(II), Ni(II), Cu(II) and Zn(II) THB complexes in Figure 6.1 were calculated using a PCM solvent model with dimethylformamide (DMF) in order to compare to experimental spectra. The experimental spectra were calculated using the excited state energies and intensities from the TDDFT calculations convoluted over a 0.093 eV full-width half-max Gaussian to approximate experimental linewidths.

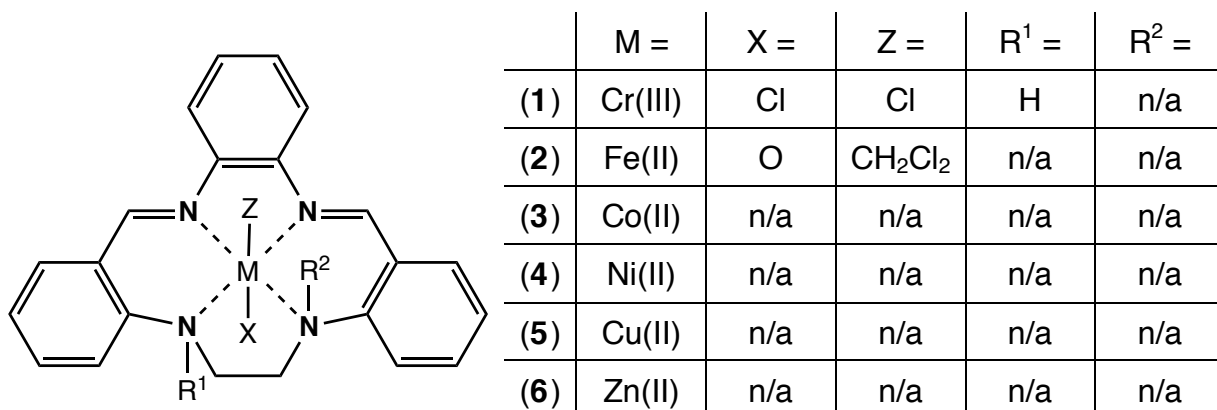


Figure 6.1: THB complex of first row transition metals that were calculated and compared to experimental data.

Fe(II) and Co(II) were calculated in their low spin states. The Cr(III)THB complex was also modeled in acetonitrile in order to study the binding of acetonitrile to the Cr(III) metal center. From the excited state energies and oscillator strengths, theoretical absorption spectra were plotted. Natural transition orbitals (NTOs) were obtained from the TDDFT calculation and were plotted using the Gaussview software.

III. RESULTS

The theoretical absorption spectra of the metal THB complexes are plotted in Figure 6.2 with the corresponding experimental spectra (in red) of the complex in DMF solvent. While there is a fair amount of qualitative theoretical and experimental agreement in some spectra, other spectra do not closely align.

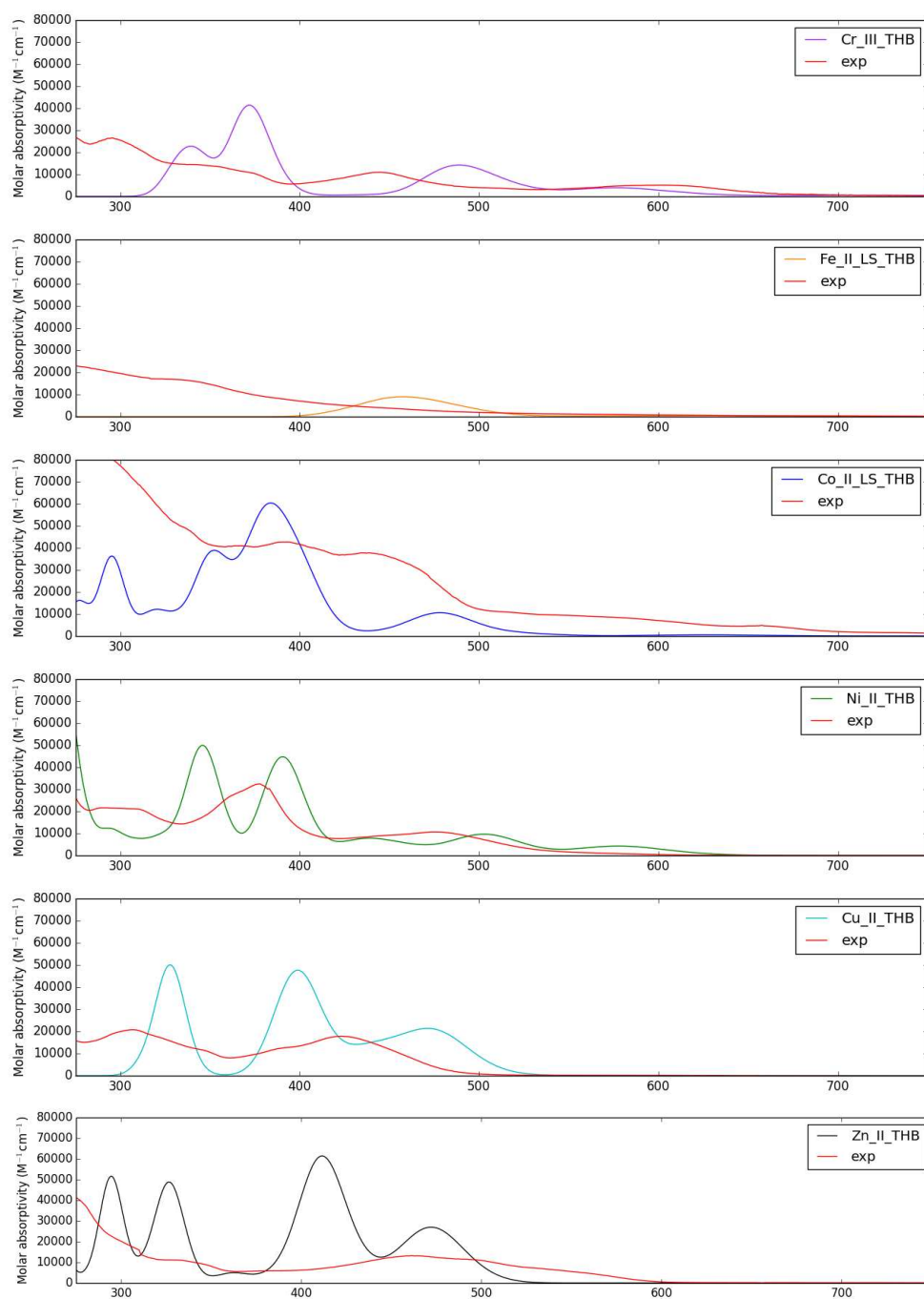


Figure 6.2: TDDFT(APF-D/6-311+G*) absorption spectra of Cr(III) complex (1) (purple), low spin Fe(II) complex (2) (orange), low spin Co(II) complex (3) (blue), Ni(II) complex (4) (green), Cu(II) complex (5) (aqua), and Zn(II) complex (6) (black) THB complexes with implicit DMF solvent overlaid with corresponding experimental spectra of THB complex in in DMF solvent (red).

General trends can be elucidated such as the complex's expected absorption range, while peak intensities and positions are not as well described theoretically. Solvent plays a major factor in these discrepancies. The PCM solvent model is an implicit solvent model where no explicit solvent molecules are present. Especially for a polar solvent like DMF, explicit solvent molecules could be important for understanding the system. A DMF solvent molecule may be coordinated to the metal center or interacting with a ligand system. More detailed calculations would need to be run in order to understand what we are seeing in solution.

In addition, transition metal complexes are difficult to characterize experimentally due to their ability to occupy multiple spin states. It is intuitive therefore that the complexes that are generally characterized by one common spin state such as Ni(II), Cu(II), and Zn(II) have better experimental agreement. Metals such as Fe and Co easily undergo oxidation state changes in addition to occupying high spin and low spin states. It is therefore difficult to know for certain what states these complexes are in without further information since the spin states of the Fe and Co metal centers have not been experimentally established. The theoretically calculated state may be different than the one observed experimentally.

In order to emphasize the importance of explicit solvent when characterizing these complex systems, and to observe the possibility of substrate binding for the potential for inner sphere photocatalysis, the structures in Figure 6.3 were studied. The Cr(III)THB complex with protonated secondary amines (**7**) was first calculated in acetonitrile by using the implicit PCM solvent model. An explicit acetonitrile molecule was then added to the Cr(III)THB complex where one secondary amine was

deprotonated (**8**). It was assumed that the H would leave with the once-bound Cl^- ion upon acetonitrile substitution. The complex was again deprotonated with the addition of another acetonitrile molecule explicitly bound to the Cr(III) metal center (**9**).

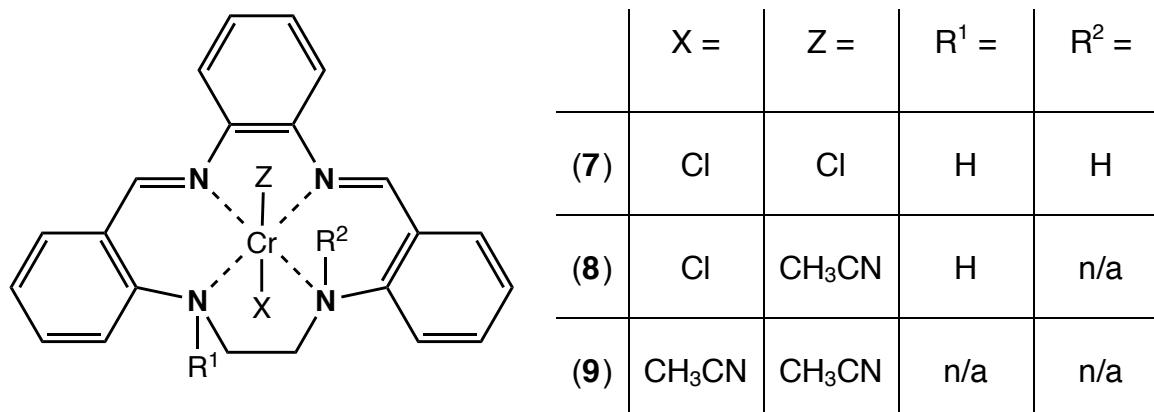


Figure 6.3: Structure derivatives of Cr(III) THB complex with acetonitrile solvent.

The theoretical spectra of the calculated excited states of structures in Figure 6.3 are shown in Figure 6.4. Addition of the acetonitrile molecules changes the spectrum considerably. For the case of complex (**7**) in implicit solvent with no acetonitrile molecules bound, there are no observed spectral features past around 415 nm (in red). Peaks grow in upon the addition of explicit acetonitrile molecules.

The theoretical spectra were compared to the experimental spectrum of Cr(III)THB in acetonitrile solvent. Figure 6.5 compares the calculated spectrum of complex (**8**) with one acetonitrile bound to the experimental spectrum. Spectral features were observed past 400 nm indicating that acetonitrile was bound to the Cr(III) complex.

There is good qualitative agreement between the experimental and theoretical spectra, with the peaks around 300 nm, 375 nm, and 480-520 nm being of particular interest. There are some features in the experimental spectrum that also correlate well

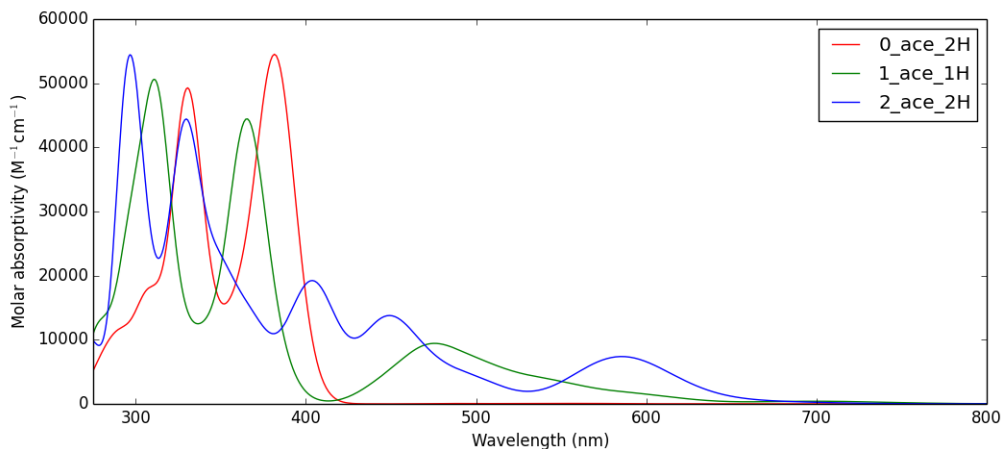


Figure 6.4: TDDFT(APF-D/6-311+G*) absorption spectra of Cr(III) THB structures in Figure 6.3 with implicit acetonitrile solvent.

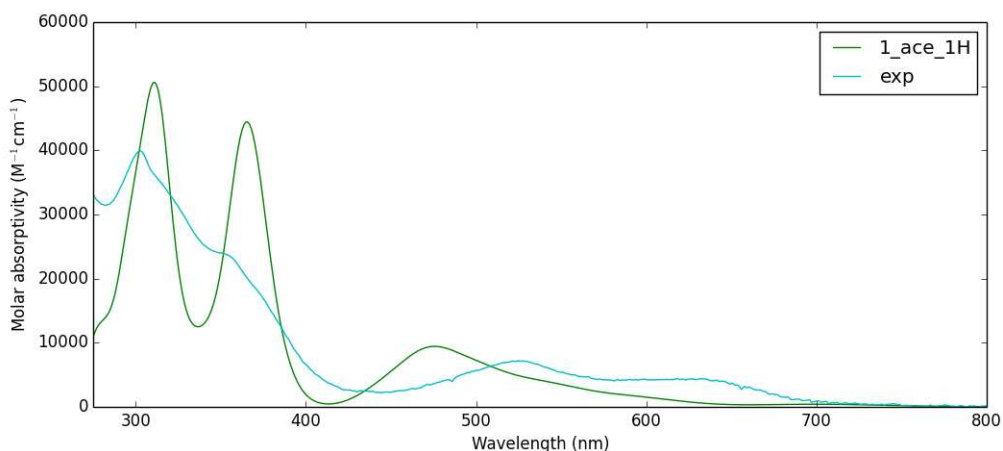


Figure 6.5: TDDFT(APF-D/6-311+G*) absorption spectrum of Cr(III)THB complex (**8**) with one acetonitrile explicitly bound in addition to implicit acetonitrile solvent (green) as compared to the experimental spectrum of Cr(III)THB in acetonitrile (aqua).

with the calculated spectrum of complex (**9**). The long wavelength spectral feature at around 630 nm corresponds well to the two acetonitrile bound case. The experimental spectral broadening is greater than the theoretical spectral broadening due to solvent effects not present in the theoretical calculations.

Figure 6.6 provides a comparison of the experimental and theoretical spectra for Cr(III)THB complex with two acetonitrile molecules bound, complex (9). In comparing Figure 6.5 and Figure 6.6, it is evident that there are some similar experimental features present in both theoretical spectra. The experimental solution may indeed have both complexes that have either one, complex (8), or two acetonitriles bound, complex (9). The importance is that there seems to be some acetonitrile bound in either case due to the presence of low energy transitions in the experimental spectrum. The significance of the experimental spectrum is that it shows the potential for substrate binding to the metal center of this complex, which is vital for the success of this complex as an inner sphere photocatalyst.

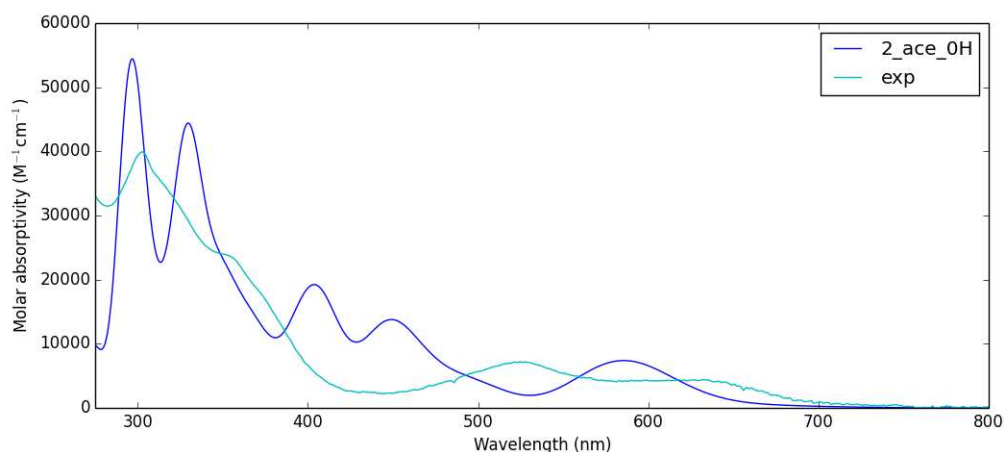


Figure 6.6: TDDFT(APF-D/6-311+G*) absorption spectrum of Cr(III)THB complex (9) with two acetonitrile molecules explicitly bound in addition to implicit acetonitrile solvent (blue) as compared to the experimental spectrum of Cr(III)THB in acetonitrile (aqua).

Natural transition orbitals (NTOs) provide additional insight into the characterization of these excited states. NTOs show where the electron came from and where the electron went to in the excitation of a given state. Interestingly, very low excited states show electron density going to the acetonitrile substrate in both cases.

This is a very exciting feature for the potential for inner sphere photocatalysis using visible light as its light source.

NTOs of excited states of the complexes of particular interest are given in Table 6.1 and Table 6.2. The second excited state at 668 nm of the Cr(III)THB complex (**9**) shows electron density going from the metal to the substrate, with electron density out on the carbon of the acetonitriles. This excited state is of low energy visible light that would be useful for photoexcitation. The reduction of the carbon shows that there is potential for some inner sphere catalysis and further chemistry.

In the experimental spectrum in Figure 6.5, there is a broad peak centered around 525 nm. The NTOs of the excited state (Table 6.1) at 504 nm of Cr(III)THB complex (**8**) show electron density going from the ligand and metal of the complex to the nitrogen and carbon of the acetonitrile substrate. Similar NTOs were observed for complex (**9**) at 480 nm where there is a THB ligand to metal and acetonitrile transition. Electron density is again seen out on the acetonitrile substrates for excited states around 390 and 408 nm given in Figure 6.6. There is a prominent absorption peak around 390 nm present in the experimental spectrum further suggesting that not only are there excited states that activate the substrates, but that these states have significant excitation probability.

IV. CONCLUSION

The initial results show promise for a Cr(III)THB complex being a successful inner sphere catalyst. Theoretical spectra show qualitative resemblance to the experimental spectrum of the Cr(III)THB in an acetonitrile solution. NTOs further propagate the assumption that a bound substrate can be activated by visible light, a first

Table 6.1: NTOs of various excited states of the Cr(III)THB complex (**8**) with an acetonitrile molecules bound, showing where the electron came from during the excitation (left) and where the electron went to in the excitation (right). NTOs were generated from TDDFT(APF-D/6-311+G*) calculations.

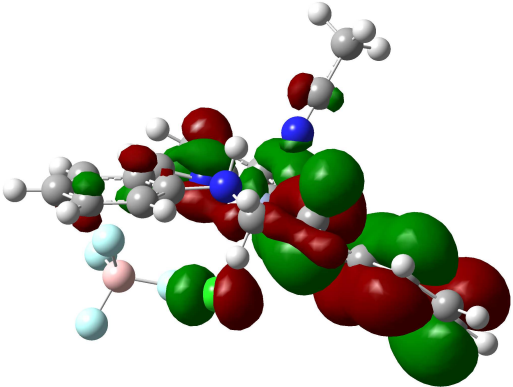
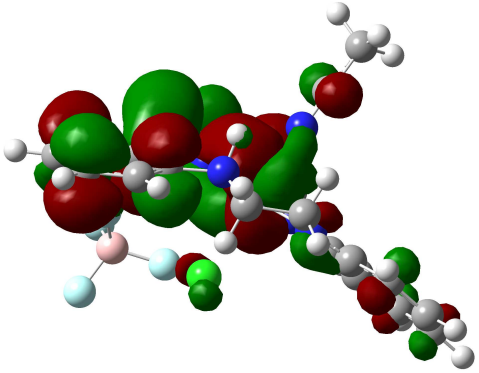
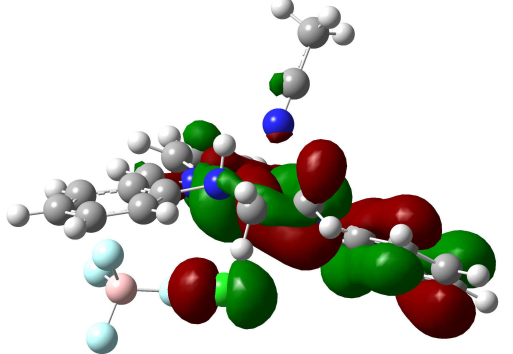
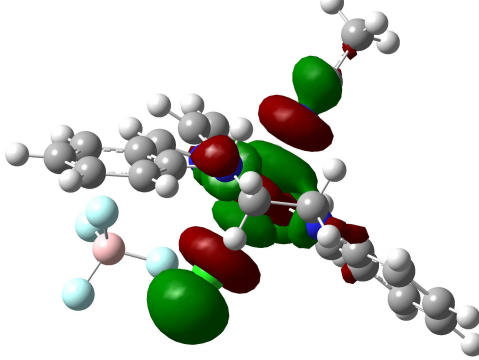
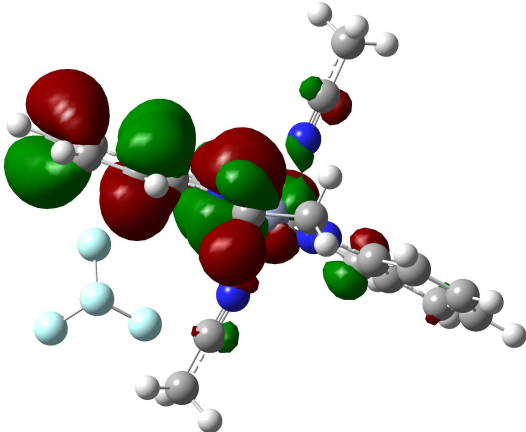
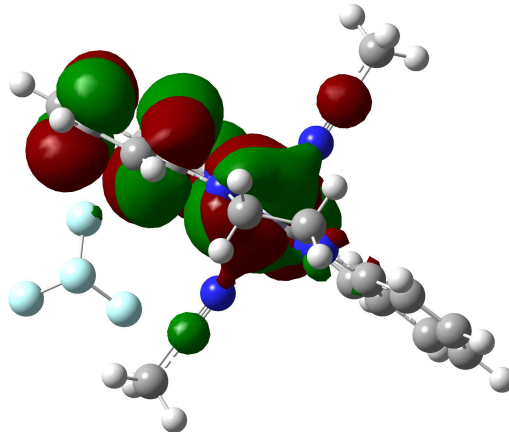
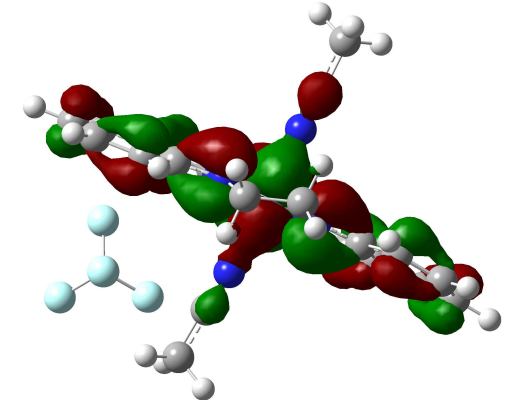
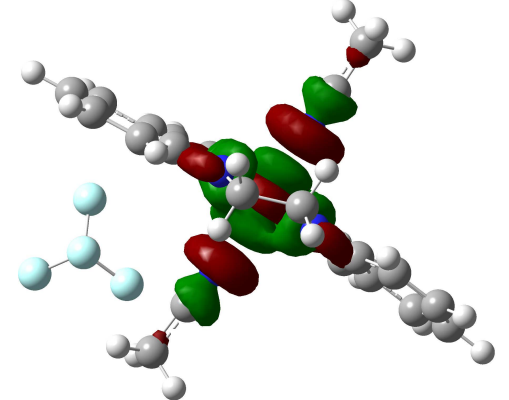
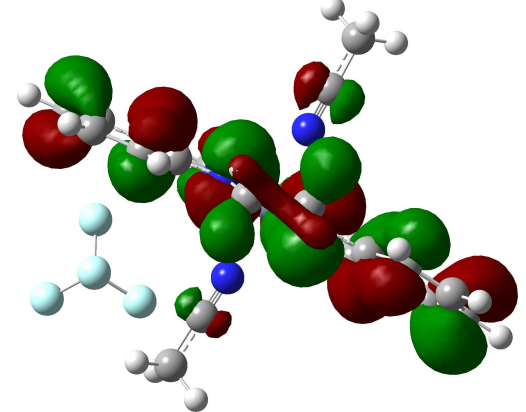
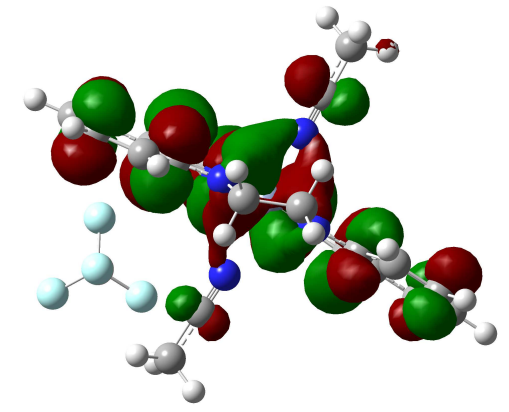
From	To
	
Excited state 6(βe^-) at 504 nm	
	
Excited state 10(αe^-) at 390 nm	

Table 6.2: NTOs of selected excited states of the Cr(III)THB complex (**9**) with two acetonitrile molecules bound. The left MOs visualize the orbitals that the electron comes from and the right MOs represent where the electron went to.

From	To
	
Excited state 2(βe^-) at 668 nm	
	
Excited state 7(αe^-) at 480 nm	
	
Excited state 12(βe^-) at 408 nm	

step to the development of an inner sphere photocatalyst. Additional studies are necessary in order to claim that acetonitrile is indeed binding to the metal center of the complex. Also, the inclusion of a variety of substrates could provide insight into capacity of Cr(III)THB for behaving as an inner sphere photocatalyst.

REFERENCES

- (1) Cieśla, P.; Kocot, P.; Mytych, P.; Stasicka, Z. Homogeneous Photocatalysis by Transition Metal Complexes in the Environment. *J. Mol. Catal. Chem.* **2004**, *224* (1–2), 17–33.
- (2) Lang, X.; Chen, X.; Zhao, J. Heterogeneous Visible Light Photocatalysis for Selective Organic Transformations. *Chem. Soc. Rev.* **2014**, *43* (1), 473–486.
- (3) McConnell, I.; Li, G.; Brudvig, G. W. Energy Conversion in Natural and Artificial Photosynthesis. *Chem. Biol.* **2010**, *17* (5), 434–447.
- (4) Narayanam, J. M. R.; Stephenson, C. R. J. Visible Light Photoredox Catalysis: Applications in Organic Synthesis. *Chem. Soc. Rev.* **2011**, *40* (1), 102.
- (5) Schultz, D. M.; Yoon, T. P. Solar Synthesis: Prospects in Visible Light Photocatalysis. *Science* **2014**, *343* (6174), 1239176.
- (6) Tucker, J. W.; Stephenson, C. R. J. Shining Light on Photoredox Catalysis: Theory and Synthetic Applications. *J. Org. Chem.* **2012**, *77* (4), 1617–1622.
- (7) Frisch, M. J.; Trucks, G. W.; Schlegel, H. B.; Scuseria, G. E.; Robb, M. A.; Cheeseman, J. R.; Scalmani, G.; Barone, V.; Mennucci, B.; Petersson, G. A.; et al. *Gaussian 09 Revision D.01*.

CHAPTER 7: FUTURE DIRECTIONS

A protocol for using TDDFT to study first row transition metal inner sphere photocatalysts has been established in this dissertation. Optimizing complex structures with a high degree of accuracy and corresponding excited state calculations yield theoretical absorption spectra that qualitatively reproduce experimental trends. These qualitative trends helped steer the direction of ligand design for potential catalytic systems in collaboration with experimentalists. Methods have been applied to help answer a variety of experimental issues that arise in exploring these catalytic systems, including the effect of protonation state on the electronic properties of a system, providing rationale for different electronic properties of transition metals with similar electron configurations, exploring solvent effects and a catalyst's potential to bind a substrate resulting in electron transfer for inner sphere photocatalysis. In addition, a method for recovering the vibronic character of these complexes has also been shown in this dissertation.

It is well known that electronic experimental spectra are not purely electronic excitations, but rather vibrational character is also included in the spectra. Therefore, theoretical spectra should also reflect this vibronic coupling. However, the theory that is established for generating a vibronic spectrum, discussed in Chapter III, is not robust. The Franck-Condon corrections to the electronic spectra are very sensitive to the total atom displacements and vibrational normal modes in the ground and excited state being studied. If the system undergoes large atom displacements between the optimized ground and excited state structures, the Franck-Condon overlaps are negligible for most

vibrational modes. The same is true if the nature of the vibrational normal modes changes between the two structures. For transition metal complexes, this causes most implementations of a vibronic spectrum calculation to fail. Another theoretical hurdle is rectifying multiple vibronic spectra when the optimized structures of several excited states for one system differ greatly. Even if one obtains a vibronic spectrum for each excited state, this leaves one with many spectra to convolute in order to compare to a single UV-vis experimental spectrum.

Future directions for this project require theoretical exploration to construct a more general theoretical form, useful for a variety of systems. Two important improvements are needed. The first improvement is a series of enhancements to the Franck-Condon spectral corrections theory such that it is more stable for transition metal complexes that undergo large geometric distortions upon excitation. Much of the benchmarks for the method in the literature focus on organic molecules, which behave much differently than coordination complexes. A more generic approach could yield better results for organic and inorganic systems. The second improvement needed is a coherent method of combining multiple vibronic calculations into a single spectrum to compare to experimental results. A simplistic approach may be to add the vibronic character only to the state that is the focus for a given vibronic calculation, however more sophisticated schemes are possible. Only then can traditionally accepted excited state pathways be challenged and complex first row transition metal excited state pathways be predicted. Knowledge of excited state pathways is vital for the further understanding of inner sphere catalytic mechanisms.